Numerical Study on Hydrodynamics and Sediment Transport of Shallow Coastal Lagoons

Mohamed Reda Mohamed Mahmoud Soliman

July 2013

Numerical Study on Hydrodynamics and Sediment Transport of Shallow Coastal Lagoons

Mohamed Reda Mohamed Mahmoud Soliman
Graduate School of Engineering
Kyoto University

A thesis submitted for the degree of
Doctor of Philosophy

July, 2013

Doctoral Supervisory Committee

1. Prof. Satoru Ushijima (thesis supervisor)

2. Prof. Tetsuya Sumi (thesis committee supervisor)

3. Assoc. Prof. Nozomu Yoneyama (thesis committee supervisor)

Day of the defense: July 29^{th}, 2013

Preface

Brackish coastal lagoon is considered an interactional zone between sea salty water and river's fresh water. When a river flows into the sea or ocean, there is a transition region in between. We call this region an estuary. Recently, it has been discovered that what distinguishes fresh water zone from saltwater zone in estuaries is a zone with a peculiar density separating the two zones. This zone, which has a different salinity from the fresh water and salty water (Brackish water), is set between bitter and sweet water and it does not allow them to get mixed. Today we know this zone (barrier). It is well known that when fresh water placed beside salty water, they do mix. But in case of estuaries they don't and this is a great capital for them. This separation has important biological effects on the ocean and the marine living organisms. Also, it ensures that salty water will not dominate over the fresh water. This fact was stated in the holy Qur'an around 1400 years ago.

"And He it is Who had made the two seas join and flow together, one palatable and sweet, and the other salt and bitter; and between the two He has made a barrier and inviolable obstruction." Al-Furqan(25), verse 53.

This noble Qur'anic verse depicts one of the wonderful manifestations of Allah's might in the world of creation. It needs not mentioning that the existence of natural reasons in such issues does not devaluate them. What is nature? It is nothing except Allah's will and intention that has bestowed such attributes to these creatures.

M.R. Soliman

To .....
My family & my professor Hossam Nagi

Acknowledgements

One of the joys of completion is to look over the journey past and remember all who have helped and supported me along this long but fulfilling road. I am highly indebted to my supervision panel and wish them all the best.

My sincere appreciation goes to my supervisor Prof. Satoru Ushijima for his constructive ideas, advices, unlimited support, help in academic front as well as extra-curricular life during my stay in Japan is beyond any repayment.

I would also like to express my heartfelt gratitude to my supervisor Prof. Tetsuya Sumi who provided valuable suggestions during my study, fruitful discussions, encouraging and constructive feedback.

I extend my sincere gratitude to my supervisor Prof. Nozomu Yoneyama for his constructive reviewing and suggestions in improving this work.

I am appreciated to Prof. Ibrahim El-Shinawy and Coastal Research Institute (CORI) members for help and providing the available field data.

Special thanks to our laboratory members, colleagues and friends especially Dr.Yamazaki, Yamashita San and Daisuke San for helping me in lab issues.

I extend many thanks to my Egyptian friends Dr.Sameh Kantoush and Mohamed Elwi for their help and valuable advices during my stay in Japan.

I am grateful to the Japanese Government through Ministry of Education, Culture, Sports, Science, and Technology (MEXT) for financial support through Monbukagakusho scholarship, which covered my personal maintenance as well as academic costs.

Finally, thanks to my family for their constant support and love; without them, it would be very difficult to complete this thesis.

Abstract

This research presents a numerical study for El-Burullus lagoon brackish water as a model example for the other Egyptian coastal lakes on the Mediterranean Sea. This lake ecosystem has deteriorated since Aswan High Dam construction, 1965. It is suffering from many problems, which might lead to environmental degradation and substantial changes in its ecosystem. Lake salinity has suffered from significant decrease due to excess unregulated drainage water effluent into the lake, which affected the lake flora and fauna. The purpose of the current study is to restore the salinity conditions of El-Burullus Lake to those before the construction of Aswan High Dam. For this purpose, three models are developed to simulate the lake hydrodynamics, circulation and salinization dynamics process.

The first model is a depth-averaged mass transport model; this model is based on MAC method on collocated grid for shallow water equations (MACS) algorithm with unstructured collocated grid system using the distributed memory system. The model numerical solutions is built on recent advances to couple numerical processes of hydrodynamic and mass transport equations using the finite volume method (FVM) in discretization. Further, on the basis of a domain decomposition method, the unstructured cells are decomposed into multiple sub-domains and their computations are simultaneously performed with the distributed-memory system. This method is implemented by message-passing interface (MPI) which significantly reduces the elapsed time of computation. It is demonstrated that the parallel efficiencies are attained by parallel computations. The model has been successfully verified against analytical solution to the advection diffusion equation and experimental measurements to transported concentration cloud in a meandering channel. Furthermore, a numerical prediction method for equilibrium and non-equilibrium sediment transport under

current and wave actions has been included in the present model. The partial differential equations for two-dimensional (2D) shallow water flow, suspended-load, bed-load sediment and bed evolution were successfully incorporated to predict the bed morphological changes. The developed model has been tested in different laboratory cases: scour downstream solid apron, shallow basin erosion due to clear water, sedimentation in a channel perpendicular to unidirectional flow of current and waves and local scouring around bridge pier abutment. Generally, good agreement was obtained between numerical simulation results and experimental data. This fact shows that the present numerical method is able to predict the sand bed profiles reasonably. After model verification, the developed model is applied to El-Burullus shallow coastal lake in Egypt. Salinity distribution inside the lake is reasonably simulated considering the effect of bathymetry, tidal current, wind, precipitation, evaporation and drainage discharges. It is verified that the model has the potential for simulating long-term coastal process using parallel computation.

The second model is a two-phase flow mass transport model; a 2D multiphase numerical model for incompressible, immiscible and variable density fluids has been developed to study stratification process of brackish coastal lakes due to density variation. The governing equations are discretized in a collocated grid system and solved with a finite volume method. A parallel computation technique in shared memory system is implemented in the present model by Open Multiprocessing (OpenMP). The developed model successfully predicted the density current propagation in the lock-exchange problems for Boussinesq and non-Boussinesq experimental cases. In addition, the model is applied to simulate salinity intrusion into Ohashi River that connects Nakaumi and Shinji brackish coastal lakes. The developed model successfully predicted the density current propagation in the River. However, this model still needs refinement to avoid concentration oscillations.

The third model is a three-dimensional multiphase model; this model is based on multiphase incompressible flow solver with collocated grid system

(MICS) algorithm which predicts the interaction between three-dimensional (3D) free surface flows and solid bodies. The free-surface flow including solid objects is modeled as a multiphase flow field. The governing equations for the multiphase field are solved on the basis of a finite volume method with collocated grid system. The model successfully predicted the density current propagation in the lock-exchange problems for Boussinesq and non-Boussinesq experimental cases. Moreover, the model is applied to the experimental results of the Nakaumi-Shinji coastal lakes system. Good agreement was obtained between experimental results of the density current propagation front position and those that are numerically estimated.

The validated depth-averaged mass transport model was applied to El-Burullus shallow coastal lake, Egypt. Five scenarios were studied for further understanding of the lake circulation and salinity dynamics and to investigate possible means of restoring them to the desired state as before Aswan High Dam construction. These scenarios revealed the importance of fresh drainage water release into the lake and the possibility of its use as an artificial flood similar to pre-Aswan High Dam construction flood under a well-monitored control system. In addition, the present model was used to investigate the impact of climate change on the lake salinization process under two IPCC climate change scenarios (SRES B1 and SRES A2). Although numerical results predicted the increase of salinity values to double the current values, they were still obviously lower than those before constructing Aswan High Dam. A dynamic discharge system is proposed to re-originate lake salinity under climate change conditions. The multiphase models are applied on El-Burullus lake for further understanding of the lake hydrodynamic behavior and the effect of changing the fresh water routing on the lake stratification. Using the two-phase model, the lake was studied under actions of the total flux of fresh water and sea water level boundary conditions. The numerical simulation results revealed the necessity of the three dimensional study. Although, the 3D multiphase model has the potential to perform accurate numerical simulations, it requires very high computational resources. It is recommended to use short-term measured field data for future simulations.

Contents

List of Figures

LIST OF FIGURES

List of Tables

1

Introduction

Shallow coastal lagoons are a common feature of coastal environments which are a highly valued natural resource for society. In recent years, coastal lagoons have received more attention and concern regarding their increasing use for transportation, recreation activities and food production. They are also a highly productive systems that function as nursery areas and feeding grounds for coastal fishes and thereby potentially support important commercial and recreational fisheries (1). Barnes (2) has estimated that coastal lagoons occupy 13% of worldwide coastal areas. Coastal lagoons are influenced by winds, tides, freshwater flow and location of seawater input. These respective influences are determined by anthropogenic impacts, climate, erosion and sedimentation processes that modify connections and fluxes between the lagoon and its neighboring marine system. There are many alterations in coastal lagoons ecosystems. They are induced by eutrophication, pollution, hydrological imbalances and ecosystem modifications. Understanding the circulation within a lagoon and natural flushing by lagoon-shelf exchanges is fundamental to maintaining its ecological health as well as its economic value (3).

Figure 1.1 shows the major worldwide coastal lagoon districts (4). The Egyptian shallow coastal lakes are considered among those districts. Land-use changes and human activities combined with a growing population pose an increasing pressure on the natural values and ecological health of these lagoons. They are suffering from severe degradation of their ecosystem. The ultimate development of the Egyptian coastal lagoons through sustainable management plans is seen as an essential approach to avoid such degradation. Computational fluid dynamics is considered a powerful tool

to understand and analyze the performance of these plans. This study focuses on hydrodynamics and sediment transport numerical modeling for shallow coastal lagoons in order to develop the most adequate solution for its environmental management.

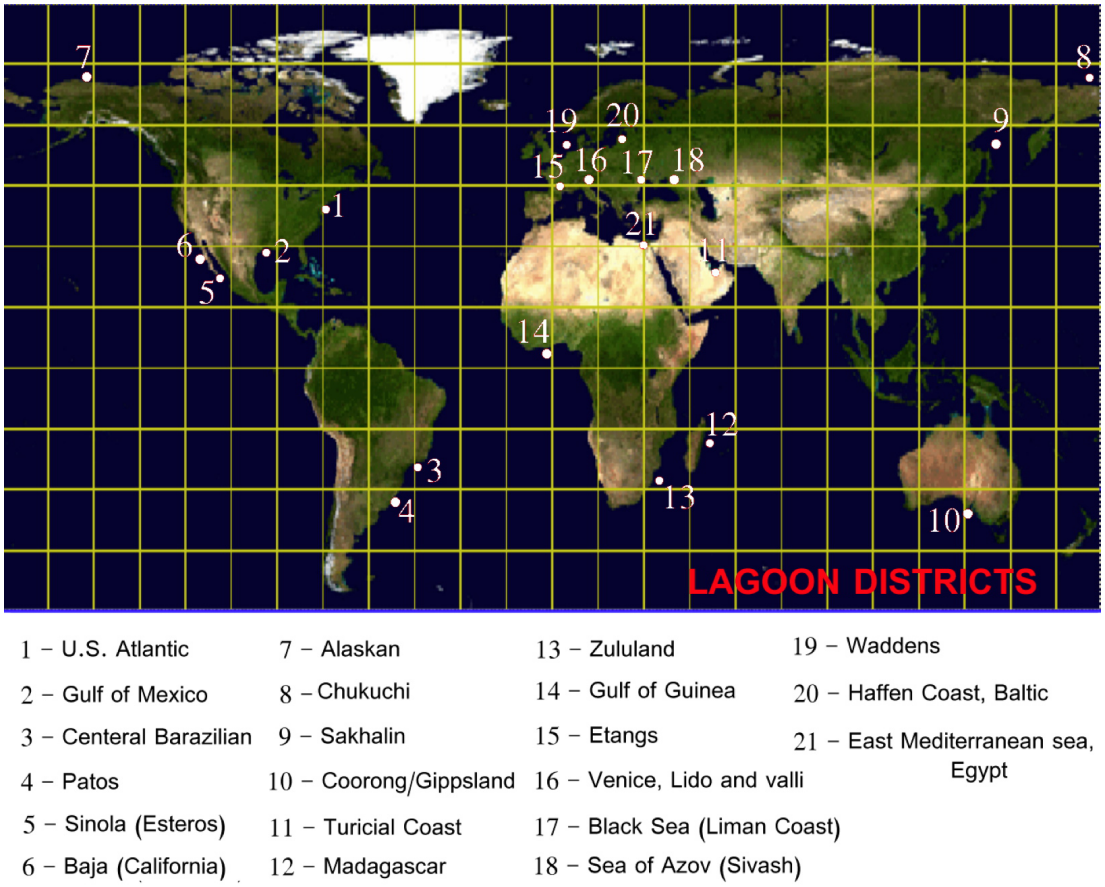

Figure 1.1: Worldwide distribution for major coastal lagoon districts.

1.1 The Egyptian Northern Coastal Lagoons

There are five lagoons along the north coast of Egypt. These lagoons are Maryout, Edku, Burullus, Manzala and Bardawil, as shown in Figure 1.2. They form 50% to 70% percent of the Egyptian northern coastline where each of them has specific characteristics (5) as shown in Table 1.1. Each Lagoon is subjected to a variety of pressures which may threaten existing economic, social and environmental aspects (6). The lagoons are commonly shallow with a varying salinity from brackish to hyper saline since

they are usually connected to the Mediterranean Sea via narrow inlets and are separated from the Sea by a narrow sand bar. The Mediterranean Sea tides govern water exchange in the lagoons. Several man-made wetlands are also found around the border including fish farms, salt-pans, canals and drains carrying water from irrigated fields. The gradient between the brackish part of the lake and marine waters provides a unique zone where many marine and fresh water organisms flourish. Lagoons are physiographic features that usually include a complex of various biotope types and habitats.

Table 1.1: Surface area and typology of northern coastal lagoons in Egypt.

	Maryot	**Edku**	**Burullus**	**Manzala**	**Bardwil**
Area (km^2)	50	80	410	780	660
Water salinity	Fresh water	Brackish water	Brackish water	Brackish water	Hyper saline
Drainage input (billion m^3)	2.2	1.4	4.0	3.7	-
Water depth (m)	0.4 - 0.8	0.3 - 2.0	0.4 - 2.4	0.4 - 3.0	0.0 - 2.2

The Egyptian northern coastal lagoons are a highly valued natural resource for the society. They support a network of significant ecological communities as well as a diverse range of recreational activities. Many of the coastal areas in north Egypt are in flat or low-lying areas, which are particularly vulnerable to flooding and inundation. Coastal wetlands are particularly important in the northern zone because they can help reduce flooding under the expected sea level rise. The lagoon plant vegetation provides habitat for many aquatic invertebrates which are considered food for larger animals such as fish or birds. In addition, they provide inhabitants with various activities as shown in Table 1.2 and Figure 1.3, as follows:

Fishing: Fishing is the leading economic activity in the coastal lakes which produces about 11% of the Egyptian total fish productivity in 2009, Figure 1.4.

Reed harvesting: Substantial amounts of reeds are cut and used for various purposes. Green shoots are used as fodder for livestock while the sun-dried stems are sold to be used in the demarcation of the cultivated fields on the sand bar or as building materials. Some of these reeds are woven into mats or used as wind breaks, fishing nets and in bird catching.

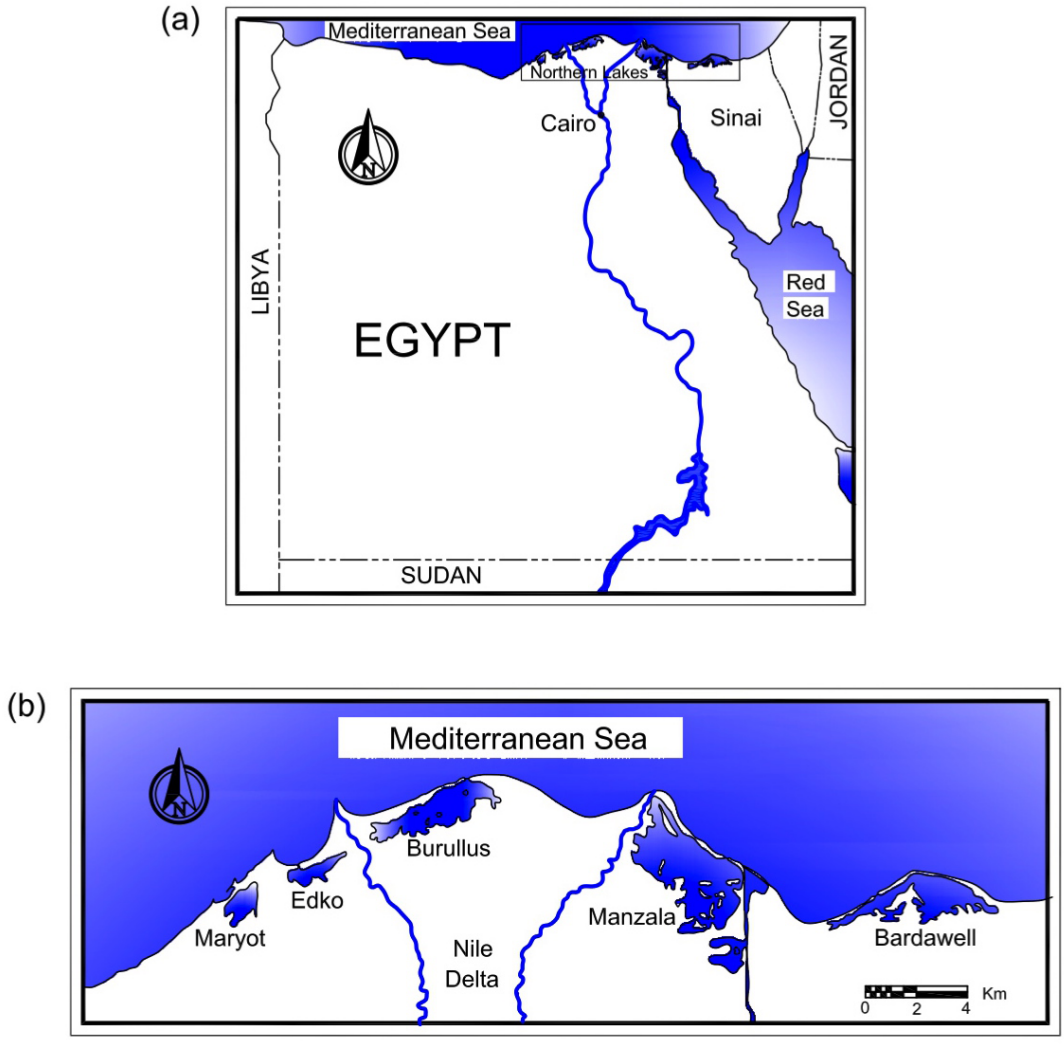

Figure 1.2: Geographical location of the Egyptian coastal lagoons: (a) location in Egypt and (b) shows the five coastal lagoons which are separated from the Mediterranean Sea by a narrow sand bar and are connected to the sea water through small inlets.

Bird hunting: Bird catching is a widespread activity in the coastal area, and is largely concentrated in the autumn and winter. Birds use lagoons as feeding grounds during migration or as breeding areas. Quail catching is a traditional activity along the entire Mediterranean coast of Egypt. The catch is usually transported to nearby towns and cities where it may be sold for a reasonable price.

Salt production: Commercial salt production is carried on the lakes shoreline. Solar evaporation is used to concentrate the lake waters to produce either salts or highly concentrated brine (water with high salt content).

Livestock breeding: Villagers around the lagoons shoreline breed herds of buffaloes, cows, sheep, goats and camels.

Tourism: A modest tourist industry has existed for a long time in the coastal area. It is based on attracting the Egyptian tourists during summer months.

Fish farming: Fish farming is a widespread and increasing activity along the shores of the lakes. It shares with 46% of the total fish productivity in Egypt, Figure 1.4. In the last decade, considerable areas have been allocated to aquaculture owing to availability of water and a much higher profitability than that achieved by agriculture.

Table 1.2: Activities carried out in the coastal lagoons zone (other than fisheries and aquaculture).

	Maryot	**Edku**	**Burullus**	**Manzala**	**Bardwil**
Reed harvesting	+++	+++	+++	+++	-
Bird hunting	+	++	+++	+++	++
Salt production	-	+	++	++	+++
Livestock breeding	+	++	+++	+++	+
Tourism	-	+	++	++	++
Shipyard	-	-	+	+	+

1.2 Statement of The Problem

Egyptian coastal northern lakes suffered from various problems which might lead to environmental degradation, shortage in fish catch and substantial changes in its ecosystem. Among those lakes is El-Burullus Lake which will be more or less representative of the Egyptian coastal lagoons in this study. El-Burullus lagoon brackish water is one of the most important Egyptian northern lakes from an economical point of view. This lake produces about 40% of fish productivity of the northern lakes in Egypt. Several

Figure 1.3: Different activities around Egyptian northern coastal lagoon, El-Burullus Lake.

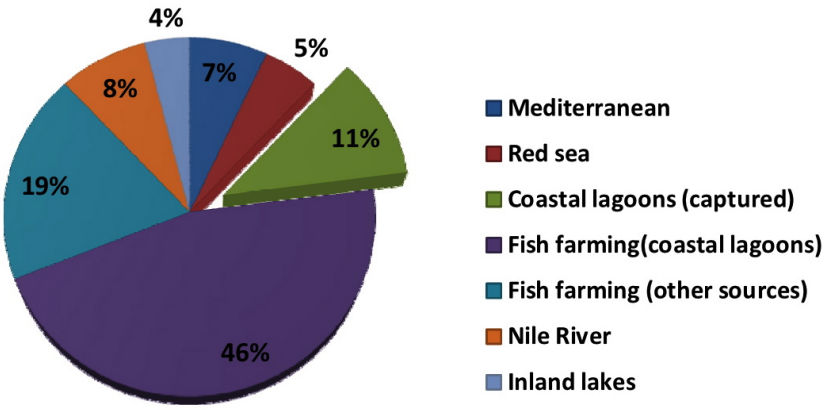

Figure 1.4: Classification of fish production in Egypt, 2009.

studies have been carried out on the different aspects of the lake ecology (7, 8), which showed that the water quality of the lake has changed over time. Lake Burullus was predominantly saline in the northern zone and brackish in the southern zone, with a salinity gradient between both zones. Following the completion of the Aswan High Dam on the Nile River in 1965, the fresh water resources became fully regulated and this lead to an increase in the intensity of agricultural irrigation and synthetic fertilizer consumption. This dramatic change leads to a rise in the amounts of agricultural drainage received by the lagoon before they are discharged to the eastern Mediterranean Sea through a small breach-way. It is now almost brackish throughout the entire basin. In particular, salinity values were significantly high for various areas during 1973 compared with 2002 (9, 10), as shown in Figure 1.5.

According to the Egyptian Environmental Affairs Agency (EEAA), these factors have led to; (i) substantial reed growth (Phragmites australis) extending coverage over a major part of the Lake's area, (ii) changes in the species composition of the fauna and flora, and (iii) socio-economic consequences as a result of changes in commercial fish availability from highly-prized marine species to the much cheaper tilapia. In 2002, EEAA (11) introduced a management plan in order to restore the Lake's ecological system. They included five main long-term objectives to be achieved by 2010 through field actions (programs and projects) and establishment of effective institutional arrangements. These objectives were: (1) restoring the ecological and landscape values

which have been lost or damaged, (2) maintaining and enhancing the ecological and landscape values of the site, (3) conserving El-Burullus Lake natural resources through sustainable management, (4) improving socio-economic conditions for local people, and (5) developing public awareness and respecting for nature conservation. In addition, some suggestions were introduced to restore the Lake's natural hydrological system:

- Re-institute the procedure of "winter closure" in the southern outskirts of Lake Burullus.
- Divert part of the drainage water (i) to be reused in newly reclaimed lands, or (ii) to directly flow to the sea.
- Maintain the sea inlet to keep it opened and clear to ease seawater flow into the Lake.

Although, these suggestions are valuable and could be effective, Younes and Nafea (12) concluded that the lake ecological conditions are still in degradation. Figure 1.5 shows a slight decrease in salinity values at the middle and western area of the lake in 2011 are than 2002. Salinity values in 2011 still very low and almost no improvement was achieved through such management plan. Management practices in coastal lagoons notably act on the control of freshwater inflow and connections with the sea (13, 14). Understanding the influence of connections and fluxes on lagoon fauna is important to be able to predict the ecological impacts of management plans (14, 15). Therefore, a reliable and effective management of coastal lakes should be based on a clear insight into the physics of the lake hydrodynamics.

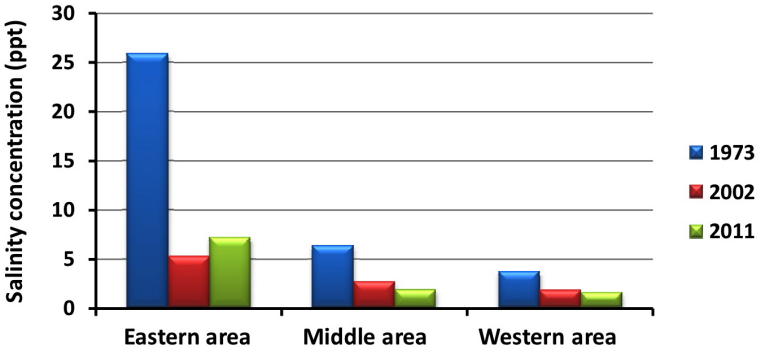

Figure 1.5: Salinity values inside El-Burullus lagoon in the eastern, middle and western area during 1973, 2002 and 2011.

1.3 About The Dissertation

1.3.1 Objective of the research

Coastal lagoons experience forcing from river input, wind stress, tides, precipitation to evaporation balance, and surface heat balance. Water and salt balances, lagoon water quality, and eutrophication depend critically on lagoon circulation, salt and material dispersion, water exchange through the sea connected canal(s) as well as residence or flushing times. The understanding of physical hydrodynamics, circulation and ecological dynamics of the lagoons is important for planning and implementation of management strategies in coastal lagoons. Figure 1.6 shows the different parameters included in this study to sustainably manage El-Burullus coastal lagoon.

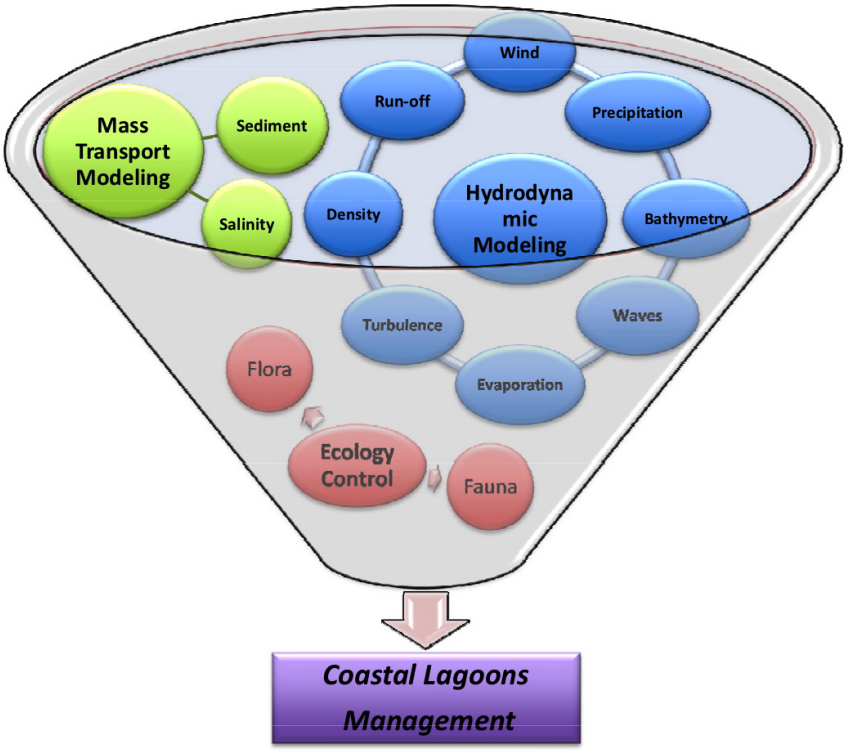

Figure 1.6: Various parameters included in this study to sustainably manage El-Burullus lagoon, Egypt.

The main objectives of this study are summarized as follows.

1. The overall aim of the proposed study is to provide a comprehensive understand-

ing of El-Burullus shallow coastal lagoon's hydrodynamic physical process that influence its environmental conditions to identify enhancement, development and management needs to ensure the long-term ecological sustainability of the Lagoon.

2. Develop numerical models (hydrodynamic modeling and mass transport model) that can simulate the coastal lakes as well as its related processes (that is, hydrodynamic and sedimentary processes, including tidal behavior, freshwater inputs, water balance, mixing, exchange with the Mediterranean Sea, density current, geomorphological characteristics and sediment movement).

3. To determine which forcing parameters control the lagoon's salinity regime.

4. If possible, to investigate possible means of restoring them to the desired state as before Aswan High Dam Construction.

5. The likely impacts of future climate change including sea-level rise.

6. To this may be added, integrate the hydrodynamic model and sediment transport model to evaluate the lake sedimentation problems.

1.3.2 Outlines of the dissertation

This dissertation concerns the numerical study of El-Burullus coastal lagoon hydrodynamics and mass transport based on recent advances in numerical solutions. To the best of the author's knowledge, it is the first hydrodynamic model that simulates El-Burullus Lagoon and it is applicable for all the Egyptian coastal lagoons. The present dissertation is organized in eight chapters. In this chapter, the importance of the Egyptian coastal lagoons, the motivation and the objectives of this study, together with a brief introduction of the dissertation contents are presented.

Chapter 2 provides the details of the depth-averaged mass transport model governing equations and its discretization. In addition, a high performance computing system is introduced to shorten the computational time. The model is validated against analytical solution of the advection diffusion equation and experimental measurements for transported concentration cloud in a meandering channel.

Chapter 3 describes El-Burullus lagoon study area, the lake problems, and the field data which are used to calibrate the model. The model is applied on the lake to simulate its salinization process. Five scenarios were studied for further understanding of the lake circulation and salinity dynamics and to investigate possible means of restoring them to the desired state as before Aswan High Dam Construction. These scenarios revealed the importance of fresh drainage water discharges into the lake and the possibility to change the discharge routing.

Chapter 4 outlines the model application to investigate the impact of climate change on salinization process in El-Burullus Lake. The model is used to predict the salinization and circulation processes occurring under the effect of two global emissions scenarios (SRES A2 and SRES B1). Through numerical simulation, a dynamic discharge system is proposed to re-originate the lake's salinity under climate change conditions.

Chapter 5 introduces a depth-averaged sediment transport model. The partial differential equations for 2D shallow water flow, suspended-load, bed-load sediment and bed evolution are incorporated to predict the bed morphological changes. Two approaches of sediment transport modeling are introduced: the equilibrium and the non-equilibrium approaches taking into account current and wave actions in coastal areas. The developed model is validated against different scour problems and its validity is examined. Also, a comparison between the results of the two approaches is discussed.

Chapter 6 contains the 2D vertical multi-phase flow model's governing equations and the modeling numerical procedures. The computational method is described including the open multiprocessing computation technique. The model is validated against the Boussinesq and non-Boussinesq lock exchange problems. In addition, it is applied on Ohashi River to validate its applicability. Finally, it is used to simulate El-Burullus lake breach-way.

Chapter 7 presents 3D computational multi-phase flow model's governing equations and numerical procedures. The model is validated against the Boussinesq and non-Boussinesq lock exchange problems. In addition, The model is applied on

experimental results for Shinji-Nakaumi brackish coastal lakes system to test its applicability.

Chapter 8 summarizes all contributions of this study.

2

Depth-averaged Mass Transport Model

In this chapter, a two-dimensional depth-averaged mass transport model is developed to simulate shallow coastal lakes under actions of wind, waves, tidal current, rain, evaporation, and effluent flows from drains and rivers. MAC method on collocated grid for shallow water equations (MACS) is used to solve the flow governing equations. This algorithm was originally proposed using structured collocated grid and it was confirmed that this method is able to predict dam-break problems, hydraulic jumps, sub-critical and super-critical flows stably and accurately without artificial diffusions, (16, 17). Yamashita and Ushijima (18) extended this algorithm for unstructured collocated grid system. This research builds on recent advances for numerical solutions to couple numerical processes of hydrodynamic and mass transport equations using the finite volume method (FVM) in discretization. Further, on the basis of a domain decomposition method, the unstructured cells are decomposed into multiple sub-domains and their computations are simultaneously performed with the distributed-memory system. This method is implemented by message-passing interface (MPI) which allows us to significantly reduce the elapsed time of computation. The predicted model was verified against analytical solution of the advection diffusion equation and experimental measurements for transported concentration cloud in a meandering channel.

2.1 Governing Equations and Discreatization

2.1.1 Flow governing equations

The governing equations for flow are the shallow water equations, Eq.(2.1)-Eq.(2.3), which describe the flow conditions in the horizontal domain Ω and appear in the integral form as follows:

$$\int_{\Omega} \frac{\partial h}{\partial t}\, d\Omega + \oint_{\partial\Omega} \boldsymbol{M}\cdot\boldsymbol{n}\, dl = \int_{\Omega} Q_h\, d\Omega \tag{2.1}$$

$$\int_{\Omega} \left(\frac{\partial M_i}{\partial t} - \frac{\tau_{bi}+\tau_{si}+\nabla \boldsymbol{S}}{\rho} \right) d\Omega = \oint_{\partial\Omega} \boldsymbol{F}_i \cdot \boldsymbol{n}\, dl \tag{2.2}$$

with

$$\boldsymbol{F}_i = -M_i\boldsymbol{u} - g\, h(H\boldsymbol{k}_i) + \nu_t \nabla M_i \tag{2.3}$$

where t is time and h is the water depth which is defined as $H - z_b$; H and z_b are water surface and bed levels measured from a horizontal datum as shown in Figure 2.1; g and ρ are the gravity acceleration and the density of the fluid, respectively, which are assumed to be constant; $\boldsymbol{n}$ is the unit normal vector on the domain boundary $\partial\Omega$ towards the outside direction; $\boldsymbol{u}$ is the depth-averaged velocity vector; $\boldsymbol{M}$ is the vector representing the flow rate of unit width, $\boldsymbol{M} = \boldsymbol{u}h$; M_i is the unit width flow rate with subscript $i = 1$ and 2 representing unit flow rate in x- and y-directions; x and y are the horizontal orthogonal coordinates; Q_h is the volumetric source/sink term including rain and evaporation; $\boldsymbol{k}_i$ is a unit vector in x_i direction; and $\boldsymbol{\tau}_b$ is the shear stress at bed level which is modeled using Manning formula:

$$\frac{\tau_{bi}}{\rho} = -\frac{g\, n^2\, |\boldsymbol{u}|\, M_i}{h^{4/3}} \equiv -\lambda M_i \tag{2.4}$$

where n is a Manning roughness coefficient and $|\boldsymbol{u}| = \sqrt{u_1^2 + u_2^2}$.
The eddy viscosity ν_t is expressed using the parabolic eddy viscosity model:

$$\nu_t = \alpha\, u_*\, h \tag{2.5}$$

where α is an empirical coefficient, set as 0.05-0.3 in this study, and u_* is the friction velocity. Surface shear stress $\boldsymbol{\tau}_s$ at water surface is usually computed as (19):

$$\tau_{si} = C_D\, \rho_a |\boldsymbol{u_w}| u_{wi} \tag{2.6}$$

where C_D is the drag coefficient, set as 1.125x10^{-3}; ρ_a is air density, set as 1.176 kg.m^{-3}; u_{wi} is the wind velocity component in x_i direction; and $|\boldsymbol{u_w}| = \sqrt{u_{w1}^2 + u_{w2}^2}$. The wave radiation stress vector $\boldsymbol{S}$ is represented based on linear wave theory (20) by:

$$S = \begin{bmatrix} S_{xx} \cdot n_1 + S_{xy} \cdot n_2 \\ S_{yx} \cdot n_1 + S_{yy} \cdot n_2 \end{bmatrix} \tag{2.7}$$

$$S_{xx} = \frac{1}{2} E(1+G)cos^2\theta + G \tag{2.8}$$

$$S_{xy} = S_{yx} = \frac{1}{2} E(1+G)cos\theta sin\theta \tag{2.9}$$

$$S_{yy} = \frac{1}{2} E(1+G)sin^2\theta + G \tag{2.10}$$

with

$$E = \frac{1}{8}\rho g {h_w}^2 \quad and \quad G = \frac{2kh}{sinh(2kh)} \tag{2.11}$$

where h_w is the wave height; k is the wave number; n_1 and n_2 are normal unit vectors in x- and y-direction, respectively; and θ is the angle between wave crest and x-axis.

2.1.2 Flow governing equations discretization

The flow governing equations are discretized using the Finite Volume Method (FVM) which are evaluated by divergence theorem for unstructured collocated grid system where the C-ISMAC method (21) is used. Eq.(2.1) - Eq.(2.3) can be written as:

$$\frac{h^{n+1} - h^n}{\Delta t} \Delta S = \oint_{\partial\Omega} m_i^{n+1} \cdot \boldsymbol{n} \; dl + \int_{\Omega} Q_h \; d\Omega \tag{2.12}$$

or

$$h^{n+1} = h^n - \frac{\Delta t}{\Delta S} \sum_{k=1}^{3} \boldsymbol{m}_k^{n+1} \cdot \boldsymbol{n}_k \; l_k + \Delta t \; Q_h \tag{2.13}$$

and

$$\begin{aligned} \frac{M_i^{n+1} - M_i^n}{\Delta t} \Delta S = & - x_1 \oint_{\partial\Omega} M_i^{n+1} \boldsymbol{u}^n \cdot \boldsymbol{n} \; dl - (1-x_1) \oint_{\partial\Omega} M_i^n \boldsymbol{u}^n \cdot \boldsymbol{n} \; dl \\ & + x_2 \nu_t \oint_{\partial\Omega} \nabla M_i^{n+1} \cdot \boldsymbol{n} \; dl + (1-x_2)\nu_t \oint_{\partial\Omega} \nabla M_i^n \cdot \boldsymbol{n} \; dl \\ & - g h^n \oint_{\partial\Omega} (H^n \boldsymbol{k}_i) \cdot \boldsymbol{n} \; dl - \oint_{\partial\Omega} \boldsymbol{S} \cdot \boldsymbol{n} \; dl \\ & - \int_{\Omega} \lambda M_i^n \; d\Omega - \int_{\Omega} \tau_{si} \; d\Omega \end{aligned} \tag{2.14}$$

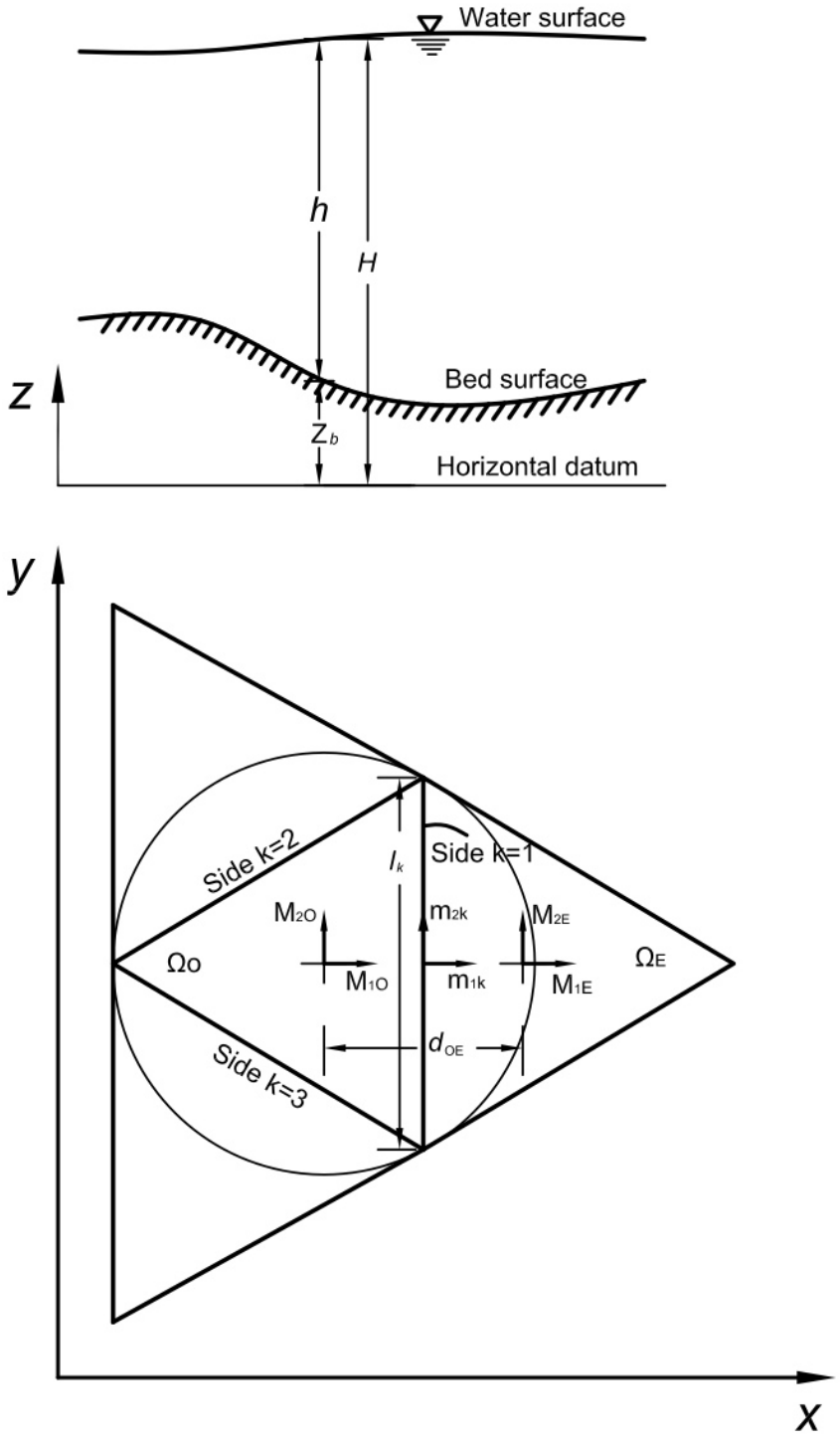

Figure 2.1: Schematic sketch for the unstructured mesh and the model parameters.

where m_i is the unit flux vector at the cell boundary in i direction; $\boldsymbol{m}_k$ stands for $(m_{1k},\ m_{2k})$, see Figure 2.1; and x_1 and x_2 are parameters that control the implicit and explicit weight for convection and diffusion terms. In the C-ISMAC method, the following relationship can be used:

$$M_i^{n+1} = M_i^n + \tilde{M}_i \tag{2.15}$$

Substituting Eq.(2.15) into Eq.(2.14), the following linear equation system is used to get $\tilde{M}_i$ for all cells as:

$$\begin{aligned}\tilde{M}_{io} + \frac{\Delta t}{\Delta S}\sum_{k=1}^{3}(x_1\tilde{C}_{ik} - x_2\tilde{D}_{ik})\ l_k &= \frac{\Delta t}{\Delta S}\sum_{k=1}^{3}(-C_{ik} + D_{ik})\ l_k \\ - gh_o^n\frac{\Delta t}{\Delta S}\sum_{k=1}^{3}H_{ok}^n n_{ki}\ l_k - \frac{\Delta t}{\Delta S}\sum_{k=1}^{3}S_{ki}n_{ki}\ l_k &- \lambda M_{io}^n\Delta t - \tau_{sio}\Delta t\end{aligned} \tag{2.16}$$

with

$$C_{ik} = \frac{1}{2}(U_k^n - |U_k^n|)M_{iE}^n + \frac{1}{2}(U_k^n + |U_k^n|)M_{io}^n \tag{2.17}$$

$$\tilde{C_{ik}} = \frac{1}{2}(U_k^n - |U_k^n|)\tilde{M}_{iE} + \frac{1}{2}(U_k^n + |U_k^n|)\tilde{M}_{io} \tag{2.18}$$

$$D_{ik} \approx \nu_t\frac{M_{iE} - M_{io}}{d_{oE}} \tag{2.19}$$

$$\tilde{D_{ik}} \approx \nu_t\frac{\tilde{M}_{iE} - \tilde{M}_{io}}{d_{oE}} \tag{2.20}$$

where l_k is the mesh side length on a k side number; The convection flux is calculated by the first-order upwind method, as presented in Eq.(2.17) and Eq.(2.18); U_k^n stands for $\boldsymbol{u}^n|_k \cdot \boldsymbol{n}_k$; M_{iE} and M_{io} are defined at the cell-center of the element E and o, respectively as shown in Figure 2.1; and the diffusion term is approximated as shown in Eq.(2.19) and Eq.(2.20). In the collocated grid system, Ushijima et al. (16, 17) identify the importance of removing source terms (i.e. water level gradient, wave radiation stress, bottom friction stress and surface stress) to improve the numerical stability and accuracy. As a result, a tentative flux M_i^* at cell center for all cells can be calculated by removing such source terms as:

$$\begin{aligned}M_{io}^* = M_{io}^n + \tilde{M}_{io} \\ + gh_o^n\frac{\Delta t}{\Delta S}\sum_{k=1}^{3}H_{ok}^n n_{ki}\ l_k + \frac{\Delta t}{\Delta S}\sum_{k=1}^{3}S_{ki}n_{ki}\ l_k + \lambda M_{io}^n\Delta t + \tau_{sio}\Delta t\end{aligned} \tag{2.21}$$

Then the tentative flux m_i^* at cell boundary can be calculated by taking the arithmetic average of the cell center values as:

$$m_{ik}^* = f(M_{io}^*, M_{iE}^*) \tag{2.22}$$

In MACS method, in order to get the flux m_{ik}^{n+1} at n+1 time step, the source terms are added at the cell boundaries where the water level H is treated implicitly as follows:

$$\begin{aligned} m_{ik}^{n+1} &= m_{ik}^* \\ &- g h_{bk}^n \frac{\Delta t}{\Delta S_{oE}} (H_E^{n+1} - H_o^{n+1}) n_{ki} l_k - \frac{\Delta t}{\Delta S} \sum_{k=1}^{3} S_k n_{ki}\ l_k - \lambda m_{ik}^n \Delta t - \tau_{sio} \Delta t \end{aligned} \tag{2.23}$$

On the other hand, if the water level H is treated explicitly, we get:

$$\begin{aligned} \hat{m}_{ik}^* &= m_{ik}^* \\ &- g h_{bk}^n \frac{\Delta t}{\Delta S_{oE}} (H_E^n - H_o^n) n_{ki} l_k - \frac{\Delta t}{\Delta S} \sum_{k=1}^{3} S_k n_{ki}\ l_k - \lambda m_{ik}^n \Delta t - \tau_{sio} \Delta t \end{aligned} \tag{2.24}$$

Subtracting Eq.(2.24) from Eq.(2.23):

$$m_{ik}^{n+1} = \hat{m}_{ik}^* - g h_{bk}^n \frac{\Delta t}{\Delta S_{oE}} (\phi_E - \phi_o) n_{ki} l_k \tag{2.25}$$

in which,

$$\phi_E = H_E^{n+1} - H_E^n \approx h_E^{n+1} - h_E^n \tag{2.26}$$

Substituting Eq.(2.25) into continuity equitation Eq.(2.13), the linear relationship for ϕ_o and ϕ_E is obtained:

$$\phi_o^n \left[1 + \frac{g(\Delta t)^2}{\Delta S} \sum_{k=1}^{3} \frac{h_k^n l_k^2}{\Delta S_{oE}} \right] - \frac{g(\Delta t)^2}{\Delta S} \sum_{k=1}^{3} \frac{h_k^n l_k^2}{\Delta S_{oE}} \phi_k^n = -\frac{\Delta t}{\Delta S} \sum_{k=1}^{3} \boldsymbol{m}_k^* \cdot \boldsymbol{n}_k l_k \tag{2.27}$$

By solving the linear system given by Eq.(2.27), ϕ_o can be determined and m^{n+1} can be estimated from Eq.(2.23). The water depth h^{n+1} can be calculated using Eq.(2.13). Once h^{n+1} is calculated, M^{n+1} at the cell center is obtained by adding source terms to M^*, which already was calculated with Eq.(2.21).

$$M_i^{n+1} = \frac{1}{1 + \lambda \Delta t} \left[M_i^* - \frac{\Delta t}{\Delta S} g h^{n+1} \sum_{k=1}^{3} H_k^{n+1} n_{ki} l_k - \frac{\Delta t}{\Delta S} \sum_{k=1}^{3} S_k\ n_{ki}\ l_k - \tau_{sio} \Delta t \right] \tag{2.28}$$

2.1.3 Mass transport equation

The transported concentration can be obtained by solving the advection diffusion equation, Eq.(2.29):

$$\int_{\Omega} \frac{\partial hc}{\partial t}\, d\Omega + \oint_{\partial\Omega} \beta h \boldsymbol{u} c \cdot \boldsymbol{n}\, dl = \oint_{\partial\Omega} \frac{\nu_t}{\sigma_c} h \nabla c \cdot \boldsymbol{n}\, dl + \int_{\Omega} (E - D)\, d\Omega \tag{2.29}$$

where c is the depth-averaged concentration of transported material; and σ_c is turbulent Schmidt number for concentration diffusion, which represents the ratio of eddy viscosity to eddy diffusivity; β is a correction factor representing the ratio between depth averaged transported concentration and flow velocities; and $(E - D)$ is the source term which represents sink or source to the transported material.

2.1.4 Mass transport equation discretization

The advection diffusion equation is discretized using the FVM which is evaluated by divergence theorem for unstructured collocated grid system using the C-ISMAC method (21) and similar to the momentum equation of the flow governing equations. Let $Q = hc$, Eq.(2.29) can be written as:

$$\int_{\Omega} \frac{\partial Q}{\partial t}\, d\Omega + \oint_{\partial\Omega} \beta \boldsymbol{u} Q \cdot \boldsymbol{n}\, dl = \oint_{\partial\Omega} \frac{\nu_t}{\sigma_c} \nabla Q \cdot \boldsymbol{n}\, dl + \int_{\Omega} (E - D)\, d\Omega \tag{2.30}$$

$$\begin{aligned} \frac{Q^{n+1} - Q^n}{\Delta t} \Delta S = &- x_1 \oint_{\partial\Omega} Q^{n+1} \boldsymbol{u}^n \cdot \boldsymbol{n}\, dl - (1 - x_1) \oint_{\partial\Omega} Q^n \boldsymbol{u}^n \cdot \boldsymbol{n}\, dl \\ &+ x_2 \frac{\nu_t}{\sigma_c} \oint_{\partial\Omega} \nabla Q^{n+1} \cdot \boldsymbol{n}\, dl + (1 - x_2) \frac{\nu_t}{\sigma_c} \oint_{\partial\Omega} \nabla Q^n \cdot \boldsymbol{n}\, dl \\ &+ \int_{\Omega} (E - D)\, d\Omega \end{aligned} \tag{2.31}$$

In the CISMAC method, the following relationship can be used;

$$Q^{n+1} = Q^n + \tilde{Q} \tag{2.32}$$

Substituting (Eq. 24) into (Eq. 23), the following linear equation system is used to get $\tilde{Q}$ for all cells as:

$$\tilde{Q}_o + \frac{\Delta t}{\Delta S} \sum_{k=1}^{3} (x_1 \tilde{C Q_k} - x_2 \tilde{D Q_k})\, l_k = \frac{\Delta t}{\Delta S} \sum_{k=1}^{3} (-C Q_k + D Q_k)\, l_k + (E - D)\Delta t \tag{2.33}$$

with

$$CQ_k = \frac{1}{2}(U_k^n - |U_k^n|)Q_E^n + \frac{1}{2}(U_k^n + |U_k^n|)Q_o^n \tag{2.34}$$

$$C\tilde{Q}_k = \frac{1}{2}(U_k^n - |U_k^n|)\tilde{Q}_E + \frac{1}{2}(U_k^n + |U_k^n|)\tilde{Q}_o \tag{2.35}$$

$$DQ_k \approx \frac{\nu_t}{\sigma_c}\frac{Q_E - Q_o}{d_{oE}} \tag{2.36}$$

$$D\tilde{Q}_k \approx \frac{\nu_t}{\sigma_c}\frac{\tilde{Q}_E - \tilde{Q}_o}{d_{oE}} \tag{2.37}$$

where Q_E and Q_o are defined at the cell-center of the element E and o, respectively; and d_{oE} is the distance between these cells' centers as shown in Figure 2.2. Once Q^{n+1} is calculated using Eq.(2.32), the depth averaged concentration c is estimated as $c = Q/h$.

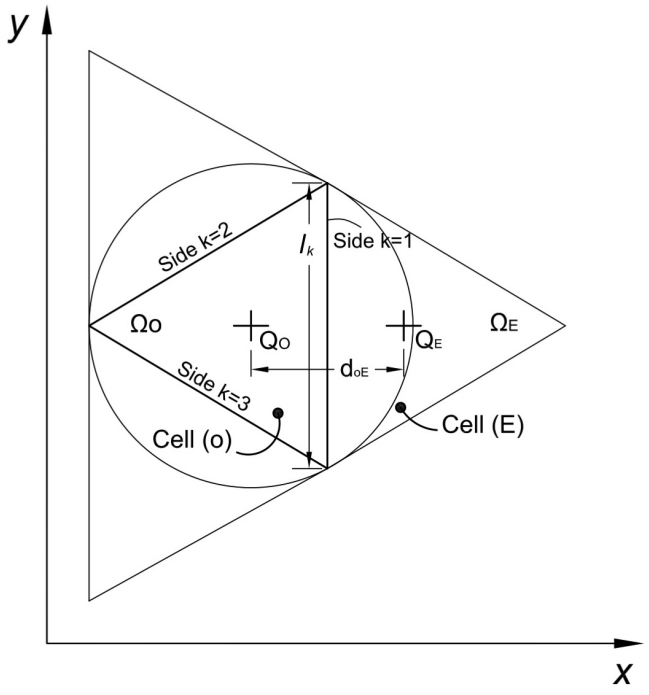

Figure 2.2: Definition sketch for the mass transport model parameters.

2.2 Boundary Conditions

Boundary condition is needed at the inlet and outlet in order to derive a well-imposed solution for the flow and mass transport equations according to flow regime; subcritical or supercritical. In this study, only the subcritical flow case is considered below.

2.2.1 Flow boundary conditions

Wall boundary conditions: The velocity at the wall is non-slip and has a value of zero and the water depth gradient is set to zero.
Inflow boundary conditions: Inlet boundary condition is usually a time series of unit width flux or flow velocity and it is essentially to determine the flow direction in the x- and y-directions. The water depth gradient is set to zero.
Outflow boundary conditions: The boundary condition at the outlet is the measured water stage while the gradient of velocity along the flow direction at the outlet boundary is set to zero.

2.2.2 Mass transport boundary conditions

Wall boundary condition: The mass-transported concentration gradient is set to zero.
Inflow boundary conditions: The mass-transported concentration must be given at each point of the inflow boundary.
Outflow boundary conditions: The mass-transported concentration gradient in the flow direction is set to zero.

2.3 High Performance Computing System

The computational method is performed based on high performance computing system. The domain of the generated unstructured cells is decomposed with METIS library (Karypis and Kumar (22), 1998) which is a free Package for domain decomposition into various subdomains. The computations are implemented by a group of processors. Each processor is responsible on a subdomain where computations are simultaneously performed with the distributed-memory system. The code is implemented using MPI (23) for distributed-memory system which is a library for communicating data messages between different subdomains at the sub-domains' boundaries as shown in Figure

2.3. Supercomputer at Kyoto University was used to perform these computational processes. Using the high performance computing system method significantly decreases the computational time as well as the necessary memory capacity in each processor.

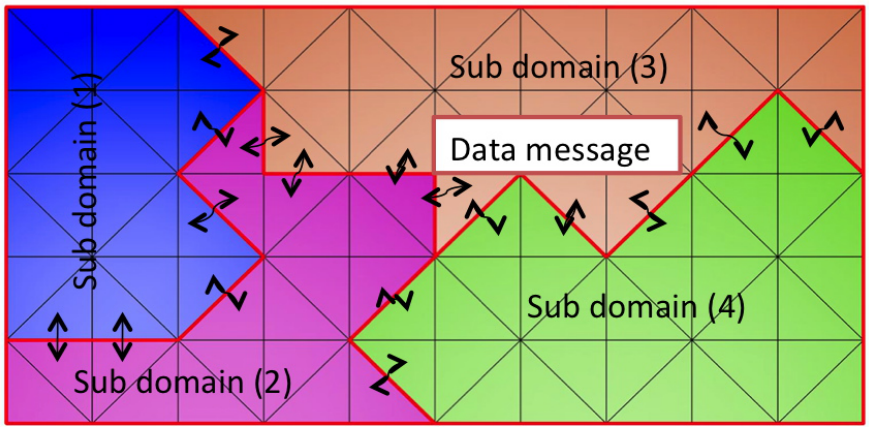

Figure 2.3: Domain decomposition method and data messages between various subdomains using MPI.

2.4 Model Validation

The present model has been tested to evaluate its applicability. Therefore, it was applied to predict mass transported materials and compared with analytical solution and experimental data. The simulation results in these test cases are described below.

2.4.1 Comparison with analytical solution

Transport model has been verified using analytical solution of the advection diffusion equation subjected to a continuous load of substance concentration for finite duration. An analytical solution given by Runkel (24) is used:

$$C(x,t) = \frac{C_o}{2}\left\{\exp\left[\frac{Ux}{2D}(1-\Gamma)\right]\operatorname{erfc}\left(\frac{x-Ut\Gamma}{2\sqrt{Dt}}\right)\right.$$
$$\left.+\exp\left[\frac{Ux}{2D}(1+\Gamma)\right]\operatorname{erfc}\left(\frac{x+Ut\Gamma}{2\sqrt{Dt}}\right)\right\}(t \le t_f) \tag{2.38}$$

$$C(x,t) = \frac{C_o}{2}\Bigg\{\exp\left[\frac{Ux}{2D}(1-\Gamma)\right]\left[\text{erfc}\left(\frac{x-Ut\Gamma}{2\sqrt{Dt}}\right)\right.$$
$$\left.-\text{erfc}\left(\frac{x-U(t-t_f)\Gamma}{2\sqrt{D(t-t_f)}}\right)\right]+\exp\left[\frac{Ux}{2D}(1+\Gamma)\right]$$
$$\left[\text{erfc}\left(\frac{x+Ut\Gamma}{2\sqrt{Dt}}\right)-\text{erfc}\left(\frac{x-U(t-t_f)\Gamma}{2\sqrt{D(t-t_f)}}\right)\right]\Bigg\}(t>t_f) \tag{2.39}$$

with

$$\Gamma = \sqrt{1+\frac{2K_dD}{U^2}} \tag{2.40}$$

For the tested channel shown in Figure 2.4, the channel length is 15 m, constant velocity $(U) = 0.30$ m/sec, and mixing coefficient (D) or $(\nu_t/\sigma_c) = 0.3$ m^2/sec. The initial injected concentration (C_o) is 100 g/m^3 for finite duration $(t_f) = 5$ seconds, and a decay factor, $k_d = 0$. Figure 2.5 shows a coincidence between the calculated and the theoretical results for $\beta = 0.96$ which will be used for all consequent simulations.

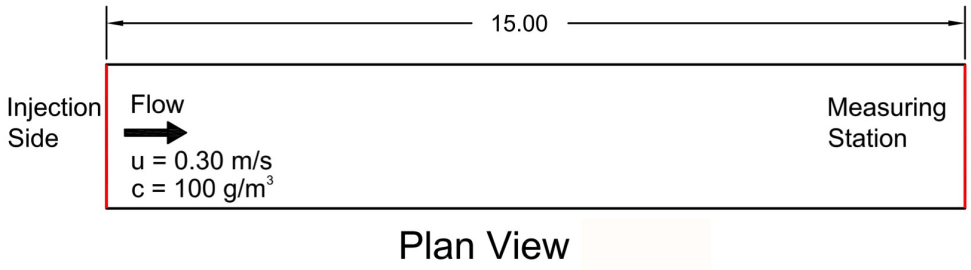

Figure 2.4: Schematic sketch for the test channel.

2.4.2 Comparison with experimental measurements

The model was applied to the experimental results obtained by Beak et al. (25) who has carried out a series of experiments in S-curved laboratory channels for transient tracer. Case 101 for left-bank tracer injection was selected in this study. The experiments were conducted in a 15 m long, 1 m wide and 0.6 m deep. It consisted of circular arcs connected by straight sections as shown in Figure 2.6. The initial concentration of the injected tracer was 100,000 g/m^3. Figure 2.7 and Figure 2.8 compare the computed and measured results for velocity field and the transient concentration cloud, respectively.

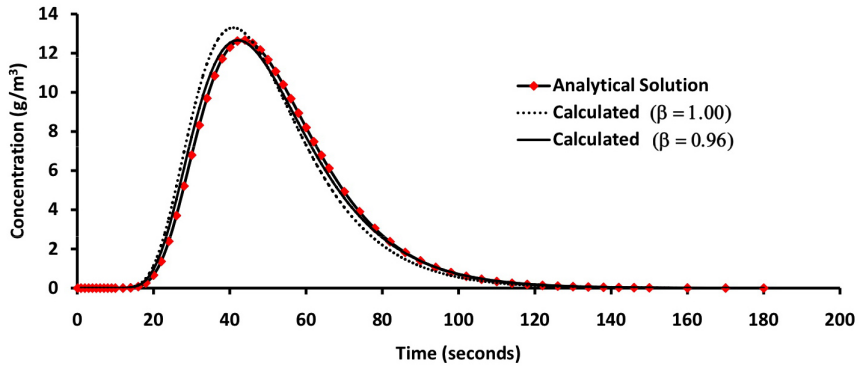

Figure 2.5: The time series of concentration at channel downstream section for theoretical solution and simulated results.

The comparison between predicted and measured results shows a good spatial and temporal agreement.

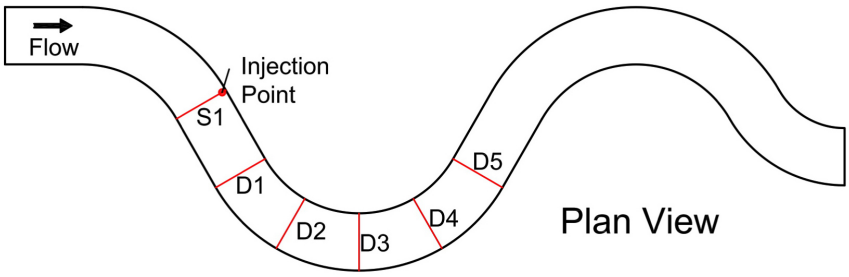

Figure 2.6: Schematic sketch for meandering channel.

2.5 Summary

A depth-averaged mass transport model based on MACS algorithm for shallow water equations coupled with mass transport equation has been developed. The computational method was performed based on high performance computing system; domain decomposition method and MPI for distributed memory system. This model is able to predict mass transported concentrations in shallow waters. The model has been successfully verified against analytical solution to the advection diffusion equation and experimental measurements to the transported concentration cloud in a meandering channel.

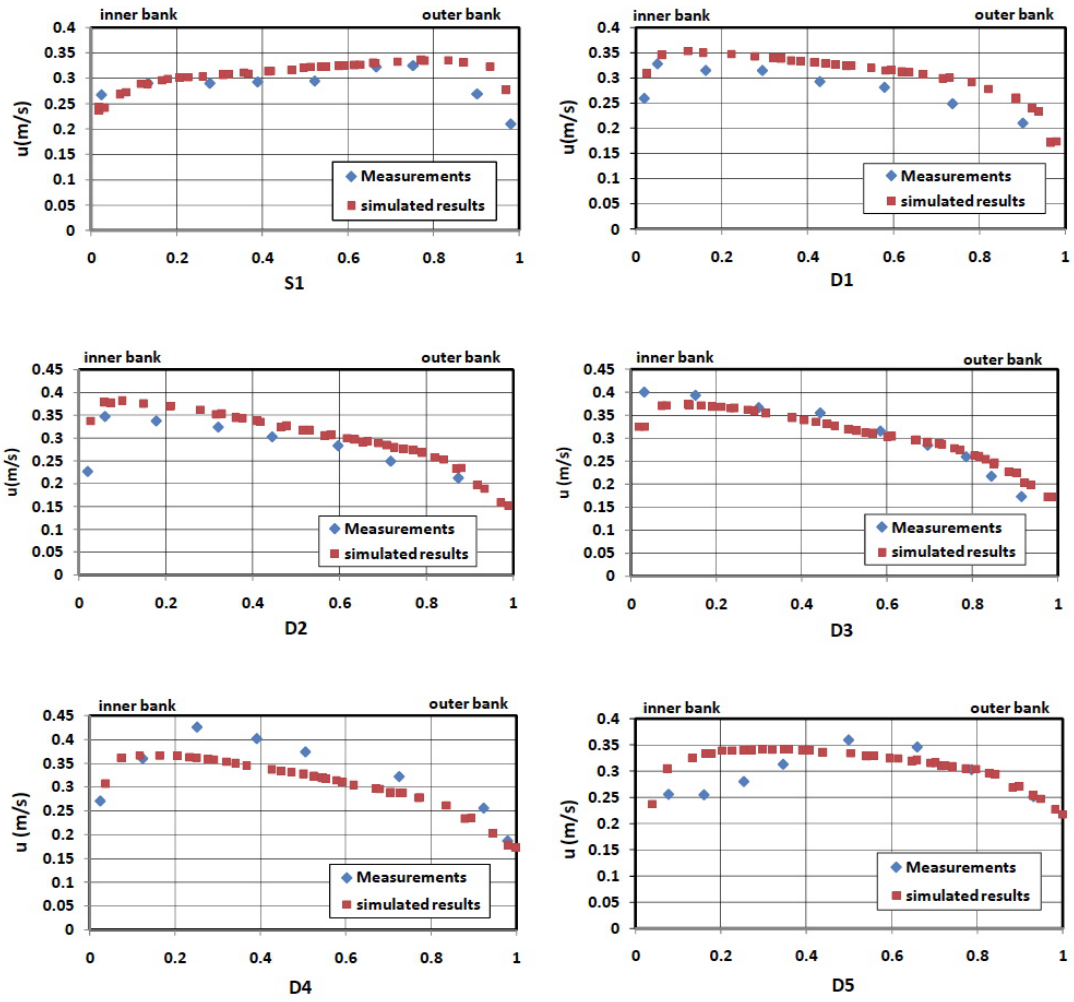

Figure 2.7: Comparison between depth-averaged calculated and measured velocities at different sections.

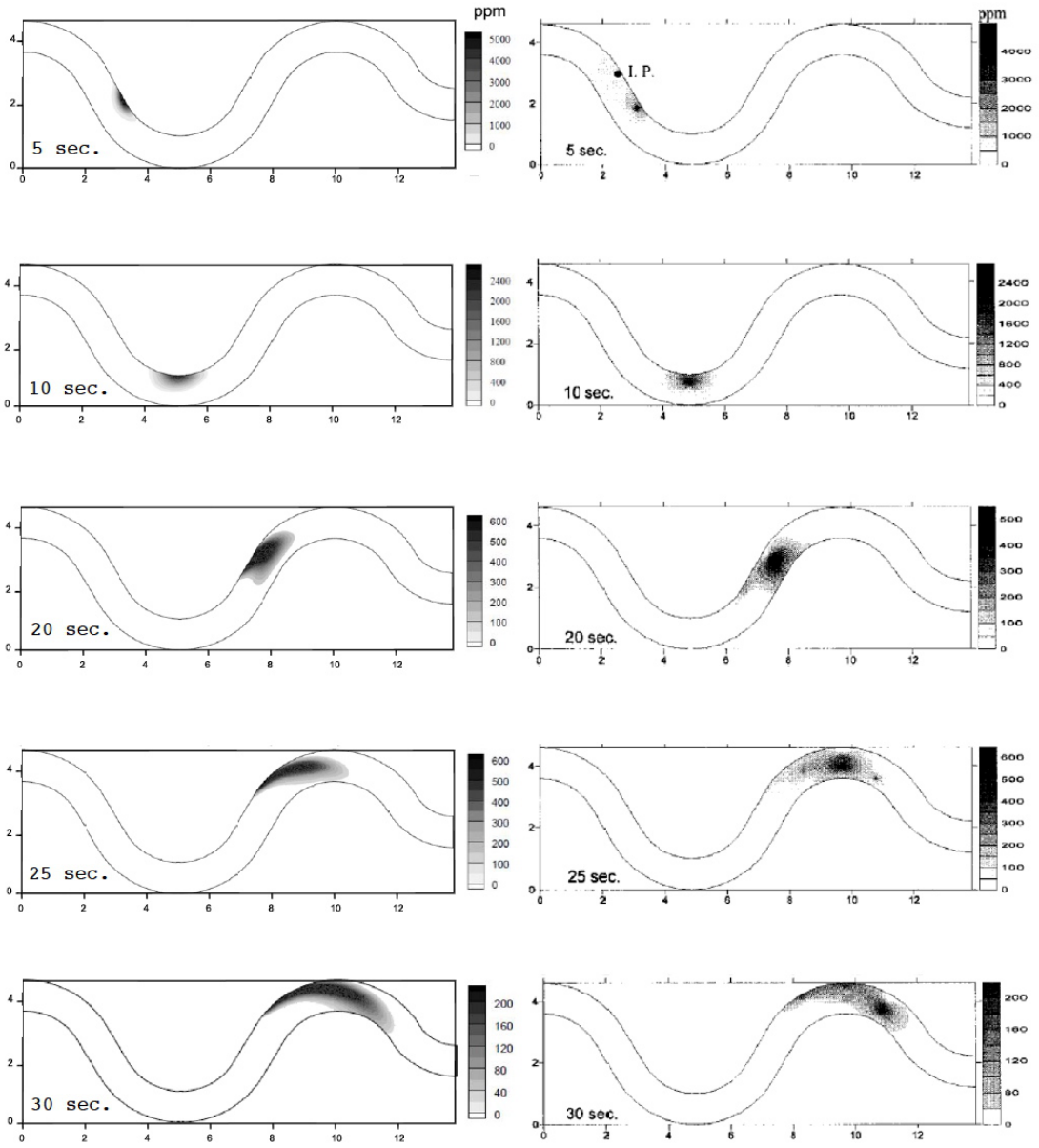

Figure 2.8: Behavior of concentration cloud; (left) simulated results and (right) measured results.

3

Case Study: Re-originate Burullus Coastal Lake's Ecosystem Using Salinity Dynamics as a Management Tool

This chapter is representing a numerical study for El-Burullus lagoon brackish water as a model example for the other Egyptian coastal lakes on the Mediterranean Sea. This lake ecosystem has deteriorated since Aswan High Dam Construction, 1965. It is suffering from many problems, which might lead to environmental degradation and substantial changes in its ecosystem. Lake salinity has suffered from significant decrease due to excess unregulated drainage water effluent into the lake, which affected the lake flora and fauna. The purpose of the current study is to restore the salinity conditions of Burullus Lake to those before the construction of Aswan High Dam. For this purpose, the validated depth-averaged mass transport model is used to simulate salinity distribution under actions of bathymetry, tidal current, wind, precipitation, evaporation and drainage discharges for El-Burullus shallow coastal lake. After model verification, five scenarios were studied for further understanding of the lake circulation and salinity dynamics to investigate possible means of restoring them to the desired state as before Aswan High Dam Construction.

3.1 The Study Area

Burullus lagoon brackish water (31^o 22' - 31^o 26' N and 30^o 33' - 31^o 07' E), on the northern Egyptian coast, Figure 3.1, is one of the most important Egyptian northern lakes from an economical point of view. It is located on the delta between Rosetta and Damietta branches of the Nile. Water depth is ranged between 0.50m and 2.00m and separated from the Mediterranean Sea by sand dunes to the north and fish farms along its southern margin. The lagoon intercepts great amounts of agricultural effluents before they are discharged to the eastern Mediterranean Sea through a small breachway. It is suffering from many problems, which might lead to environmental degradation and substantial changes in its ecosystem. Several studies have been carried out on the different aspects of the lake ecology (7, 8), which showed that the water quality of the lake has changed over time. These changes are related to human intervention (26, 27).

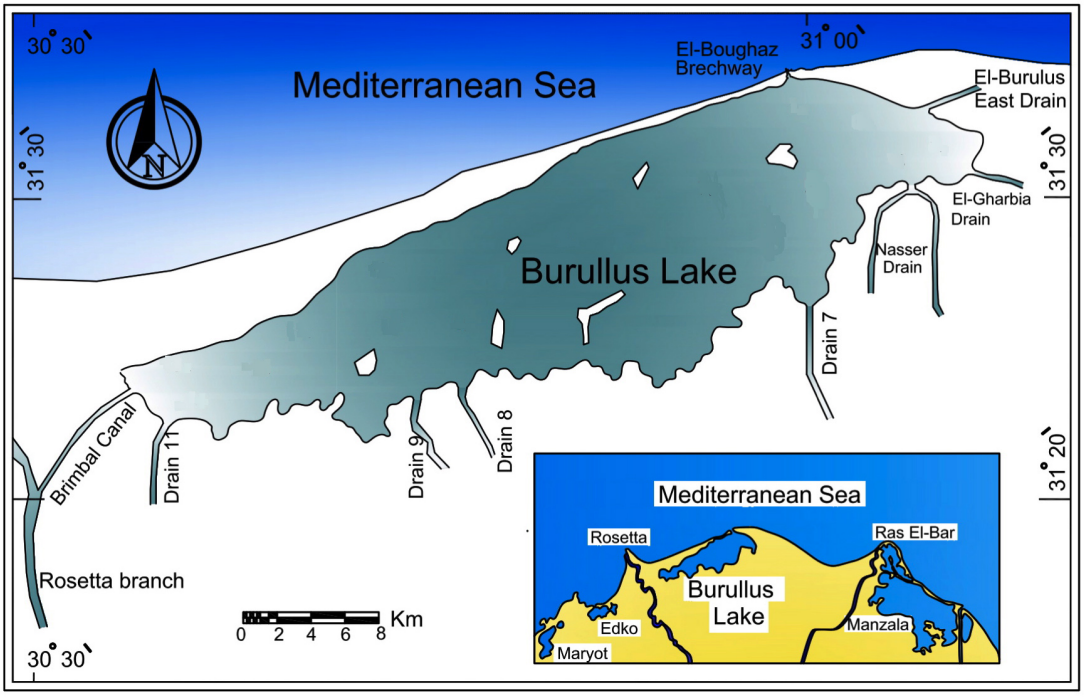

Figure 3.1: Layout of Burullus Lake presenting different connected drains.

Figure 3.2 introduces a chain process that led to severe environmental degradation of Burullus Lake. Once the drainage discharge increased after constructing Aswan High Dam, the lake desalination started which was the major factor affecting vegetation prevalence in the lake. Vegetative colonies offered a suitable environment for sediment trapping which led to decrease the lake size and reduced the lake residence time. Again, the lake size reduction while the lake is intercepting great drainage water, which led to the lake desalination. Since the sea water couldnt intrude the lake due the lake water level rise. This process led to change the composition of the aquatic fauna, which lead to Socio-economic consequences as a result of changes in commercial fish availability from highly prized marine species to the much cheaper tilapia. These problems are explored in details in the following subsections.

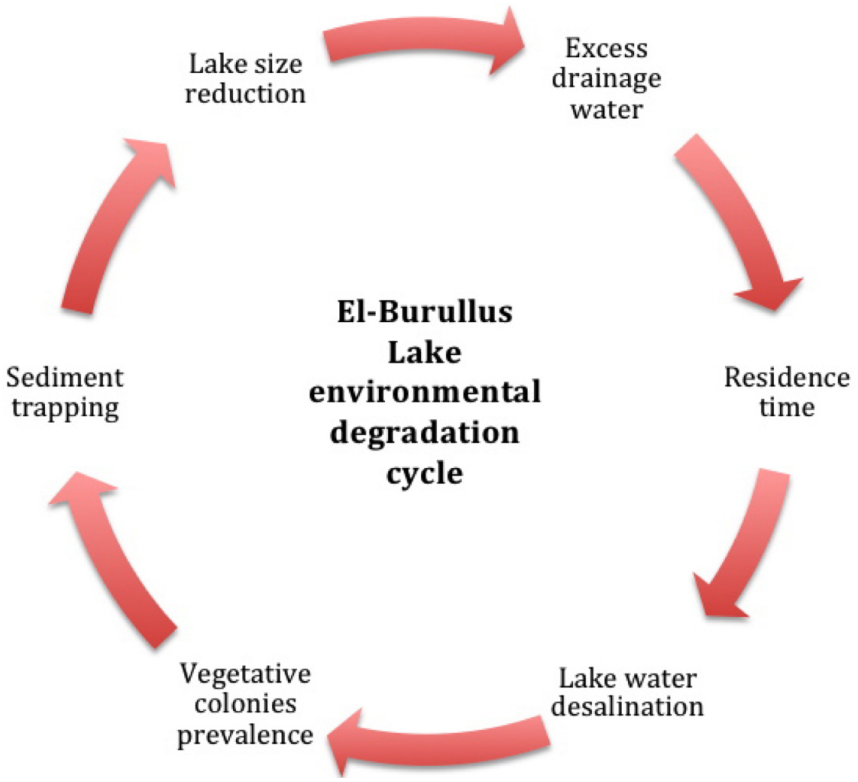

Figure 3.2: Burullus Lake environmental degradation cycle.

3.1.1 Desalinization

Burullus wetland is one of the disposal areas for agricultural drainage water in Egypt. It receives most of drainage water of the Nile Delta region through the drainage system. Figure 3.3 shows that the lake agricultural catchment area is covering about 68% of the middle Nile Delta region. Recently, the marine ecosystem in the lake has deteriorated due to discharges of excessive agricultural drainage water into the lake. Most of the drainage zones end with pumping stations which lift the drainage water into Burullus Lake as the case with drains 7, 8, 9, and 11. Few drainage zones discharge their water into the lake freely as the case of Brimbal canal.

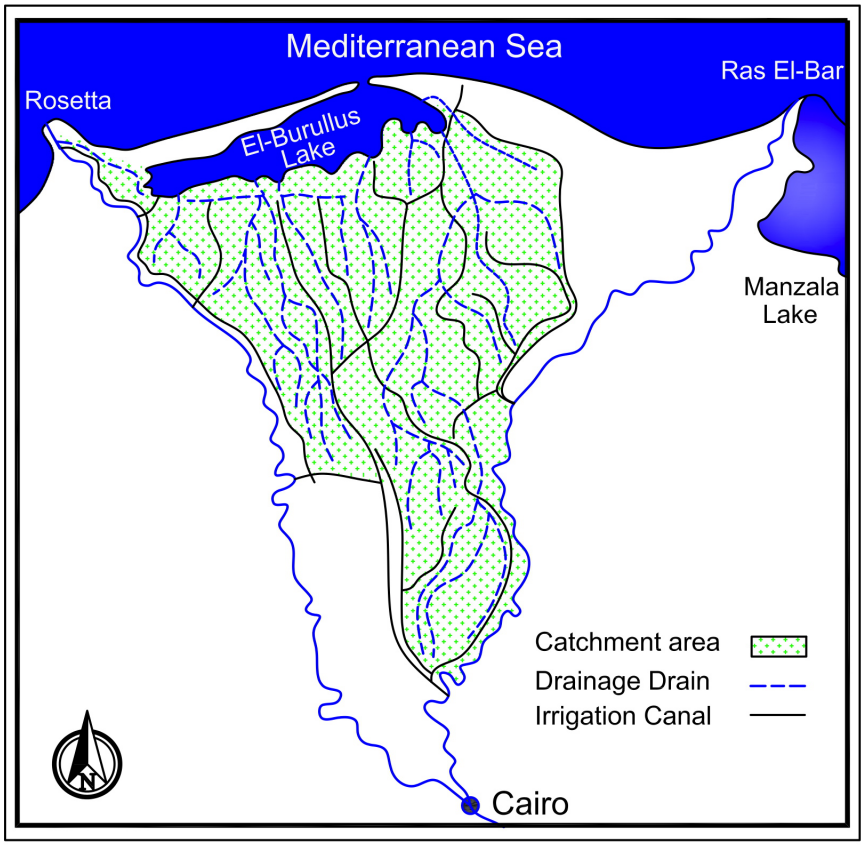

Figure 3.3: Burullus Lake catchment area.

Following the completion of the Aswan High Dam on the Nile River in 1965, Egypt's fresh water resources became fully regulated and the intensity of agricultural irrigation and synthetic fertilizer consumption increased, leading to a rise in the amounts of

agricultural drainage received by the lagoon. The total amount drained was about 2.3-2.7 billion cubic meters, which increased in 1970 to about 3.2 billion cubic meters, and in 2001 and later, a higher value of about 4.0 billion cubic meters was reached (27). These factors, combined with increases in upstream pollution have significant and often dramatic ecological effects. Salinity as an ecological indicator has decreased over time while nutrient concentrations, including organic and inorganic nitrogen, have increased. Salinity values are significantly high for various areas during 1973 compared with 2002 as shown in Figure 3.4. Even the minimum salinity values in 1973 is higher than the maximum values in 2002 (9, 10).

3.1.2 Fish productivity

One evidence on the environmental conditions degradation is the distribution of the aquatic fauna in the lake that originally consists of fresh and marine water fish. Table 3.1 gives the percentage weight records of the fish species catch in the experimental fishing at El-Burullus Lake in 1973 and 2002. It is clearly shows that the marine fish species decreased in the experimental catch from 15.99% in 1973 to 1.81% during 2002. On the other hand, the percentage of freshwater fish catch increased from 81.72% in 1973 to 98.18% during 2002 (9). The absence of favorable environmental conditions and the decreased values of salinity are the main factors affecting presence of aquatic fauna in the lake. In addition, escaping marine fish to the sea affects the socio-economic conditions of the local inhabitants. Since marine fish is more delicious and more expensive than freshwater fish.

3.1.3 Vegetative colonies prevalence

Prevalence of common reeds (phragmites australis) inside the lake is also considered significant evidence on the environmental conditions degradation. These vegetative areas compose vegetative colonies that obstacle navigation inside the lake, Figure 3.5. Moisture, salinity and sedimentation were the main factors that governed the plant succession in Burullus Lake with the decrease in salinity being the main factor that lead to the formation of these communities (28). Phragmites marshes offer poor-quality habitats for larval and juvenile fish (29), whose mobility is reduced by progressive clogging of shallow-water areas following litter and sediment accumulation (30, 31).

3. CASE STUDY: RE-ORIGINATE BURULLUS COASTAL LAKE'S ECOSYSTEM USING SALINITY DYNAMICS AS A MANAGEMENT TOOL

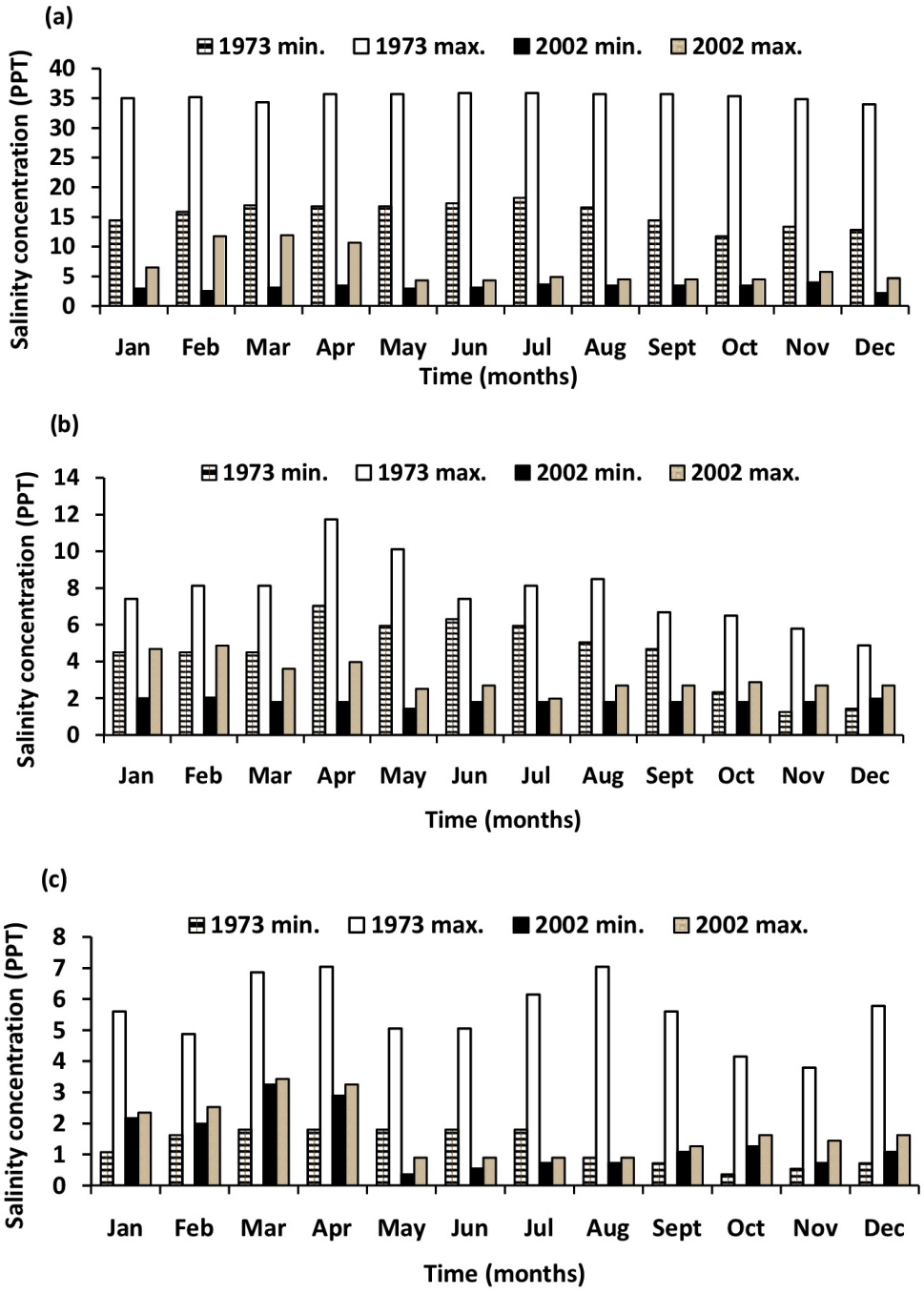

Figure 3.4: The minimum and maximum values of water salinity at various areas of Burullus Lake recorded in 1973 and 2002; (a)eastern area, (b)middle area, and (c)western area.

Table 3.1: Percentage weight of marine and freshwater fish species in experimental fishing at El-Burullus Lake 1973 and 2002.

Fish species	1973	2003
Tilapia	68.06	93.87
Clariaus lazara	11.58	3.42
Bagrus bayad	2.08	0.90
Total fresh water	81.72	98.18
Liza ramada	8.76	1.81
Mprpome lanrax	1.54	-
Morone puncata	3.61	-
Mugil cephalus	1.54	-
Angulia Sp.	0.54	-
Total marine fish	15.99	1.81

Hellings and Gallagher (32) conducted many experiments and concluded that reeds height, density and biomass is negatively affected by increasing salinity. Moreover, cutting reeds and flooding with brackish water (salinity 10 ppt) is able to prohibit further growth for 18 months.

Figure 3.5: A plate shows the vegetative colonies propagation in the lake.

3.1.4 Water quality

Lake Burullus was declared a nature reserve under Law 102/1983 in May 1998. The lake and its surroundings are subjected to excessive use: land reclamation, fish farming, over-fishing, over-hunting, overwhelming flow for drainage water, etc. Despite being the least polluted of the northern delta lakes, increasing quantities of agricultural drainage water carrying heavy fertilizer and pesticide loads contribute significantly to the eutrophication and pollution of the lake (33, 34).

Okbah and Hussein (33) studied the physical and chemical properties of the lake. They declared that the decreased amount of pure fresh water and sea water invasion to the lake through El-Boughaz opening affected directly and/or indirectly the water quality of the lake, causing eutrophication state, such as increasing amount of dissolved inorganic nitrogen, phosphate and silicate concentrations. These causes higher phytoplankton count, diversity index and chlorophyll-a content. Such situation provides a warning alarm against the increased pollution in the lake. They are recommended to control discharge of drainage and sewage water into the lake or at least minimize the usage of fertilizers in agricultural lands and treatment of drainage water is essential to hurry its recovery and improving water quality.

Other investigators examined the lake ecological and biological status to determine its water quality and eutrophication status (35, 36, 37). They concluded that the lake suffers from excessive nutrient concentrations. The evaluation of the Lake trophy state shows that the lake water body varies between oligotrophic to mesotrophic. These levels sustain the lake in good to fair trophic conditions. Chlorophyll a showed wide variations over the sampling period with maximum levels in the western area in response to the nutrient-rich water inputs from the surrounding farmlands. Nutrients were at maximum levels in the southern and western parts of the lake, which were affected by wastewater discharged into the lake through the drains system. The eastern zone is the least trophic area because it is subjected to water exchange between the lake and the sea through the inlet at the northern part. They also recommended the lake environmental restoration through drastic reduction of the external Nitrogen and phosphorus loads by regulating effluents from fish farms, domestic and industrial sources.

3.2 Salinity Distribution in El-Burullus Lake

Salinity distribution inside the lake has been simulated during 2001 taking into account; bathymetry, hourly tidal current, hourly wind action, average monthly precipitation, average monthly evaporation and average monthly drain discharges.

3.2.1 Data overview

Water salinity distribution measurements from Al-Sayes (9) for 15 measuring stations during 2000-2003, Figure 3.7, plus those taken from the Coastal Research Institute, National Water Research Center, were used to verify the numerical predictions. Measured salinity values show that the salinity gradient in the vertical direction is not dominant which means that stratification is weak and accordingly assuming vertical homogeneous salinity could be valid. The used data consists of bathymetry, meteorological, effluent flux, and salinity concentrations as follows.

3.2.1.1 Lake geomorphology and bathymetry

The shoreline of Lake Burullus takes several forms related basically to its formation, origin and evolution. It has an oblong shape extends for a distance of 47 km along NE-SW axis. The width of the lake from north to south varies from site to the other. The western sector has the least width which does not exceed 5 km, and then it increases in the middle sector to reach an average of 11 km. As the area of the lake changed over time, it is obvious that the lake size had decreased from 502.7 km^2 in 1984 to 410 km^2 in 1997 (i.e. 18.4% reduction), the maximum length from 56 to 47 km (16.1% reduction) and the maximum width from 15 to 14 km (6.7% reduction) as shown in Figure 3.6. The rate of these changes was assessed using the GIS and remote sensing techniques (38). The main basin of Lake Burullus is classified into three sectors: eastern, middle and western, each one has some sort of homogeneity in the geomorphological, hydrological and biological characteristics. The islets scattered in the lake form physical isolations between these sectors. Figure 3.7 shows the bathymetric map of Burullus Lake abstracted from El-Bayomi (39) and data supplied by Coastal Research Institute. Lake depth varies between 40 cm near the shores and 200 cm near the sea outlet (El-Boughaz opening). The remote sensing studies indicated that the deepest parts were in the middle sector of the lake where the depth reached 200 cm.

The area between the shore line and 75 cm depth approximates 58% of the total area of the lake (236.6 km^2 out of 410 km^2). Thus it seems that the lake lives its senility stage particularly with the continuation of drying and silting up processes which lead to the increase of shallow areas; the areas deeper than 130 cm have already decreased to about 20.6 km^2 (5% of the lake size). The outlet that connects the Mediterranean Sea with Lake Burullus is called Boughaz El-Burullus. From the original viewpoint, it is a natural water course. Its width at the narrowest point is about 80 m, and the water depth varies between 50 cm and more than 250 cm.

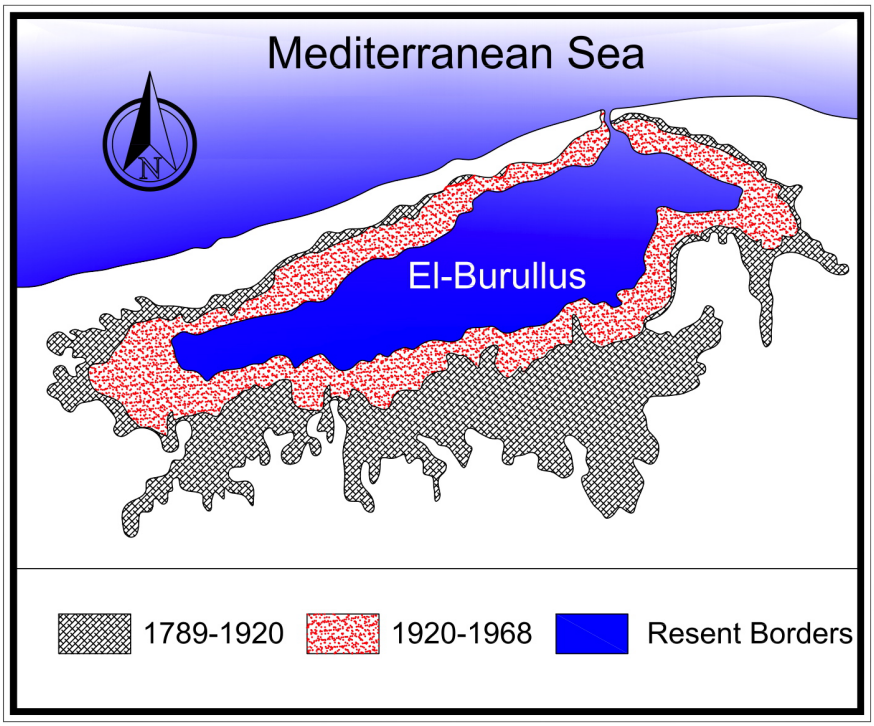

Figure 3.6: Size changes of Lake Burullus (1789 to 1997)

3.2.1.2 Drainage water

Burullus wetland is one of the disposal areas for agricultural drainage water in Egypt. It receives most of drainage water of the Nile Delta region through the drainage system. Figure 3.8 and Figure 3.9 show the monthly average drainage rate over the catchment area and its salinity concentration, respectively. The drainage system provides the lake with about four billion m^3/year of agricultural drainage water. The maximum rate of

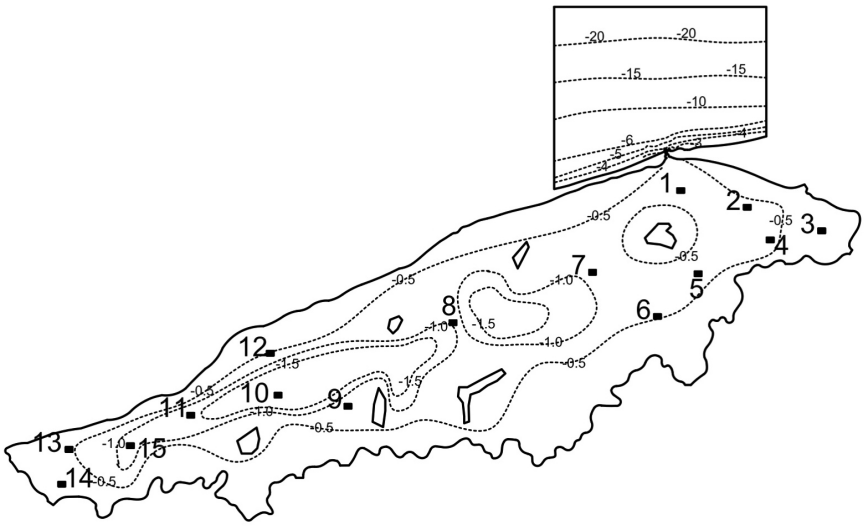

Figure 3.7: Bathymetric map of Burullus lagoon showing the field measuring stations during 2000-2003.

water discharged to the lake is during rice cultivation season (July - September), while the minimum rate is in January and February (winter closure). Drain 9 discharges the maximum amount (about 20 % of the total volume), while Burullus drain discharges the minimum (about 1.7 % of the total volume). Drainage water is not totally fresh but has some amount of salinity; approximately 4 ppt.

3.2.1.3 Rainfall

The mean annual rainfall over the area is 187.4 mm. This depth of water provides the lake with a mean annual volume of about 77.4 million m^3. Most rainfall takes place during the winter season (October - March), with no rainfall during summer months. The maximum depth of rainfall is received in December and January, as shown in Figure 3.10. The direct precipitation is not significant as inflow from drains.

3.2.1.4 Evaporation

The mean annual evaporation is 1583.3 mm. This value approximates about 646.5 million m^3 of water loss from Lake Burullus. Maximum evaporation takes place during May - September, while the minimum during December - February, Figure 3.10.

3. CASE STUDY: RE-ORIGINATE BURULLUS COASTAL LAKE'S ECOSYSTEM USING SALINITY DYNAMICS AS A MANAGEMENT TOOL

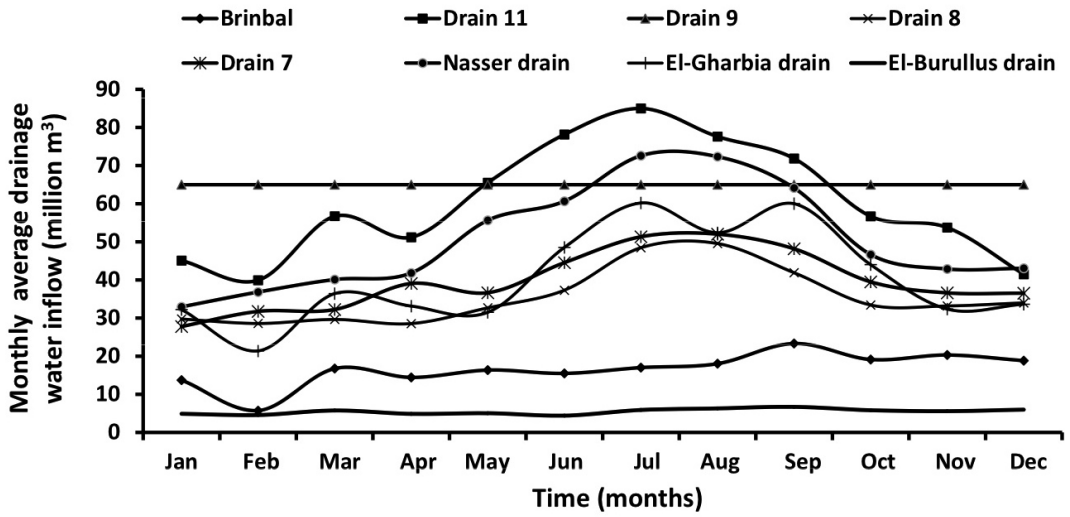

Figure 3.8: Average monthly drainage water inflow to Burullus Lake from various drains.

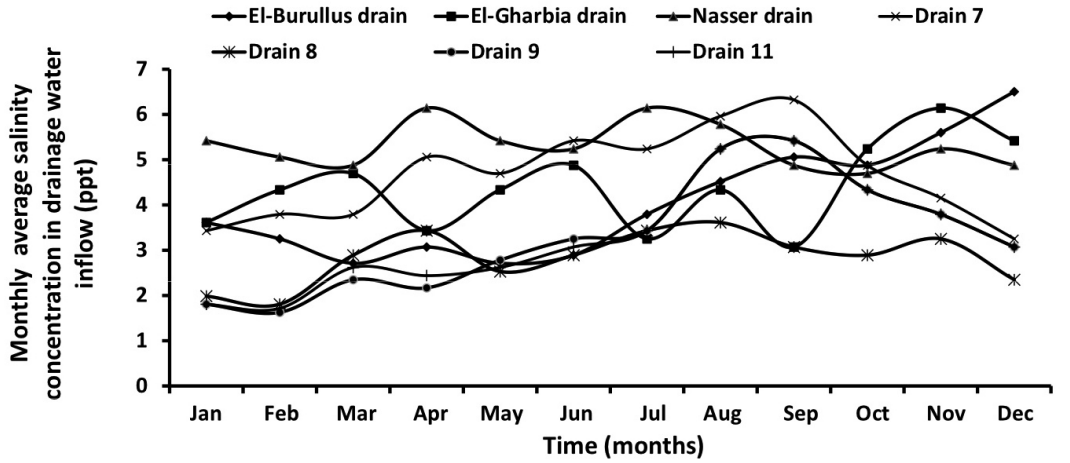

Figure 3.9: Average monthly salinity concentration values in drainage water inflow to Burullus Lake through various drains.

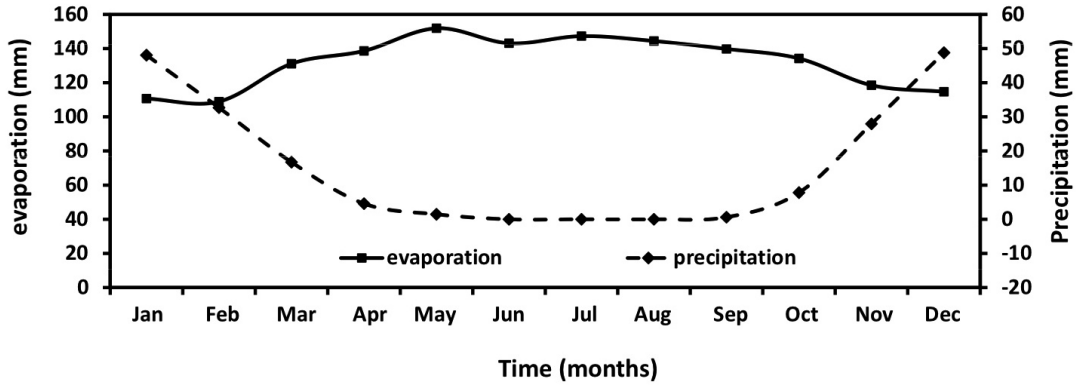

Figure 3.10: Average monthly precipitation and evaporation at Burullus Lake area.

3.2.1.5 Sea water level

Fanos (40) and El-Shinawy (41) estimated the tide at Burullus headland as the difference between the mean high water level of 33 cm and the mean low water level of 18 cm. Although, they concluded that the tide range is small and hence the tidal effect could be negligible, sea water level is an important boundary for the lake which, directly affects the salinity and the water amount getting in or out of the lake. As a result, direct sea water level measurements shown in Figure 3.11 were used as boundary condition which is considered the main source of salinity for the lake.

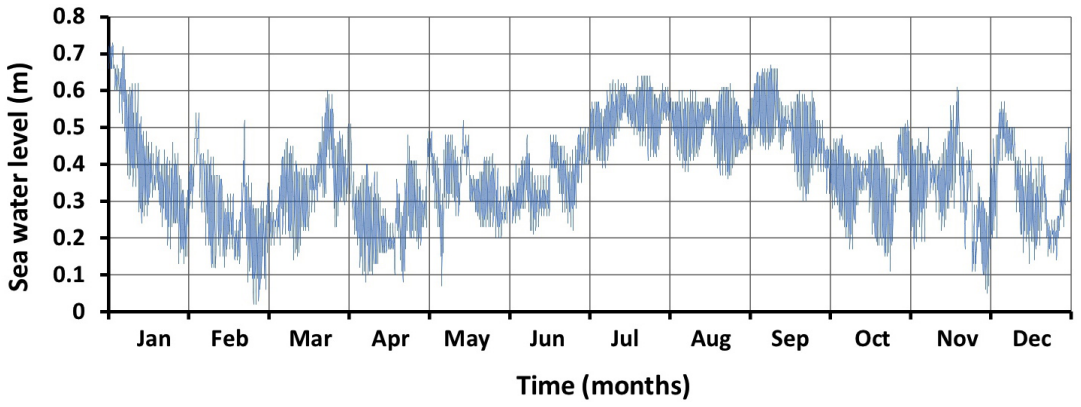

Figure 3.11: Sea water level at Burullus outlet during 2001.

3.2.1.6 Wind

Wind is one of the driving forces for shallow water especially in coastal areas. The hourly measured wind speed and direction is used in this simulation. Figure 3.12 presents wind rose for the lake area during 2001 which demonstrate that the north-west is the most prevailing wind direction and the mean annual wind speed is 3.4 m/sec.

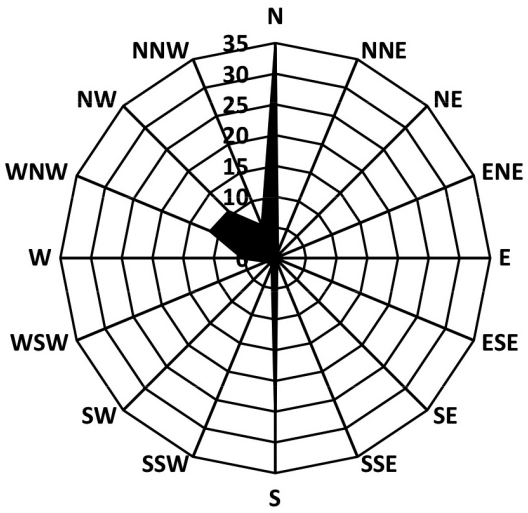

Figure 3.12: Wind rose plot for Burullus Lake area.

3.2.2 Model setup and results

The computational method was parallelized in a distributed-memory system with a domain decomposition method. The domain decomposition of the generated unstructured cells was subdivided into 32 sub-domains to shorten the simulation time while fine unstructured mesh with total 36677 elements was generated to represent the lake basin, Figure 3.13. The computations were performed with XE6 open super computer, Kyoto University. The total computational time required to run simulations is approximately 155 minutes using time step of 6.0 seconds. For simplicity, we set the lake initial salinity on the measured data of autumn 2000 to describe the horizontal salinity gradient in the lake. The hydrodynamic model is driven by the potential flows emanating from the major drains feeding the lake, the surface wind shear across the lake, and the monthly

evaporation and precipitation rates. The direct measurements for sea water level were used for the sea open boundary.

Predicted results and measured data show that El-Burullus Lake water is considered as fresh water in the most western parts and tends to be brackish in other areas, while the saline water is limited in a narrow area at El-Boughaz area due the direct connection with Mediterranean Sea. The predicted model lake salinity distribution was validated against the measured data during 2001. As shown in Figure 3.14, good agreement was obtained between measured and calculated spatial salinity distribution for different seasons. Salinity concentration discrepancies may be caused by the used monthly averaged data especially the drains fluxes or stratification due to density variation. Water level in the lake has a great influence on the salinity distribution. However, low water level permits sea water to enter the lake. On the other hand, high water level in the lake during most of the year months leads to flow towards Mediterranean Sea.

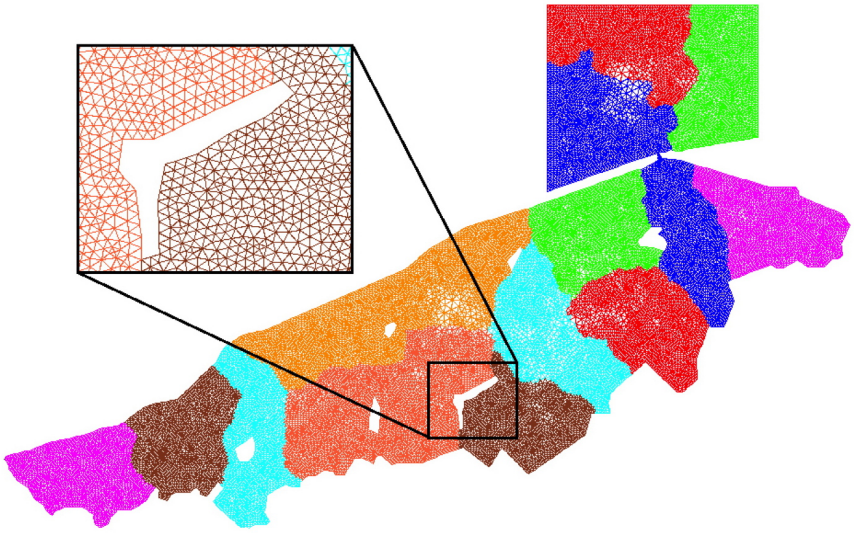

Figure 3.13: Computational domain of unstructured grid divided into sub-domains and close up for the mesh around island.

3.3 Management Scenarios

Scenarios are very useful for environmental management since they illustrate possible situations that might develop in the future based on knowledge of the possible conse-

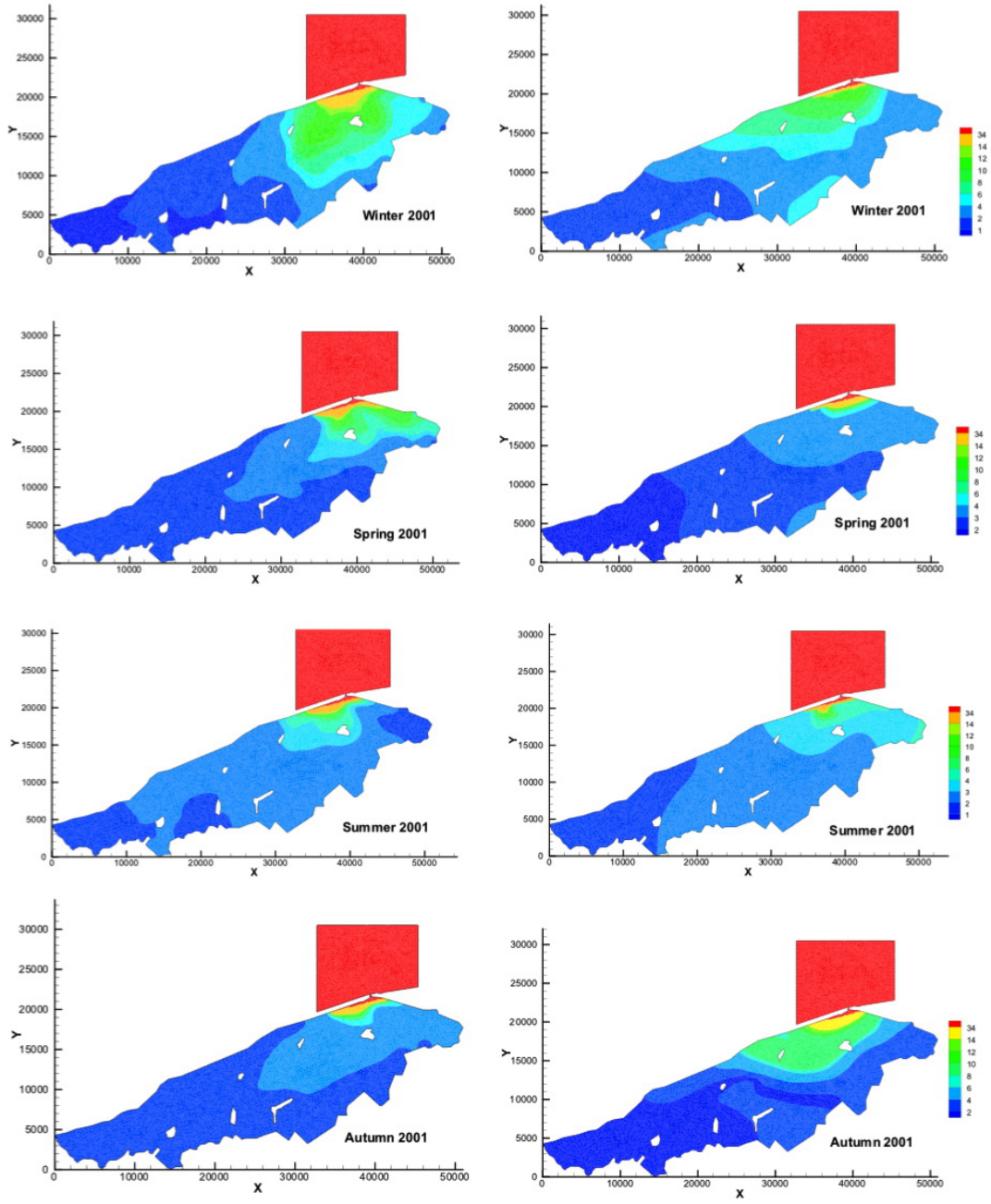

Figure 3.14: Spatial salinity distribution in the lake in ppt; (left) calculated, and (right) measured.

quences of human activity. Though, monitoring measurements are needed to mitigate the adverse effects or to extend positive results. Five scenarios were studied to understand salinity dynamics, circulation and flow driving forces, with the assumption that no change in meteorological conditions. These scenarios are based on changing the interaction between drainage water and sea water in order to get the best salinity dynamics for proper environmental ecosystem of the lake aquatic fauna and flora.

3.3.1 Benchmark (Pre-Aswan High Dam Construction)

This is the first scenario to be simulated and it represents the original situation, which assumes the flood routing before constructing Aswan High Dam. This control run shows the target pattern of salinity spatial and temporal distribution. This scenario is important as a point of reference against the suggested scenarios with changed conditions. This scenario simulates the Nile River flooding to the lake. Water flow of almost 100 million m^3 is flooded into the lake throughout the year. During flood season, water flow is increased to about 700 million m^3 in September, Figure 3.15, with a total annual flow of 2.5 billion m^3.

3.3.2 Current status

The second scenario presents the usual case of the irrigation system during 2001. This scenario was used for model verification. The major drains feed the lake with a monthly flux that ranges from 250 million m^3 to 400 million m^3 with total annual amount of 4.0 billion m^3, Figure 3.15. This scenario gives a clear picture to the current status salinity pattern. Also, this scenario compared with the benchmark scenario represents how significantly are salinity dynamics in Burullus Lake affected nowadays.

3.3.3 Drainage water flows elimination (No-flux)

The third scenario reflects the importance of the drainage flux into the lagoon. Thus, all discharges into the lake are stopped and only wind, tidal and meteorological parameters are considered.

3.3.4 Add new inlet

This scenario is a suggestion to construct a new breach-way to increase the direct sea water exchange between Mediterranean Sea and Burullus Lake. The proposed new

inlet has the same dimensions as the old one and exists in the middle part of the lake. Using this scenario, salinity inside the lake is expected to increase without changing drainage water amounts into the lake.

3.3.5 Change effluent routing

This scenario represents a proposed routing flow to Burullus Lake in order to re-originate the lake conditions without artificial constructions. Change effluent routing depends on the winter closure season, which is closing delivery canals for a month or two months during winter season to permit maintenance and construction of irrigation structures. Through this scenario, two alternatives were studied; (a) stopping drainage water into lake during January, and (b) stopping drainage water during January to March (New routing). Trapped water is then released uniformly during July to December to produce artificial flood routing, as shown in Figure 3.15.

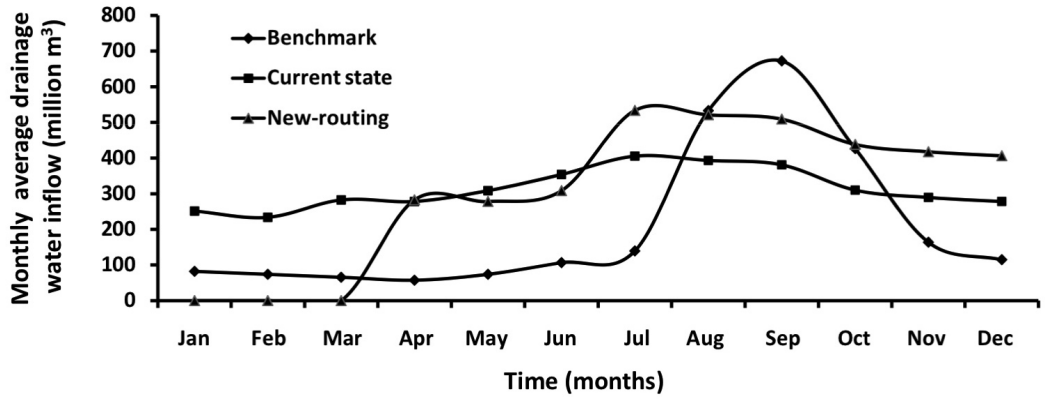

Figure 3.15: Total flow routing to the lake.

3.4 Results and Discussions

The predicted results for various scenarios are shown in Figure 3.16, Figure 3.17 and Table 3.2. Figure 3.16 plots the salinity values over time for eastern, middle, and western areas. Eastern, middle, and western areas are represented with station 1, station 8 and station 11, respectively. Figure 3.17 shows the lagoon water level for different scenarios abstracted form station 8 compared with sea water level. Table 3.2

gives a summary of average salinity values for different scenarios for eastern, middle, and western areas.

Table 3.2: Summary of average salinity values for different case studies.

Scenario	Benchmark	Current status	No-flux	New-inlet	New-routing
Eastern Area	20.96	5.88	36.01	9.39	13.46
Middle Area	7.91	2.44	38.14	5.05	8.31
Western Area	3.29	1.50	38.90	1.96	4.17

The benchmark scenario reveals an obvious time pattern for salinity dynamics inside the lake. It shows that salinity values go up during May to July resulting in a sea water environment in the lake. Salinity values then decreases significantly when fresh water floods to the lake during September to December accompanied with a rise in lake water level. This scenario expresses the original status which allows marine fish to enter the lake with sea water invasion and return back to the sea during the flood season. For the lake current status scenario, it is clear that lake water level is almost higher than sea water level except for a few days during the year. As a result sea water cannot encroach inside the lake and low salinity brackish water environment becomes the most dominant in the lake over time. This environment is unfavorable for marine fish while suitable for aquatic flora (i.e. common reeds) which obstacle navigation inside the lake. Another descriptive scenario with no drainage water flow to the lake is introduced to show the importance of fresh water flux into the lake. Without this flux, the lake will be hyper saline, Figure 3.16. The salinity significantly increases since the lake water level is always lower than sea water level. This scenario emphasizes the importance of effluent flow to the lake for salinity control and also for water flow circulation.

Other scenarios were considered to enhance the lake environmental conditions either by constructing a new breach-way or changing the drainage water flow routing to the lake. Adding a new breach-way to increase water exchange between sea and lake is considered. Improvement in salinity values are obtained but not similar to those of the benchmark scenario, Table 3.2. The lake remains a brackish water environment and accordingly a better solution is needed. In case of the first alternative for the last scenario, drainage water flow is stopped during January. Simulation results reveal

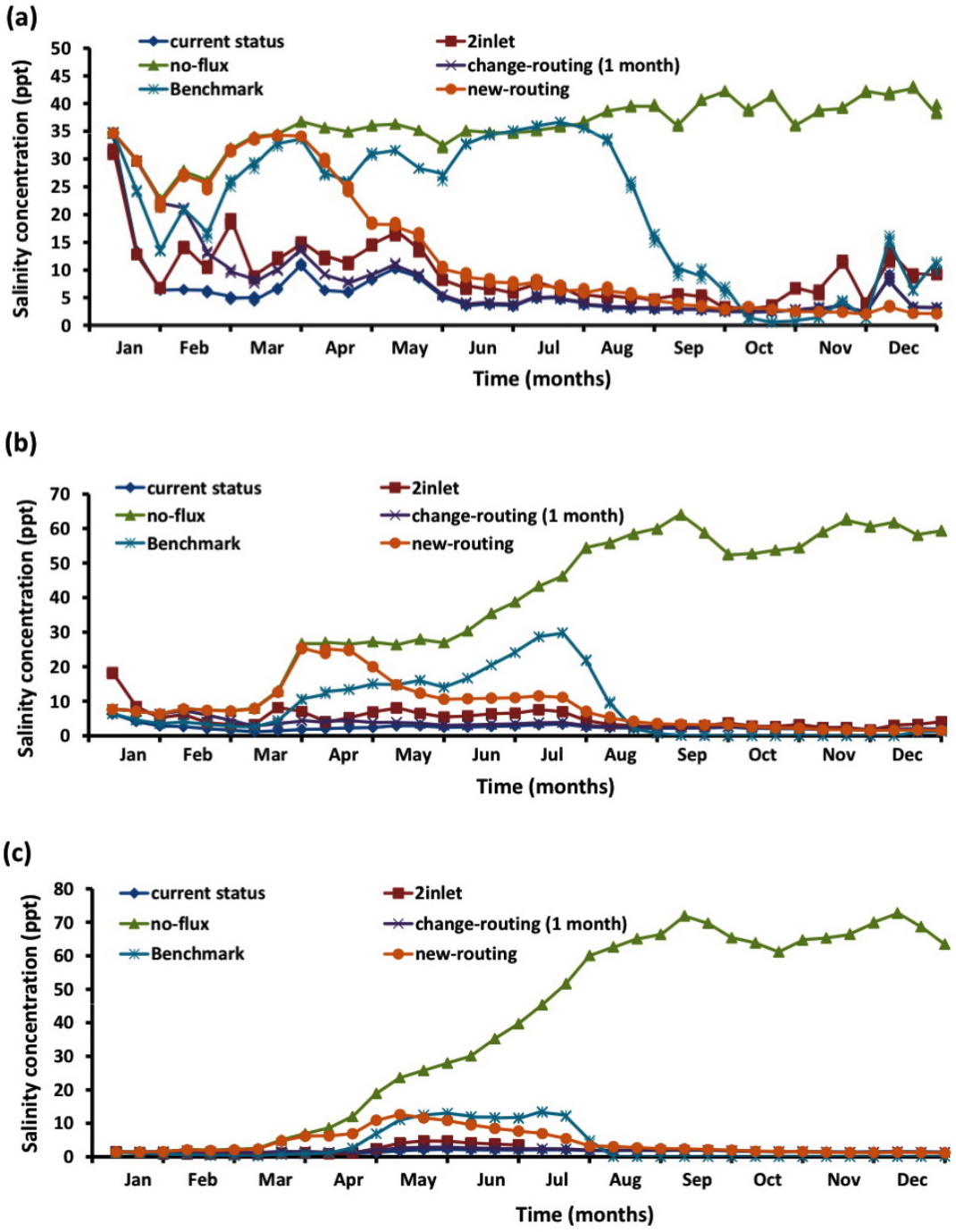

Figure 3.16: Water salinity concentration in the lake results from different scenarios for various areas; (a) eastern area, (b) middle area, and (c) western area.

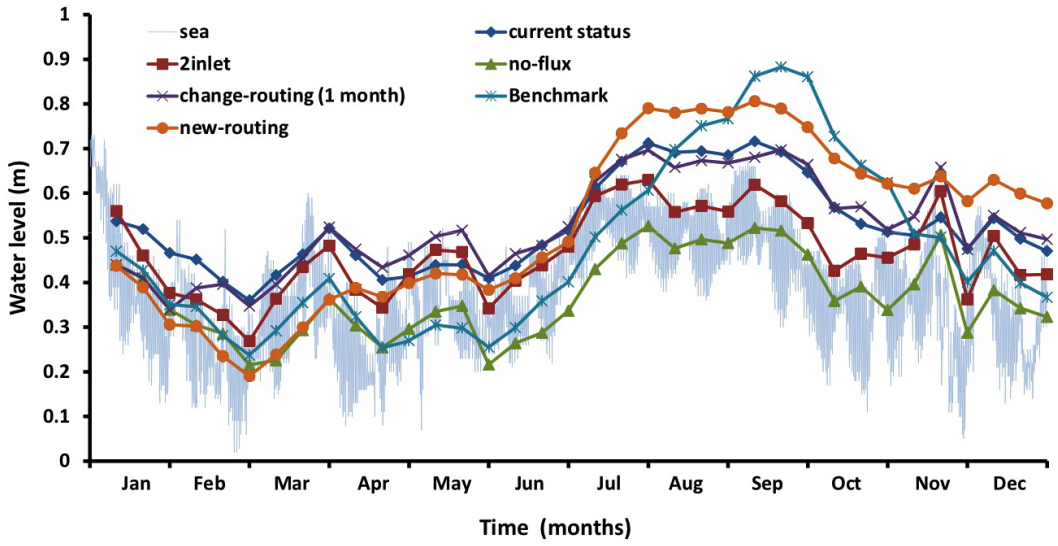

Figure 3.17: Burullus Lake water level during applying different scenarios.

that this period is not enough to increase salinity as expected in all areas, which leads to the second alternative where this period is extended from January to March. The main purpose is to allow sea water to invade the lake. It is found that the sea water environment prevails the lake during March and starts to return back to the sea after starting drainage water flushing through the artificial flood prepared by the new routing, Figure 3.15. The salinity propagation due to the new routing is similar to that produced by the benchmark scenario at different areas.

Figure 3.18 compares the water circulation inside the lake during March for different scenarios. Streamtraces point sources at the lake breach-way are used to visualize water streamlines. This figure clearly shows that the lake nowadays is considered as a collecting zone for drainage water and then gets out of to the sea. On the other hand, it also presents water flows to the lake in case of pre-Aswan High Dam scenario with monthly flux from Brinbal canal of about 100 million m^3 allowing sea water to invade the lake. Using the new routing, the reduced winter flow results in less resistance to sea water intrusion and can significantly increase salinity in the lake. Moreover, the new artificial flood routing can expel saltwater out of the lake by October. The salinity propagation due to the new routing is relatively good since salinity values can be increased inside the lake, see Figure 3.16 and Table 3.2. Using the new routing, salinity

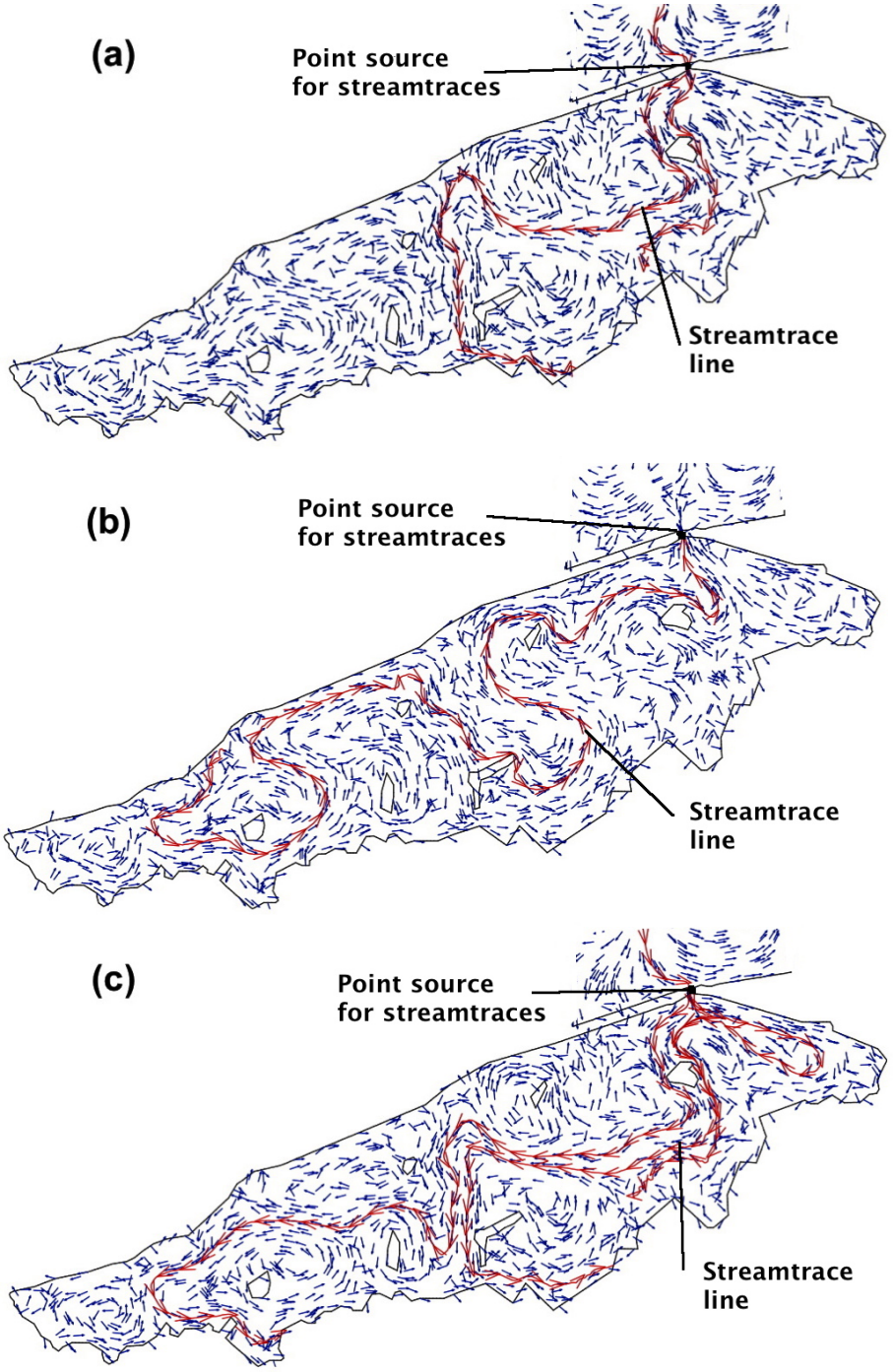

Figure 3.18: Depth-averaged velocity field and water circulation inside the lake in March; (a) pre-Aswan High Dam, (b) current status, and (c) after using the new-routing.

dynamics may be restored to be the same those in pre-constructing Aswan High Dam case. As a result, marine fish can enter the lake most of the year and socio-economic status of fishermen will be improved. In addition, sea water which is almost free of pollution and gives relative movement to the lake water will improve the aeration in the lake. Also, common reeds distribution at the southern and eastern area will be demolished providing much navigation space in the lake.

As with any environmental system, it is important to evaluate progress by objectively measuring key indicators. A well-designed monitoring system is urgently needed to provide important information about changes to the environmental system including lake, surrounding soil and groundwater conditions, e.g. water table depth and salinity that will affect surrounding vegetation areas. This will help decision makers and responders to develop actions, define local trends and risks, fine tune the actual plans or place other management options.

3.5 Summary

A 2D-depth averaged transport model based on MACS algorithm for shallow water equations coupled with mass transport equation has been applied to Burullus shallow coastal lake, Egypt. Salinity distribution inside the lake has been reasonably simulated considering the effect of bathymetry, tidal, wind, precipitation, evaporation and drainage discharges. It is verified that the model has a potential for simulation of long-term coastal process using parallel computation. The present study provides a basis from which decision makers and responders can develop actions and allocate resources to improve environmental conditions in Burullus Lake. Salinity dynamics have been simulated for various possible scenarios: before constructing Aswan high dam, current status, drainage discharge elimination, case of adding new breach-way, and changing drainage water routing, in order to adequately manage temporal salinity in Burullus lagoon. These scenarios revealed the importance of fresh drainage water discharges into the lake and the possibility to eliminate the effluent discharge during January to March which allow sea water to invade the lake and permit salinity exchange. The stored water can be used as an artificial flood similar to pre-Aswan High Dam construction flood, which unexpectedly increases the lake water level to become brackish water again. This circulation may lead to re-originate the lake and to improve its ecosystem.

4

Climate Change Impact On El-Burullus Lake Salinization Process

Scientific community has commonly argued on the global climate change. Rising global temperatures have been accompanied by changes in weather and climate. Many places have seen changes in rainfall, resulting in more floods, droughts, or intense rain, as well as more frequent and severe heat waves. Between the years 1961 and 1993, the global sea level rise increased with an average rate of 1.8 mm/year. Between the years 1993 and 2003, a higher rate was observed, averaging approximately 3.1 mm/year according to the United Nations Intergovernmental Panel on Climate Change (IPCC 2007). Sea level will rise between 18 and 59 cm by the end of the 21st century (42). This chapter presents a numerical study to investigate the impact of climate change on salinization process in El-Burullus lake. The purpose of the current study is to restore the salinity conditions of Burullus Lake to those before the construction of Aswan High Dam under climate change conditions. The model is used to predict the salinization and circulation processes occurring under the effect of two global emissions scenarios (SRES A2 and SRES B1) archived from the 2007 IPCC Fourth Assessment Report (AR4) which are abstracted from four different atmosphere-ocean coupled general circulation models (AOGCMs). In addition, two other reference cases were introduced to judge climate-induced salinization effect.

4.1 Overview to Climate Change

Egyptian researchers has commonly argued on the climate change impact on the coastal area, north Egypt, sea level rise in specific. Results from studies on various aspects of the impacts and possible responses to sea-level rise on the Egyptian coast (Milliman et al.(43), 1989; Stanley and Warne(44), 1993; El-Raey et al.(45), 1999; Frihy et al.(46), 2010; Frihy and El-Sayed(47), 2012) indicate that a sizable proportion of the northern part of the Nile delta will be lost due to a combination of inundation and erosion, with consequent loss of agricultural land and urban areas. Furthermore, agricultural land losses will occur as a result of soil salinization(48). Over the coming decades, the Nile Delta will face greater threat due to sea level rise and land subsidence as well. Regarding climate change and its impacts on soil characteristics, rapid increase in salinity values during the former three decades was found. This increase may be due to the intrusion of salty water of the Mediterranean Sea(49). Coastal wetland ecosystems of Egypt, such as salt marshes are particularly vulnerable to rising sea level because they are generally within a few centimeters above the sea level(42). El-Burullus lake's salinity is affected by various factors; temperature, precipitation, sea level rise, wind, and human intervention. These factors are subjected to be changed under climate change impact. In this study, we assume a constant wind and drainage flux from agricultural areas, and consider the predicted change in the other factors.

4.2 Climate Change Test Scenarios

Scenarios are very useful for environmental management since they illustrate possible situations that might develop in the future. To assess the effect of climate change, we used the World Climate Research Program's (WCRP's) Coupled Model Intercomparison project phase 3 (CMIP3) multi-data set archives where the AOGCMs outputs were obtained in the frame work of the IPCC AR4. The database of temperature and precipitation monthly values has been downloaded for each of the models listed in Table 4.1 for two scenarios (SRES A2, SRES B1) which are described in the IPCC AR4. A simple Fortran code was formulated to transform the database to the reference year 2100 based on the period 1971 to 2000. The same code was used to calculate the

Table 4.1: AOGCMs models used in this work

Model	Institution
CNRM-CM3	France, National center of meteorological Research
UKMO-HadCM3	UK, Hadly center for climate prediction and research
GFDL-CM2.0	U.S. Department of commerce, NOAA Geographysical fluid Dynamics Laboratory
MRI-CGCM2.3.2	Japan, Meteorological Research Institute

actual evaporation rate from temperature values using Thornthwaite method(50) as:

$$E_p = 0.553 D_o (10 T_i / J)^a \tag{4.1}$$

$$a = 0.675 \times 10^{-6} J^3 - 77.1 \times 10^{-6} J^2 + 0.01792 J + 0.049293 \tag{4.2}$$

$$J = \sum_{i=1}^{12} (T_i/5) \tag{4.3}$$

$$E_a = M E_p \tag{4.4}$$

where E_a is the actual evaporation rate; E_p is the potential evaporation rate; T_i is the monthly averaged temperature; J is the heat index; D_o is the potential day length; and M is the bias correction coefficient between the measured values and the estimated values form AOGCM data. Figure 4.1 and Figure 4.2 plot the monthly averaged predicted values under SRES A2 and SRES B1 emission scenarios for precipitation and evaporation rates, respectively. Mean values for these values are shown in Figure 4.3. Also, Table 4.2 gives a summary of the average change of the predicted values for precipitation and evaporation by the reference year 2100. This table clearly indicates that generally the evaporation rate will increase and on the contrary the precipitation rate is expected to decrease which may lead to increase El-Burullus lake salinity values.
As for the sea water level rise, it is chosen according to the IPCC AR4, as shown in Table 4.2. Sea levels will rise by 38 and 51 cm by the end of the 21st century Sea for SRES B1 and SRES A2 emission scenarios. Also, we assume that wind speed and direction, and drain fluxes and its salinity concentrations will remain constant under the different climate change scenarios. Another two reference scenarios are used to evaluate the impact of climate change; 1- current state scenario based on the climate

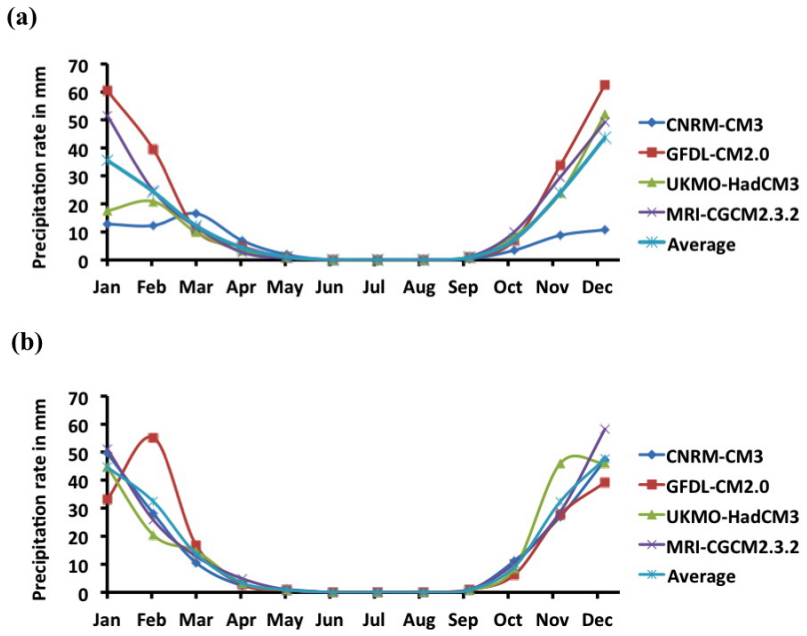

Figure 4.1: AOGCMs models monthly predicted values for Precipitation; (a) SRES A2 scenario and (b) SRES B1 scenario.

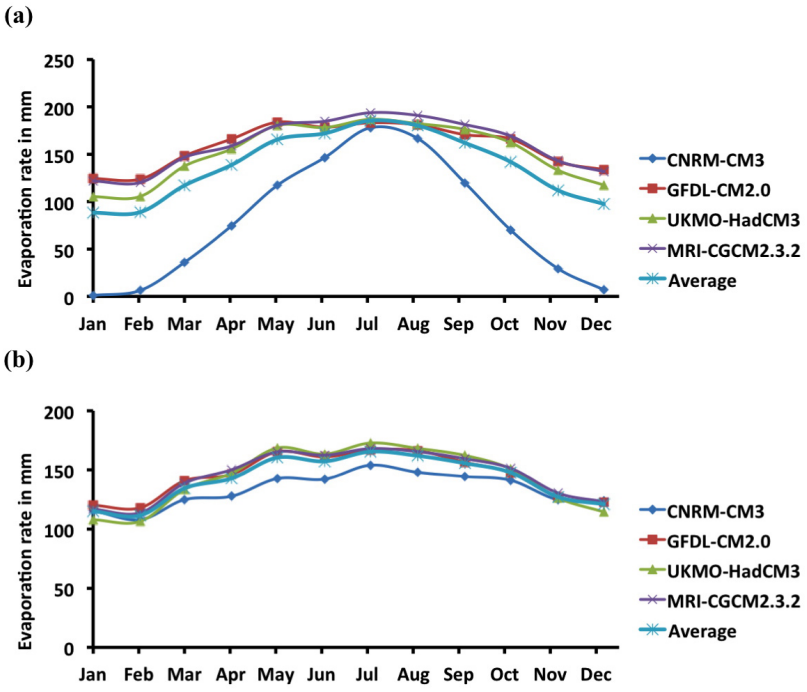

Figure 4.2: AOGCMs models monthly predicted values for Evaporation; (a) SRES A2 scenario and (b) SRES B1 scenario.

data for 2001 which represents the current lake condition, and 2- Benchmark scenario that represents the original condition of the lake before constructing Aswan high Dam. Total discharge routing from all drains for the reference scenarios is presented in Figure 4.6.

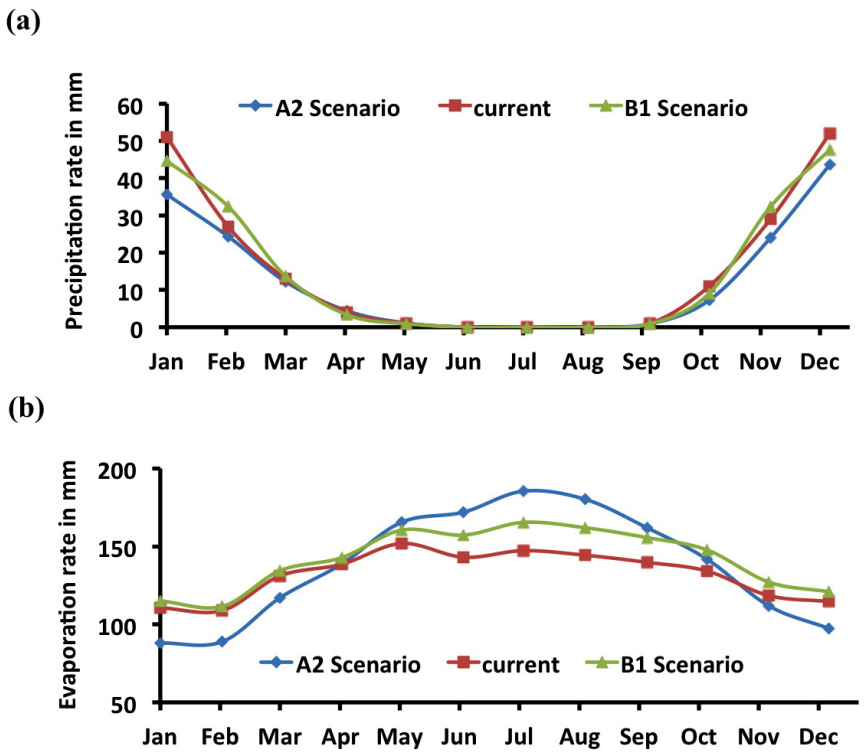

Figure 4.3: Averaged AOGCMs models monthly predicted and present values; (a) Precipitation and (b) Evaporation.

Table 4.2: Summary of climate change scenarios by 2100.

Scenario	Precipitation	Evaporation	Sea level rise (cm)	Wind
SRES B1	-2.16%	+7.42%	+38.00	Fixed
SRES A2	-18.84%	+4.17%	+51.00	Fixed

4.3 Response to Climate Change

To understand the impact of climate change on salinization process occurring in El-Burullus Lake, the calibrated model was used to determine its contribution. The results

Table 4.3: Summary of average salinity changes for different case studies.

Scenario	Benchmark	current	A2	B1
Eastern Area	20.96	5.88	10.85	9.66
Middle Area	7.91	2.44	6.41	5.08
Western Area	3.29	1.50	2.04	2.16

of the climate change simulations are compared to the current state and the benchmark scenarios. Figure 4.4 plots the simulated salinity concentrations at eastern, middle, and western parts of the lake for different scenarios. Sensitivity analysis is used to study the effect of each parameter on salinity values. Figure 4.5 provides a visual presentation of relative sensitivity among precipitation, evaporation and sea level rise for the SRES A2 scenario as a test case. This figure shows that sea level rise is the major parameter affecting salinity values since sea level will increase by approximately 50% of lake's average water depth due to climate change. On the other hand, a coincidence between current state scenario, evaporation and precipitation case studies can be seen. Evaporation and precipitation has a relatively small effect while the total amount of net evaporation (evaporation minus precipitation) will change from 16% to 17.2% of total flux from drains. This change is relatively small to affect salinity values under climate change impact. Table 4.3 presents a summary of the salinity changes at different parts of the lake compared to those of current and benchmark scenarios. Although results clearly show that salinity values will be almost doubled under the effect of climate change, these values are considered relatively small with regard to benchmark case.

4.4 Results and Discussion

Saltwater intrusion into the lake due to climate change scenarios was expected to increase. Accordingly, the lake conditions would be restored to those before the construction of Aswan High Dam. The lake is a complicated system and salinization process depends on different factors. Sea level and drainage flux from different drains are the dominant factors affecting salinity values in the lake. Although sea level will increase by about 50% of the lake's water depth, excessive drainage discharges can resist sea water invasion to the lake. Based on modeling results, it is better to reduce the through flow to the lake during winter closure (from January to March) with a ratio of dQ and to release it again in Summer and Autumn, as shown in Figure 4.6. The term dQ

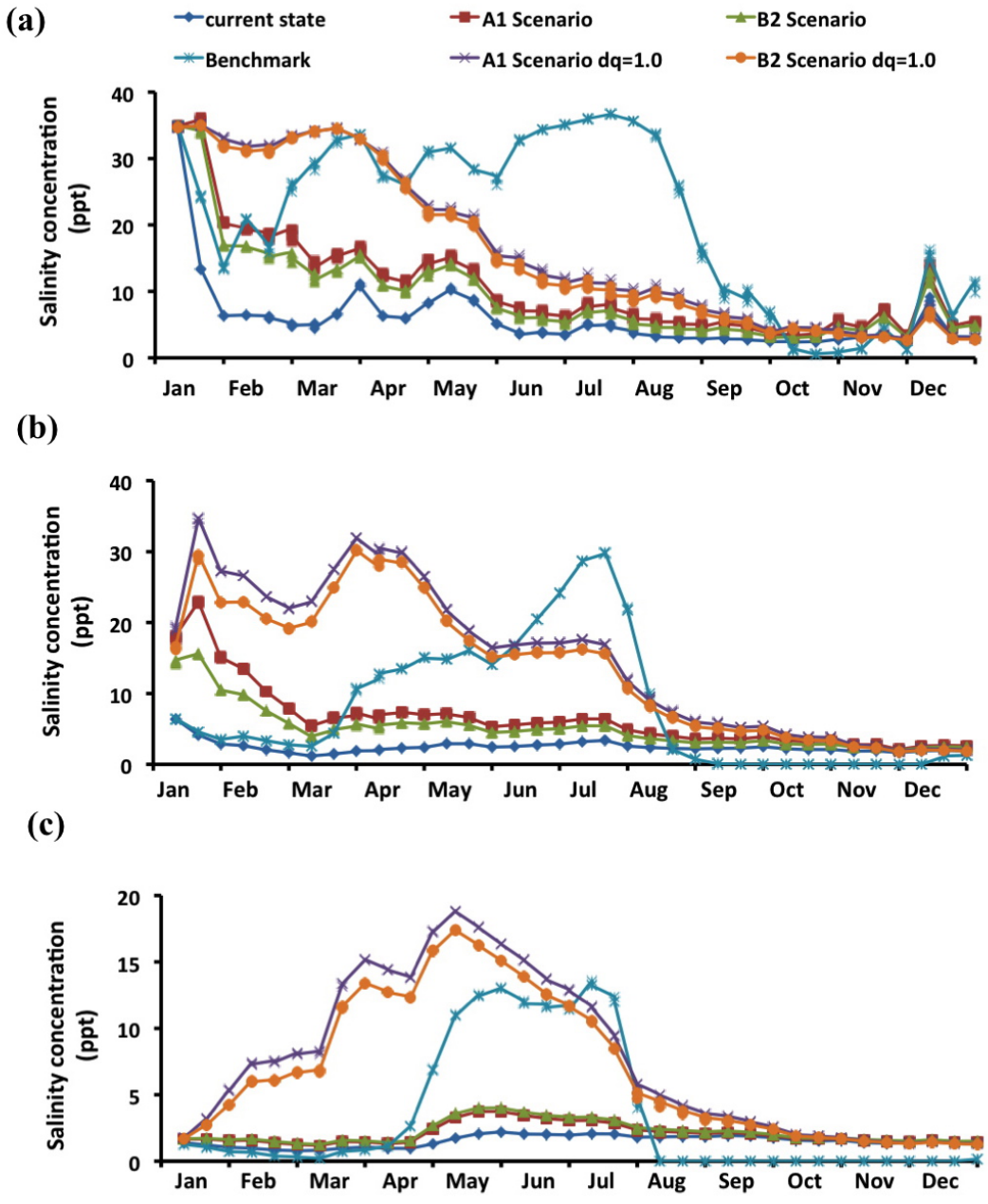

Figure 4.4: Water salinity concentration in the lake results from different scenarios for various areas; (a) eastern area, (b) middle area, and (c) western area.

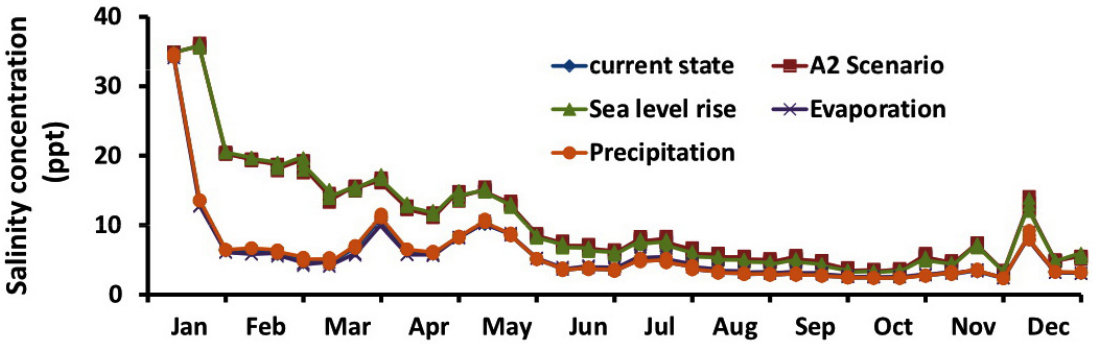

Figure 4.5: The contribution of evaporation, precipitation and sea level rise in changing salinity values under A2 Scenario (eastern area) considering current scenario as a baseline.

is representing the reduced winter drainage flux ratio needed to generate an artificial flood routing similar to the benchmark case routing, (smooth line, Figure 4.6). This dynamic operation is based on changing the interaction between drainage water and sea water to get the best salinity dynamics and to get a better environment for aquatic fauna and flora. Figure 4.7 gives a comparison between water circulation in March between climatic change scenario SRES A2 with dQ = 0.0 (using current state routing) and dQ = 1.0 (using new artificial flood routing). Streamtraces point sources at the lake breach-way are used to visualize water streamlines. For dQ = 0.0, we can observe that water plumes from different drains then gets out of the lake whereas saltwater can remarkably prevail the lake if dQ = 1.0 is used. The reduced winter flow results in less resistance to sea water intrusion and can significantly increase salinity in the lake. Moreover, the new artificial flood routing can expel saltwater out the lake by October. The salinity propagation due to the new routing (dQ = 1.0) is relatively good since salinity values can be increased inside the lake, see Figure 4.4 and Table 4.4.

In addition, the salinity propagation in the lake can be adjusted by changing dQ. Salinity-induced area for salinity values over 10 ppt and 20 ppt as shown in Figure 4.8 are measured. Figure 4.9 plots the percentage salinity-induced area of the lake for different scenarios versus dQ. The Maximum Salinity-induced area for benchmark scenario is 72% and 55% for salinity values over 10 and 20 ppt, respectively. In order to re-originate the lake salinization process, it is recommended to use a dQ value of 0.75 under climate change impact. As a result, the lake salinity values and its ecosystem could be restored to those before constructing Aswan High Dam. In addition, sea water

Table 4.4: Summary of average salinity changes for different case studies after using the new routing.

Scenario	Benchmark	current	A2	B1	A2, dQ=1	B1, dQ=1
Eastern Area	20.96	5.88	10.85	9.66	16.41	15.83
Middle Area	7.91	2.44	6.41	5.08	15.04	13.58
Western Area	3.29	1.50	2.04	2.16	7.55	6.00

is almost free of pollution and the produced relative movement of the lake water will improve the aeration in the lake. Moreover, reeds distribution at the southern and eastern area will be demolished providing much navigation space in the lake. socio-economic status of fishermen will be improved. Based on knowledge of the possible consequences of human activity, monitoring measurements are needed to mitigate the adverse effects or to extend positive results.

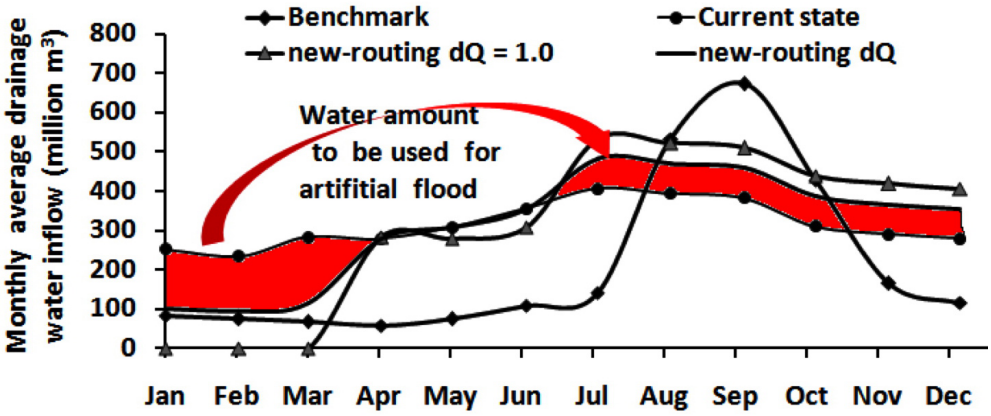

Figure 4.6: Dynamic flow routing to the lake.

4.5 Summary

The present study provides a basis from which decision makers and responders can develop actions and allocate resources to improve and adapt the impacts of climate change and sea level rise. Salinity dynamics have been simulated for various possible scenarios in order to adequately manage temporal salinity in El-Burullus lagoon. Based on SRES A2 and SRES B1 emission scenarios and from four AOGCMs models projections, by the end of 21^{st} century, a reduction of precipitation ranged from 2.16% to 18.84% is expected, a rise of evaporation rate ranged from 4.17% to 7.42%, and a rise of sea level

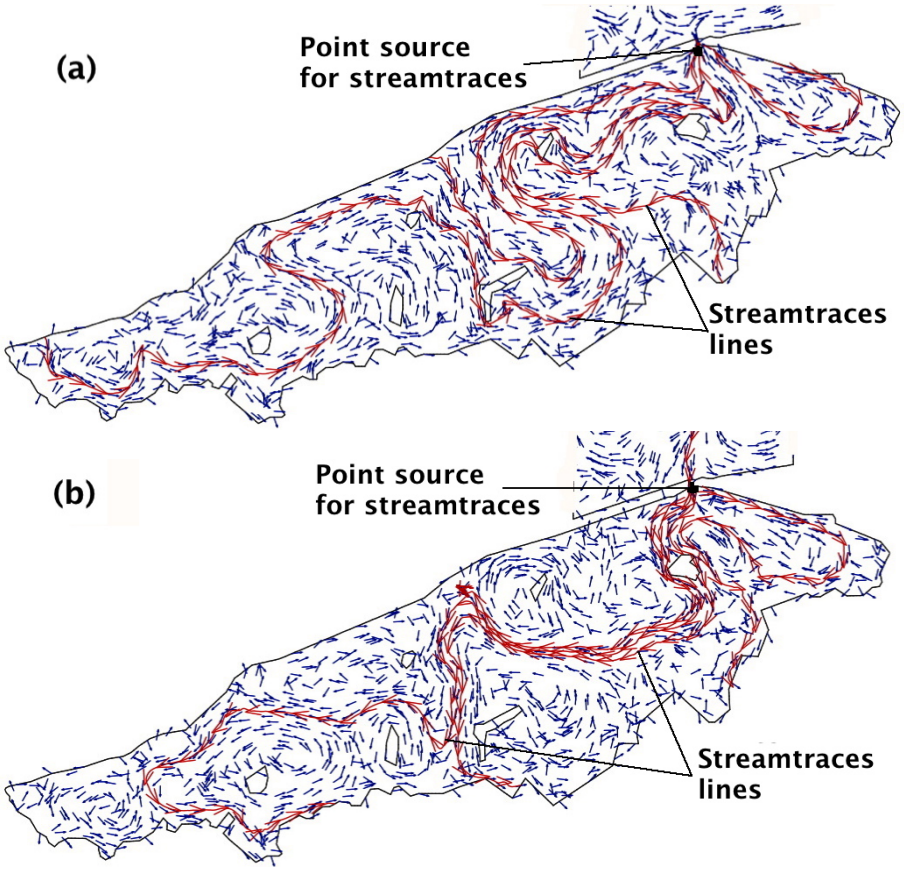

Figure 4.7: Velocity field and water circulation in March inside the lake for scenario SRES A2; (a) case of dQ=0.0 and (b) dQ=1.0.

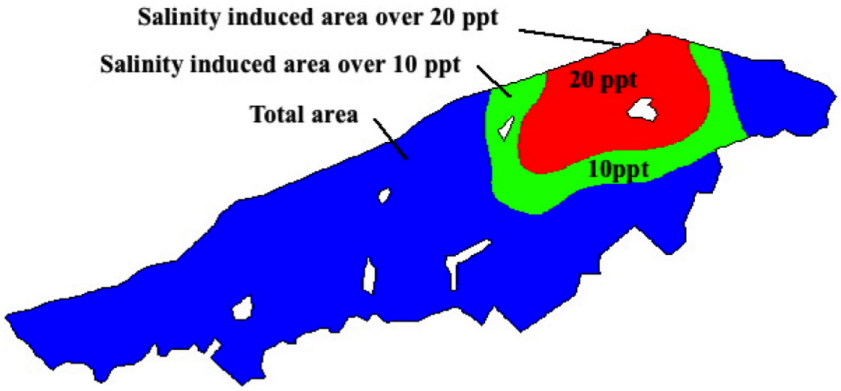

Figure 4.8: Sketch representing the lake salinity induced area for ppt = 10 and ppt = 20.

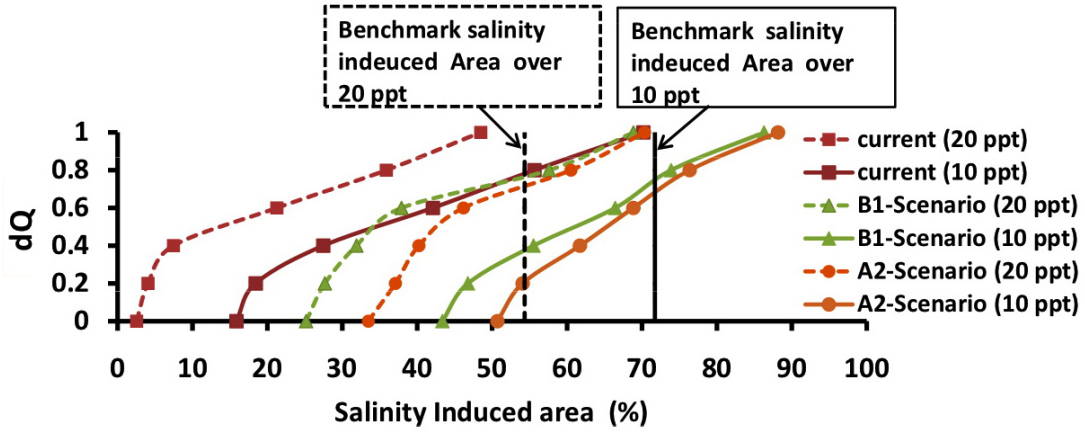

Figure 4.9: Effect of winter discharge reduction ratio (dQ) on percentage of the maximum salinity-induced area of the lake total area for different scenarios. (Solid lines: for salinity-induced area over 10 ppt) and (dashed lines: for salinity-induced area over 20 ppt)

rise of 38.0 cm to 51.0 cm. Climate change will lead to double the salinity values inside El-Burullus lake under the current conditions of drainage flux. Though results show that salinity values will increase to double the current values, they are still much lower than those before constructing Aswan High Dam. These scenarios revealed the importance of fresh drainage water discharges into the lake and the possibility to change the discharge routing. In addition, in order to re-originate the lake salinization process under climate change impact, it is recommended to reduce winter season drainage flux by 75% and release it again uniformly during summer and autumn seasons. This may improve salinity values and circulation in the lake, which may re-originate the lake's aquatic flora and fauna, and enhance its ecosystem.

5

Sediment Transport Modeling

Scour is a natural phenomenon caused by the erosive action of flowing stream on alluvial beds, which is considered as one of the practical moving boundary problems. In this chapter, a depth averaged sediment transport model is developed. Combination between MACS algorithm to track the hydrodynamics of the developed model and the sediment transport model is implemented. This research builds upon recent advances for numerical solutions to couple numerical processes of hydrodynamic, sediment, and bed deformation interaction using the Finite Volume Method (FVM) in discretization. Two approaches of sediment transport modeling are introduced: the equilibrium and the non-equilibrium approaches taking into account current and wave actions in coastal areas. The developed model is validated against different scour problems and its validity is examined. Also, a comparison between the results of the two approaches is discussed.

5.1 Sediment Transport Modeling Overview

The total sediment load is usually separated as bed-load and suspended-load regarding sediment transport mode, or divided into bed-material load and wash load according to sediment source (wash load usually is ignored in the simulation of bed morphological changes). Although there is no sharp division between the suspended-load and the bed-load physically, a bed load layer is assumed to be existent for the mathematical representation. As shown in Figure 5.1, the flow domain is subdivided into two layers vertically. Bed load is confined to move in a thin layer δ in the proximity of the riverbed, above which is the region occupied by suspended-load. The exchange of

sediment between the two layers is through the upward E_b and downward D_b fluxes at the interface. The sediment transport total load can be numerically estimated by two approaches, either jointly as bed-material load (Equilibrium sediment transport model) or separately as bed-load and suspended-load considering the effect of sediment entrainment and deposition from the bed layer (Non-equilibrium sediment transport model). As for sediment transport numerical simulation, there are many two-dimensional (2D) and three dimensional (3D) sediment transport numerical models have been developed to simulate the scour process (e.g. Shimizu et al.(51), 1990, Olsen and Melaaen(52), 1993; Ushijima(53), 1996; Duc et al.(54), 2004; Nagata et al.(55), 2005; Liu et al.(56), 2008; Li and Duffy(57), 2011).

Usually these models use the equilibrium approach or the non-equilibrium approach for suspended-load only. In some cases, the assumption of local equilibrium may lead to unrealistic results that mask the morphodynamic bed change and limit long-term simulations(58). Scouring due to unsteady flow regime or around hydraulic structures are examples of these cases. The non-equilibrium approach for sediment transport was used in river and coastal sedimentation (e.g., Philips and Sutherland(59), 1989; Wu(60), 2004; Sanchez and Wu(58), 2011). This approach is realistic and could simulate the actual phenomena of sediment transport using bed-load and suspended-load sediment transport equations. In the current study, a depth averaged sediment transport model is developed to simulate the bed deformation either by equilibrium or non-equilibrium approaches for the suspended-load as well as the bed-load.

5.2 Bed Deformation

The morphological part of the model uses the previously computed hydrodynamics in chapter 2, since water depth and components of depth-averaged velocity are known. Sediment transport iterations results in evaluation of the bed surface evolution and sediment volumes exchanged between computational cells. The overall sediment transport is governed by the sediment mass-balance equation which appears in the integral form as:

$$(1-p)\int_{\Omega}\frac{\partial z_b}{\partial t}\,d\Omega+\oint_{\partial\Omega}\boldsymbol{q_t}\cdot\boldsymbol{n}\;dl=0 \tag{5.1}$$

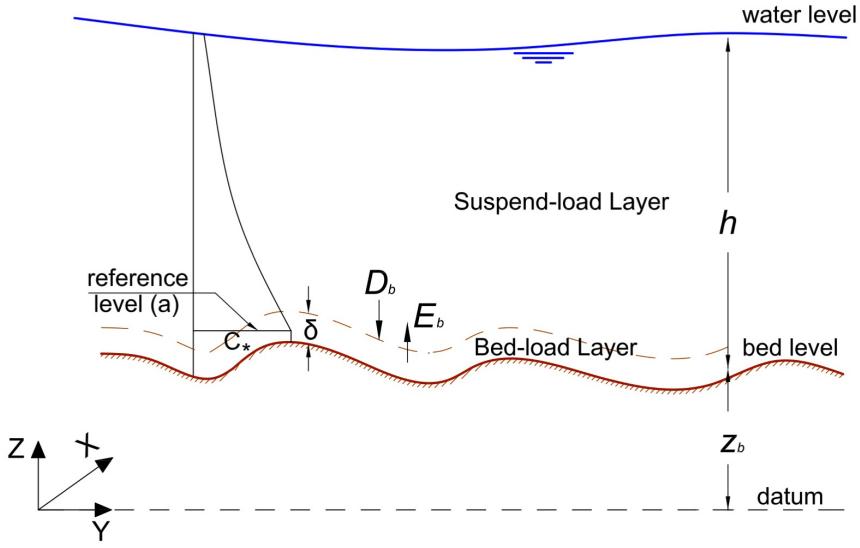

Figure 5.1: Schematic sketch for sediment transport process.

where z_b is the bed level; p is the porosity of the movable bed material; and $\boldsymbol{q}_t$ is the total sediment load transport rate vector in x- and y- directions. The sand bed profile is deformed due to the tractive force generated by turbulent flows and is evaluated by applying the surface integral development and divergence theorem on Eq.(5.1) with triangular cells:

$$z^{n+1} = z^n + \frac{1}{1-p}\,\frac{\Delta t}{\Delta S}\sum_{k=1}^{3} q_{tik}\cdot n_{ik}\; l_k \tag{5.2}$$

with

$$q_{ti} = q_t\,\frac{u_i}{|\boldsymbol{u}|} \tag{5.3}$$

and

$$q_{tik} = f(q_{tiE}, q_{tio}) \tag{5.4}$$

where u_i is the velocity component in x_i direction; $|\boldsymbol{u}|$ is the depth averaged velocity resultant; q_t is the total-load at the cell center which is calculated according to the sediment approach; q_{ti} is the total sediment load vector at the cell center in x- and y-directions; and q_{tik} is the total sediment load vector at the cell boundary k which is estimated by taking the arithmetic average of the cell center as shown in Figure 5.2.

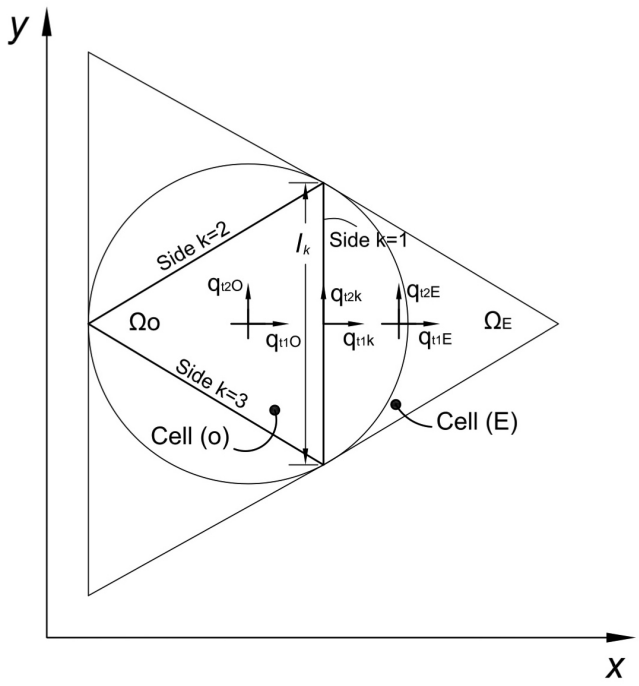

Figure 5.2: Schematic sketch for the unstructured mesh and the sediment transport model parameters.

5.3 Equilibrium Sediment Transport Model

5.3.1 Estimation of total bed-material load

In this model, the sediment total-load is calculated using empirical formulae. There are various empirical bed load transport equations in the literature (Meyer-Peter and Muller formula (61), 1948; Van-Rijn formula (62), 1984). In this model, Ashida-Michiue (1971) formula (63) has been used to evaluate the total bed-load transport q_t as:

$$\frac{q_t}{\sqrt{(s-1)gd_{50}^3}} = 17\ \tau_*^{3/2}\left(1-\sqrt{\frac{\tau_{*c}}{\tau_*}}\right)\left(1-\frac{\tau_{*c}}{\tau_*}\right) \tag{5.5}$$

with

$$s = \frac{\rho_s}{\rho_w} \tag{5.6}$$

$$\tau_{*c} = \frac{u_{*c}^2}{(s-1)gd_{50}} \tag{5.7}$$

$$\tau_* = \frac{u_*^2}{(s-1)gd_{50}} \tag{5.8}$$

$$u_* = \sqrt{\lambda \, |\boldsymbol{u}| \, h} \tag{5.9}$$

where g is the gravity acceleration; d_{50} is the mean diameter of sediment; ρ_s is the sediment density; ρ_w is the water density; τ_{*c} is the non-dimensional critical shear stress; u_{*c} is the critical friction velocity for sand movement which can be evaluated from the formulation proposed by Iwagaki (64); and u_* is the friction velocity which is based on manning roughness formula and can be calculated by Eq.(5.9) and Eq.(2.4).

5.3.2 Equilibrium model application

This model was applied to the experimental results obtained by Michiue et al. (65) to predict local scouring downstream solid apron. The flume was 15.0 m long and 0.40 m wide with longitudinal slope of 1/200. It consisted of 10 m fixed bed followed by 5.0 m alluvial bed with 0.16 m in depth and mean diameter of d_{50} = 0.64mm. The water depth at the downstream end was 0.031 m and the upstream flux was 0.014 m^2/sec.

Figure 5.3 shows the calculated scour hole downstream the solid apron. During model setup, the solid apron length was taken 0.40 m instead of 5.0 m to decrease the computational effort. Figure 5.4 compares the measured and calculated bed changes at time = 10 and 70 min along the channel centerline starting from the solid bed. Good agreement between calculated and measured results was obtained. In particular, at time = 70 min, two successive scour holes are produced and successfully simulated by the present model. The model is able to simulate profiles at different time periods.

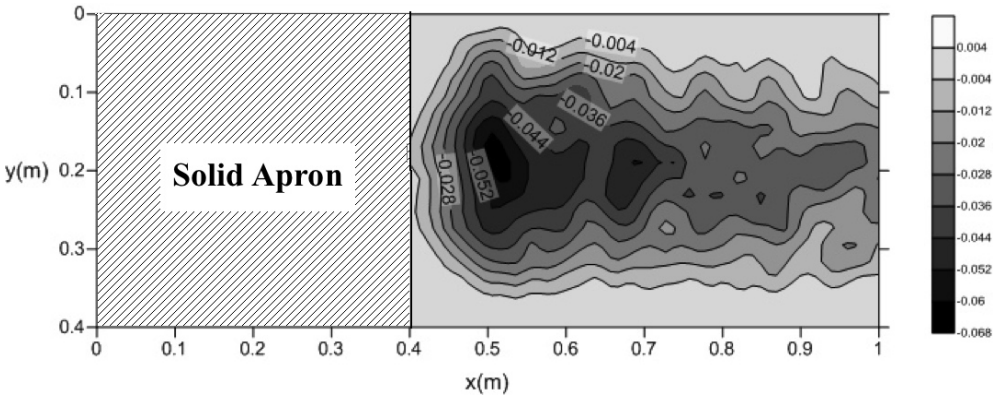

Figure 5.3: Calculated bed change downstream solid apron at time = 70 minutes.

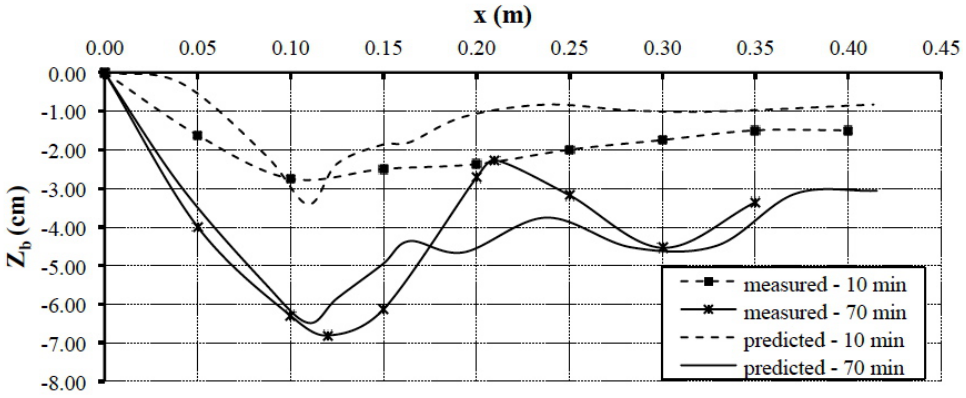

Figure 5.4: Predicted and measured bed changes along the channel centerline at 10 and 70 minutes.

5.4 Non-equilibrium Sediment Transport Model

The sediment which is usually transported by rolling, sliding and saltating along the bed is called bed-load, while the sediment suspended in the water column is termed suspended-load. In the non-equilibrium model, the total sediment transport is divided into bed-load and suspended-load considering the effect of sediment entrainment and deposition from the bed layer as follows:

$$q_t = q_b + q_s \tag{5.10}$$

with

$$q_b = \delta|\boldsymbol{u}|c_b \; and \; q_s = h|\boldsymbol{u}|c_s \tag{5.11}$$

q_t is the total-load sediment transport rate; q_b is the bed-load sediment transport; q_s is the suspended-load while wash-load is usually neglected; c_b and c_s are bed-load and suspended-load concentrations which can be calculated by the advection and advection-diffusion equations, respectively.

5.4.1 Suspended-load transport

The advection-diffusion equation of suspended-load transport is:

$$\int_\Omega \frac{\partial h c_s}{\partial t}\, d\Omega + \oint_{\partial\Omega} \beta h \boldsymbol{u} c_s \cdot \boldsymbol{n}\, dl = \oint_{\partial\Omega} \frac{\nu_t}{\sigma_c} h \nabla c_s \cdot \boldsymbol{n}\, dl + \int_\Omega (E_b - D_b)\, d\Omega \tag{5.12}$$

with

$$E_b - D_b = \alpha w_s (c_* - c_s) \tag{5.13}$$

where c_s is the depth-averaged concentration of suspended load; σ_c is the turbulent Schmidt number for mass diffusion, which represents the ratio of eddy viscosity to eddy diffusivity; β is a correction factor representing the ratio between depth averaged transported mass and flow velocities; E_b and D_b are the entrainment rate and the deposition rate, respectively; $E_b - D_b$ is the source term which presents the net sediment flux at the bed boundary of the suspended-load layer; c_* is the depth-averaged suspended-load concentration under equilibrium conditions or the suspended-load transport capacity; α is an empirical coefficient for suspended load in the range of 0.25-1.0 (60, 66); and w_s is the sediment fall velocity.

5.4.2 Bed-load transport

The mass balance equation in the bed-load zone is:

$$\int_\Omega \frac{\partial \delta c_b}{\partial t}\, d\Omega + \oint_{\partial\Omega} \boldsymbol{q_b} \cdot \boldsymbol{n}\, dl + \int_\Omega \alpha w_s (c_* - c_s)\, d\Omega + (1-p) \int_\Omega \frac{\partial z_b}{\partial t}\, d\Omega = 0 \tag{5.14}$$

where δ is bed-load zone thickness and c_b is the average bed-load sediment concentration.

For dominant bed-load, the bed change can be calculated from:

$$(1-p) \int_\Omega \frac{\partial z_b}{\partial t}\, d\Omega = \int_\Omega \frac{1}{L}(q_b - q_{b*})\, d\Omega \tag{5.15}$$

For dominant suspended-load, the bed change can be calculated from:

$$(1-p) \int_\Omega \frac{\partial z_b}{\partial t}\, d\Omega = \int_\Omega \alpha w_s (c_s - c_*)\, d\Omega \tag{5.16}$$

For a general case

$$(1-p) \int_\Omega \frac{\partial z_b}{\partial t}\, d\Omega = \int_\Omega \alpha w_s (c_s - c_*)\, d\Omega + \int_\Omega \frac{1}{L}(q_b - q_{b*})\, d\Omega \tag{5.17}$$

Therefore, inserting Eq.(5.17) in Eq.(5.14) leads to the non-equilibrium bed load transport equation(60) becomes:

$$\int_\Omega \frac{\partial \delta c_b}{\partial t}\, d\Omega + \oint_{\partial\Omega} \boldsymbol{q_b} \cdot \boldsymbol{n}\, dl + \int_\Omega \frac{1}{L}(q_b - q_{b*})\, d\Omega = 0 \tag{5.18}$$

where q_{b*} is the bed-load concentration capacity and L is an empirical coefficient representing the non-equilibrium adaptation length of bed load and usually is set as the length of bed forms.

In this model α and L are used as tuning parameters for suspended and bed load, respectively. In order to calculate the bed change using the above model, c_* and q_{b*} have to be provided through empirical formulae. These formulae are presented for two cases; case of current only and case of combined current and waves.

5.4.3 Empirical input in case of current

Empirical relations proposed by Van Rijn (1984a, b, c) (62, 67, 68) are used:

$$c_* = 0.015 \frac{d_{50} T^{1.5}}{a D_*^{0.3}} \tag{5.19}$$

$$q_{b*} = 0.053 \left[(s-1)g\right]^{0.5} \frac{d_{50}^{1.5} T^{2.1}}{D_*^{0.3}} \tag{5.20}$$

where D_* is the Particle size parameter

$$D_* = d_{50} \left[\frac{(s-1)g}{\nu^2}\right]^{1/3} \tag{5.21}$$

and T is the excess bed shear stress parameter

$$T = \frac{u_*^{'} - u_{*cr}}{u_{*cr}} \tag{5.22}$$

in which u_{*cr} is the critical bed shear velocity for initiation of motion according to Shields; $u_*^{'}$ is the effective bed shear velocity given by:

$$u_*^{'} = g^{0.50} \frac{|\boldsymbol{u}|}{C'} \tag{5.23}$$

$$C^{'} = 18 \log(12 \frac{R_b}{3 d_{90}}) \tag{5.24}$$

where $|\boldsymbol{u}|$ is the depth averaged velocity; d_{90} is the particle diameter of bed material; and R_b is the hydraulic radius.

The reference level a is chosen as the maximum of (half the bed form heigh Δ or the bed roughness k_s) which are calculated by:

$$\frac{\Delta}{h} = 0.11 (\frac{d_{50}}{h})^{0.3} (1 - \mathrm{e}^{0.5T})(25 - T) \tag{5.25}$$

$$k_s = 3 d_{90} + 1.1 \Delta (1 - \mathrm{e}^{\frac{-3.42\Delta}{h}}) \tag{5.26}$$

5.4.4 Empirical input in case of current and waves

Empirical relations proposed by Van Rijn (2007a, b) (69, 70) are used:

$$c_* = 0.015 \frac{d_{50} T_a^{1.5}}{a D_*^{0.3}} \tag{5.27}$$

$$q_{b*} = 0.015 \rho_s u h (d_{50}/h)^{1.2} M_e^{1.5} \tag{5.28}$$

where T_a is the excess bed shear stress parameter

$$T_a = \frac{\tau_{cwa}^{'} - \tau_{*cr}}{\tau_{*cr}} \tag{5.29}$$

and M_e is the Mobility Parameter:

$$M_e = \frac{u_e - u_{cr}}{[(s-1) g d_{50}]^{0.5}} \tag{5.30}$$

with

$$u_e = u + \gamma u_w \tag{5.31}$$

$$u_{cr} = \beta u_{cr,c} + (1-\beta) u_{cr,w} \tag{5.32}$$

$$\beta = \frac{u}{u + u_w} \tag{5.33}$$

in which τ_{*cr} is the bed shear stress parameter according to shields and $\tau_{cwa}^{'}$ the effective bed shear stress parameter for reference concentration at $z = a$; u is the depth averaged velocity; u_w is the peak wave velocity; $\gamma = 0.40$ for irregular waves and 0.80 for regular waves; $u_{cr,c}$ is the critical velocity for currents based on shields; and $u_c r, w$ is the critical velocity for waves based on Komar and Millar (69) as:

$$\begin{aligned}
&\text{for } 0.00005 < d_{50} < 0.0005 \text{ m} \\
&\qquad u_{cr,c} = 0.19 d_{50}^{0.1} \log(12h/3d_{90}) \\
&\text{for } 0.0005 < d_{50} < 0.002 \text{ m} \\
&\qquad u_{cr,c} = 8.50 d_{50}^{0.6} \log(12h/3d_{90}) \\
&\text{for } 0.00005 < d_{50} < 0.0005 \text{ m} \\
&\qquad u_{cr,w} = 0.24 [(s-1)g]^{0.66} d_{50}^{0.33} T_p^{0.33} \\
&\text{for } 0.0005 < d_{50} < 0.002 \text{ m} \\
&\qquad u_{cr,w} = 0.95 [(s-1)g]^{0.57} d_{50}^{0.43} T_p^{0.14}
\end{aligned} \tag{5.34}$$

5.4.4.1 Wave parameters

Using linear wave theory the following parameters can be calculated:
1- Near-bed orbital excursion:

$$A_w = \frac{H_s}{2sinh(2\pi h/l_w)} \tag{5.35}$$

2- peak wave velocity:

$$u_w = \frac{\pi H_s}{T_p sinh(2\pi h/l_w)} \tag{5.36}$$

3- Wave-boundary layer thickness:

$$\delta_w = 0.072 A_w \frac{A_w}{k_{sw}} \tag{5.37}$$

4- Return velocity mass transport:

$$u_r = -\frac{0.156 g^{0.5} H_s^2}{0.80 h^{1.5}} \tag{5.38}$$

where H_s is the wave height, h is the water depth, l_w is the wave length, T_p is the wave period, and k_{sw} is the effective bed roughness.

5.4.4.2 Friction factors

1- Current grain-related friction coefficient based on $1d_{90}$:

$$f_c^{'} = 0.24[\log(12h/d_{90})]^{-2} \tag{5.39}$$

2- Current grain-related friction coefficient based on k_{sc}:

$$f_c = 0.24[\log(12h/k_{sc})]^{-2} \tag{5.40}$$

3- Wave grain-related friction coefficient based on $1d_{90}$:

$$f_w^{'} = \exp[-6 + 5.2(A_w/d_{90})^{-0.19}] \tag{5.41}$$

4- Wave grain-related friction coefficient based on k_{sw}:

$$f_w = \exp[-6 + 5.2(A_w/k_{sw})^{-0.19}] < 0.30 \tag{5.42}$$

5- current efficiency factor:

$$\mu_c = f_c^{'}/f_c \tag{5.43}$$

6- waves efficiency factor:

$$\mu_w = f_w^{'}/f_w \tag{5.44}$$

$$\mu_{wa} = 0.60/D_* \tag{5.45}$$

here k_{sc} and k_{sw} are the current-related and wave-related bed roughnesses to be equal and set as the bed form height.

5.4.4.3 Effective time-averaged bed-shear stress

1- Bed-shear stress due to current:

$$\tau_c = \frac{1}{8}\rho f_c[v_R^2 + u_r^2]^{0.5} \tag{5.46}$$

2- Bed-shear stress due to waves:

$$\tau_w = \frac{1}{4}\rho f_w U_w^2 \tag{5.47}$$

3- The effective bed shear stress parameter for the reference concentration:

$$\tau_{cwa}^{'} = \mu_c\tau_c + \mu_{wa}\tau_w \tag{5.48}$$

5.5 Sediment Transport Numerical Procedures

Water flow and sediment transport can be calculated using different time scales as shown in Figure 5.5 similar to Ushijima's method (53) according to the studied case as follows:

- The hydrodynamic block solves the initial hydraulics according to the existing domain and boundary conditions, chapter 2.
- Reaching a selected convergence, the flow is considered steady.
- The model enters the morphological block with the computed hydrodynamic data.
- Using the empirical equations, the bed-load and suspended-load capacities, c_* and q_{b*}, are estimated according to the studied case, i.e, for the case of current only, (Eq. 5.19) - (Eq.5.26), and for the case of current and waves, (Eq. 5.27) - (Eq. 5.48).

- The actual suspended-load concentrations are obtained by solving the advection-diffusion equation, (Eq. 5.12).
- The actual bed-load concentrations are obtained by solving the advection equation, (Eq. 5.18).
- The total sediment load is calculated using (Eq. 5.10).
- The surface evolution (erosion or sedimentation) of the cells is estimated, (Eq. 5.2), until one of them exceeds a certain threshold (depending on sediment mean size and water depth).
- When the iteration arrives at this threshold, the model goes back to the hydrodynamic block, estimating new values for hydraulic variables. As convergence is reached again, model goes to morphological block and so on.
- The hydrodynamic part and the morphological part are simulated using two different time scales.
- The real time of the whole process is computed depending on the morphological block iterations because the time between iterations in the hydrodynamic part is a time of adaptation that in reality happens at the same time of morphological processes.

5.6 Non-equilibrium Sediment Transport Model Applications

The present model has been tested to evaluate its applicability producing morphological changes under current and waves actions. Therefore, it was applied to predict two sets of experimental results. The simulation results in these test cases are described below.

5.6.1 Case of current-induced only

This model was applied to the experimental results obtained by Thuc, 1991(71) . He studied sediment transport in shallow rectangular basin. The basin was 5.0 m long and 4.0m wide. The basin was connected to a channel of 0.2 m in width and 2.0 m in length in the upstream side. While a 1.2 m wide and 1.0 m long channel was connected

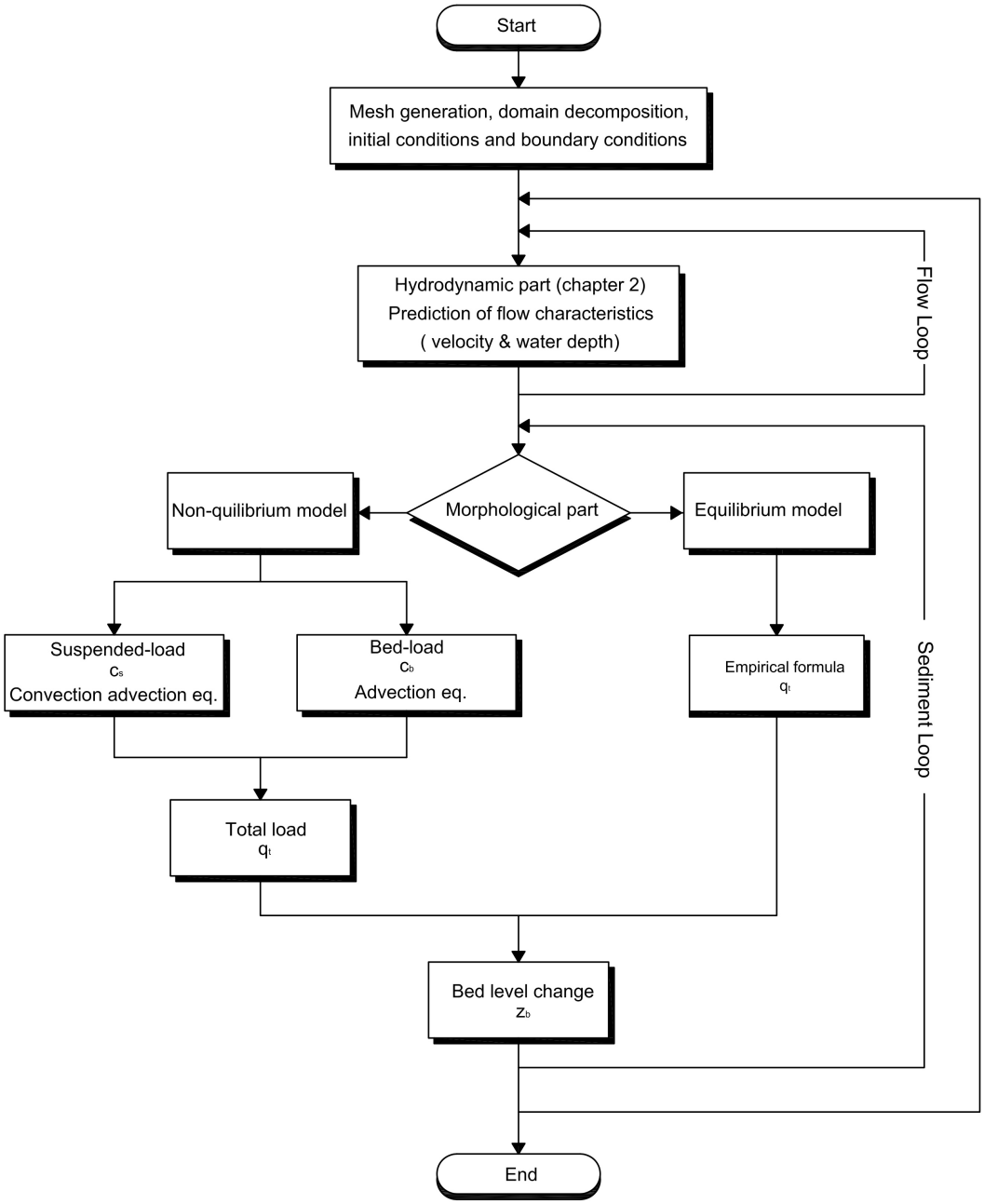

Figure 5.5: Outline of the sediment transport numerical process.

to the outlet side, Figure 5.14. The basin was covered with alluvial bed of 0.16m in depth and had a fall velocity of 0.013 m/s. The water depth at the downstream end was 0.15 m and the upstream velocity was 0.60 m/s. The basin manning roughness coefficient was 0.022. Figure 5.6 shows the estimated flow velocity field that erodes the basin at its inlet. Figure 5.7 compares the measured and calculated bed changes after 1 hour along the basin centerline. The present model successfully simulates the scour hole depth and location. On the other hand, depositions are not well estimated. However, the agreement between calculated and measured results is generally good.

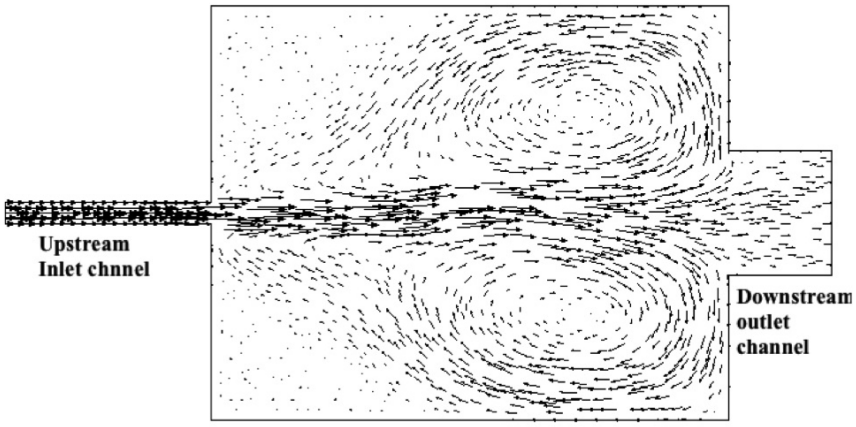

Figure 5.6: Schematic sketch for the shallow basin and the velocity field.

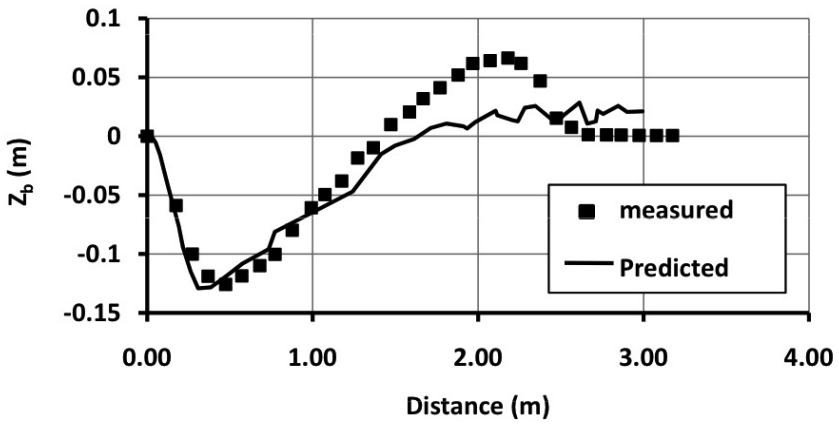

Figure 5.7: Predicted and measured bed changes along the basin centerline.

5.6.2 Case of combined wave and current

Van-Rijn (72) has carried out laboratory experiments concerning sediment entrainment and deposition in a channel perpendicular to the flow direction under wave action. The channel had a side slope of 1:10 and a depth of 0.125m. The experiment was conducted in a 17m long, 0.30m wide and 0.5m deep flume. Figure 5.8 shows the schematic layout of the movable-bed experimental set-up. The upstream current velocity was 0.18 m/sec which resulted in a water depth of 0.225 at the downstream end. A wave paddle at the upstream side propagated regular waves of 0.08 m in height and had a wave period of 1.50 seconds. The current and waves were in the same direction. The initial bed was covered by 0.20 m of sand with a mean diameter of d_{50}= 0.1 mm and d_{90}= 0.13 mm. Sand sediment flux of 0.0167 kg/m/s was supplied at the upstream of the channel to avoid upstream erosion or deposition. The bed evolution was observed after a continuous running of 10 hours. The developed model succeeded in filling the perpendicular channel with sediment. Figure 5.9 compares the estimated bed profile with the measured one. A good agreement between both profiles was achieved.

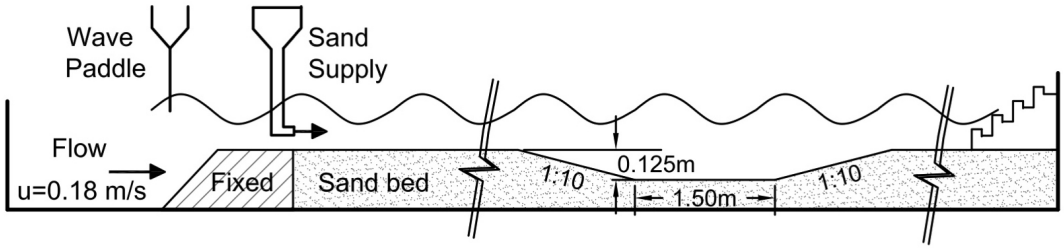

Figure 5.8: Schematic sketch for Van-Rijn experimental set-up.

5.7 Equilibrium and Non-equilibrium Sediment Transport Model Application

The equilibrium and non-equilibrium sediment transport approaches successfully predicted the bed level change in flat bed scour problems. In order to compare both approaches, they were applied on a 3D scour problem to predict a local scour around bridge pier and compared with experimental results. Husain et al. (73) have carried out a series of experiments in straight channel around different types of bridge abutments.

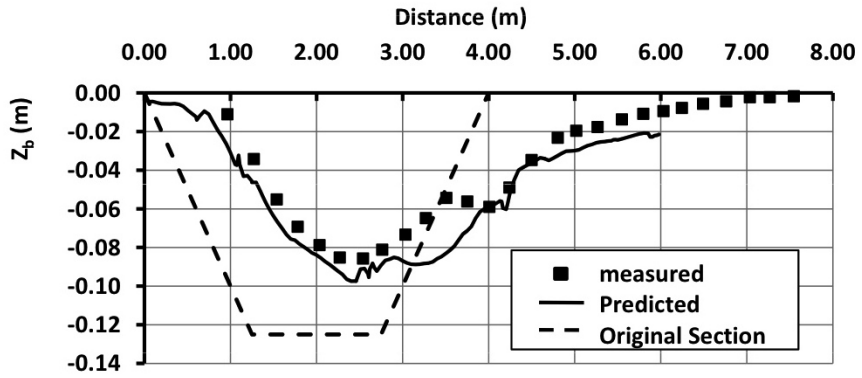

Figure 5.9: Predicted and measured bed changes along the channel centerline.

One of the rectangular abutment cases is selected in this study. The experiments were conducted in a 15 m long, 1.37 m wide and 0.62 m deep glass flume with longitudinal slope of $6.97 \text{x} 10^{-5}$. Figure 5.10 shows the schematic layout of the movable-bed experimental set-up. The selected abutment dimensions are 0.7 m in length and 0.5 m in width, as shown in Figure 5.10. The model of the abutment is attached to one side of the flume in the middle of the test section. The running discharge was 0.06 m^3/sec, which was resulted in a water depth of 0.22 m and an average velocity of 0.199 m/sec. The initial bed was covered by 0.275 m of sand with a mean diameter of d_{50}= 0.775mm. The bed evolution was observed after a continuous running of 6 hours. Figure 5.11 shows the computational domain and the generated cells around bridge abutment. The unstructured grids are intensified near the front and rear abutment's nose. Flow field shows the intensive velocity at the front nose and circulation behind the bridge pier abutment, Figure 5.12.

Figure 5.13 compares the computed results obtained by the equilibrium and non-equilibrium approaches and the measured bed data. For both cases, scour occurs at the front nose of the bridge abutment and deposition appears at the rear nose which is same as the measured data. Also, the scouring extends to the mid length of the abutments upstream side. In case of the equilibrium approach, a large scour hole which has a gentle downstream slope is deformed with greater maximum scour depth of 10.43 cm than the measured value. On the other hand, the non-equilibrium approach produced a narrower scour hole with steep slopes and a depth of 9.45 cm. It seems that the non-equilibrium approach produced a reasonable scour hole shape than the equilibrium one.

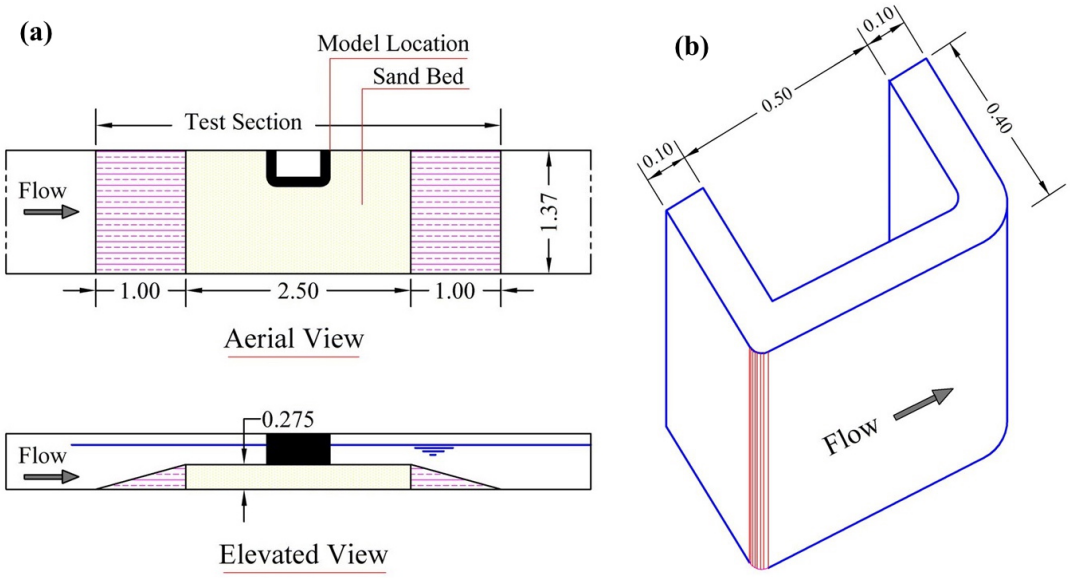

Figure 5.10: (a) Arrangement of the experimental set-up and (b) Schematic sketch for the abutment model. (unit: m)

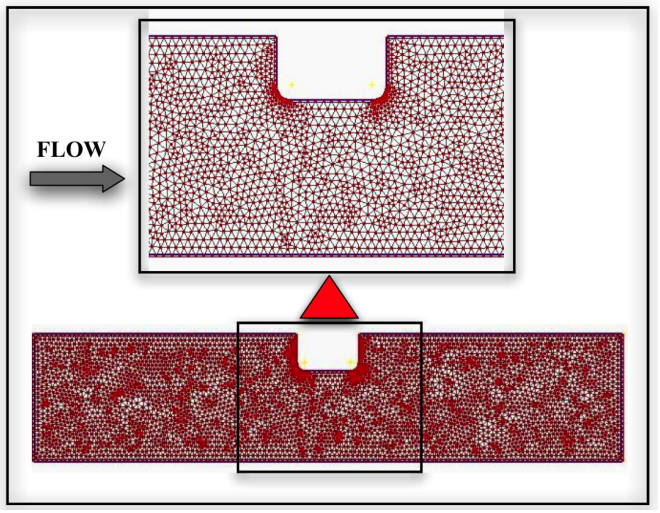

Figure 5.11: Computational domain of the generated unstructured grid and close up for the mesh around the bridge abutment.

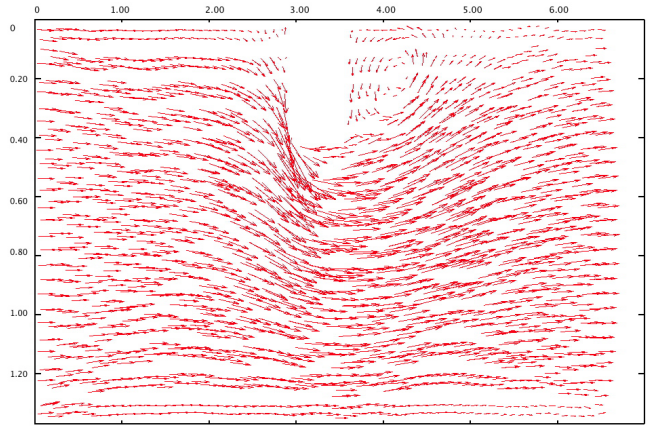

Figure 5.12: Velocity field around the bridge abutment

This may be caused because the effect of the entrainment and deposition between the bed-load and the suspended-load layer was not considered in the later. Also, the tuning parameters α and L played a significant role while developing this results. Although, the non-equilibrium model requires more computational effort, it is recommended to be used under calibrated tuning parameters. The discrepancy between the experimental and computed may be due to not considering the secondary currents effect and the assumption of neglecting the vertical acceleration in shallow water equations (Onda et al. (74), 2006; Hagaiwara et al. (75), 2010). As a result, refinement the hydrodynamic model is needed for better results if a three dimensional application is studied. Taking into account time consideration, computational cost of most sediment transport models and that the studied case is mainly a three dimensional scour phenomena, this results is considered acceptable from engineering point of view.

The computational method was parallelized in a distributed-memory system with a domain decomposition method. Figure 5.14 shows the computational domain which was subdivided into 16 sub-domains to shorten the simulation time. The computation parallel efficiency was investigated using coarse, Medium, and fine unstructured cells with total 687, 1882, and 11538 elements for the scouring problem, respectively. The computations were performed with the T2K open supercomputer M9000, Kyoto University. The parallel efficiency (PE) and the speed-up (SU) can be defined by:

$$PE = \frac{T_{1p}/T_{kp}}{P}, and \quad SU = T_{1p}/T_{kp} \tag{5.49}$$

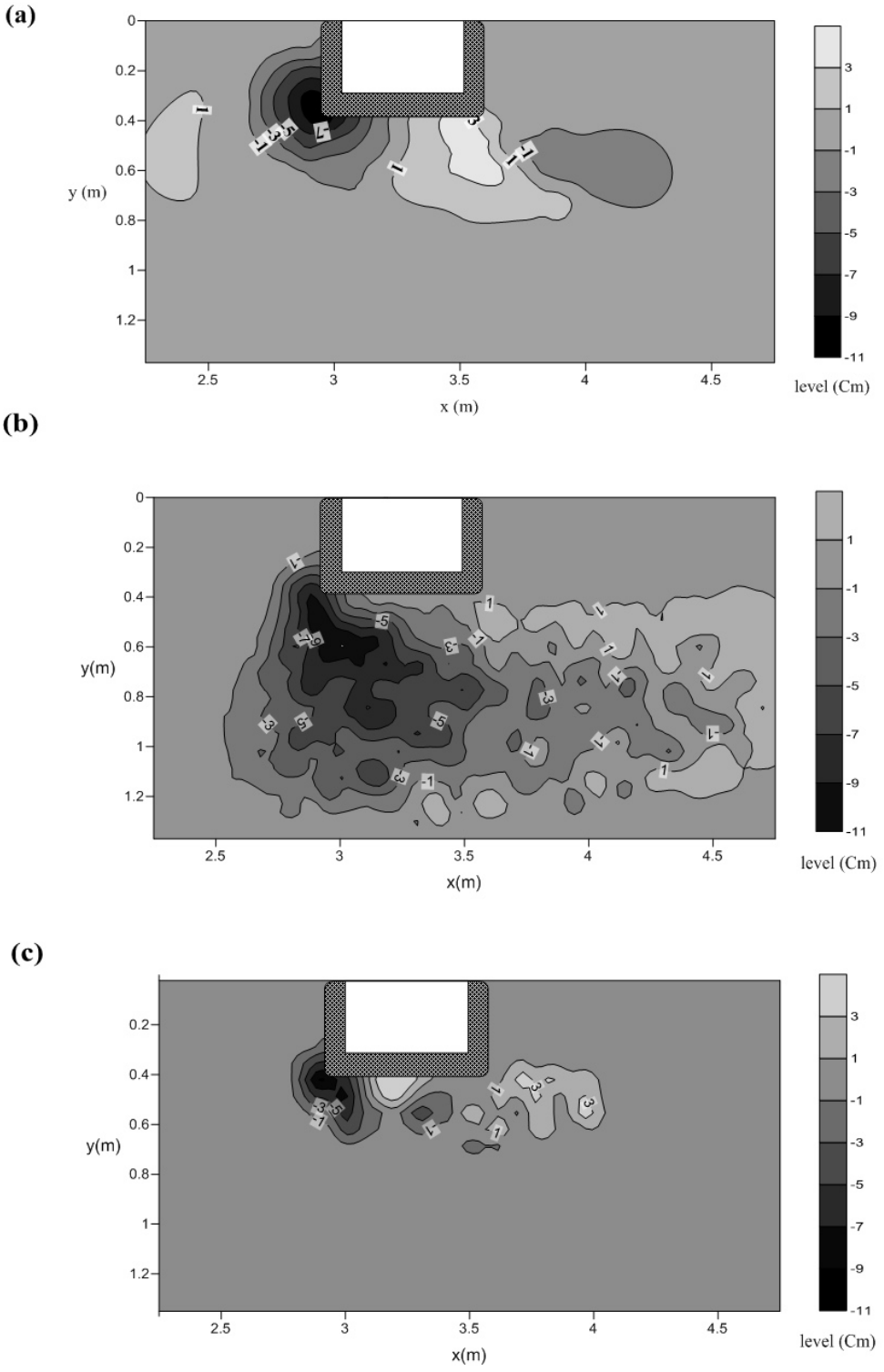

Figure 5.13: Bed variation around the bridge abutment (unit: cm): (a) measured (max. scour depth = 9.90 cm), (b) calculated (max. scour depth = 10.43 cm)cm), and (c) non-equilibrium model (max. scour depth = 9.45 cm).

where T_{kp} is the computational time using k number processors. Figure 5.15 and Figure 5.16 show the speed-up rate and the parallel efficiency using coarse, medium and fine meshes. The parallel efficiency is fair in coarse mesh, but increases when large cells' number is used. It is expected that significant parallel efficiency will be developed if very fine mesh is implemented. Parallel efficiency indicates how efficiently a parallel computation is done. As shown in these figures, the parallel efficiency of the proposed method is satisfactory in large-scale problems.

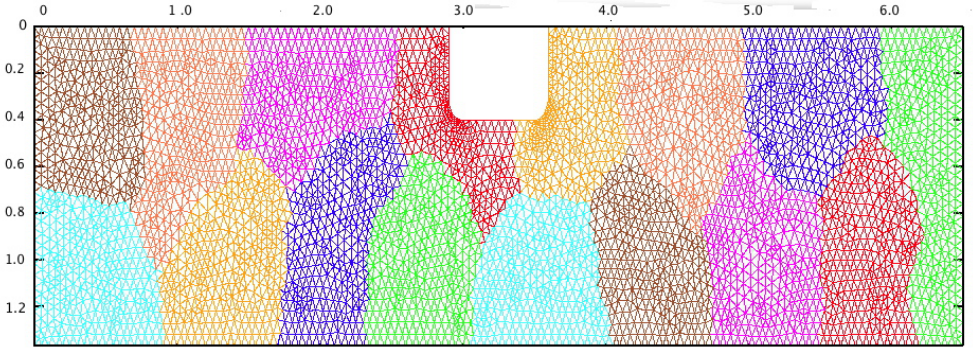

Figure 5.14: Mesh decomposition into 16 subdomains.

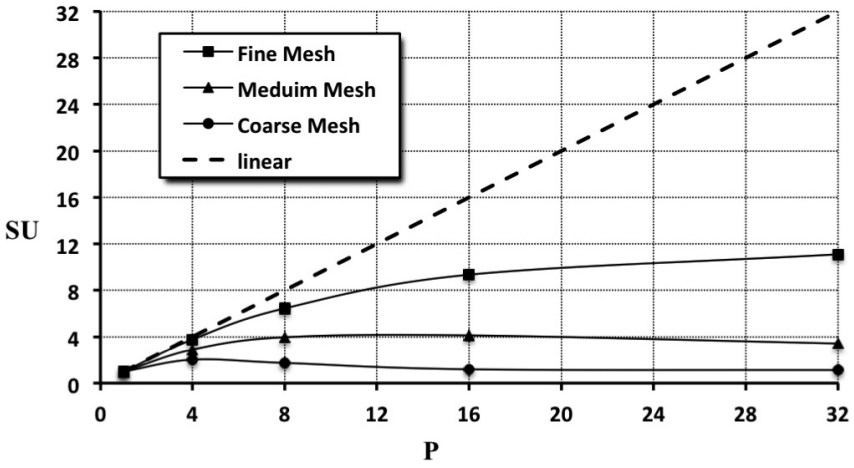

Figure 5.15: The acquiring speed (SU) using multi-process (P).

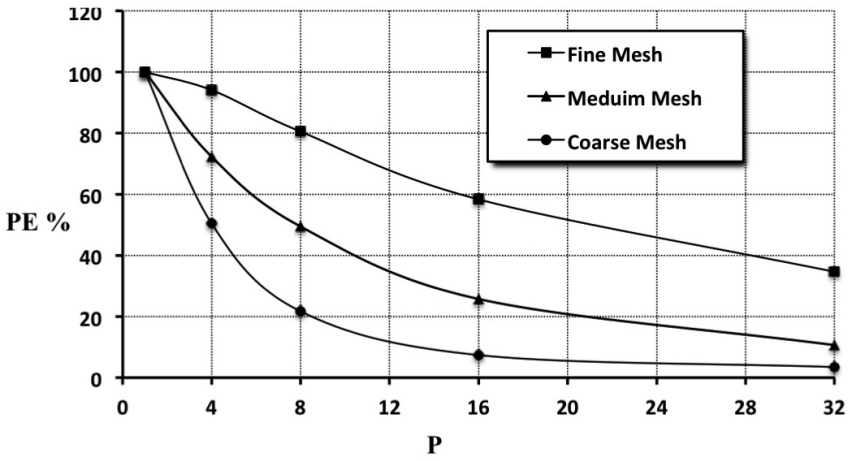

Figure 5.16: Parallel efficiency (PE) using multi-process (P).

5.8 Summary

A numerical prediction method for equilibrium and non-equilibrium sediment transport under current and wave actions has been developed in the present study. The devolved model is based on MACS algorithm with unstructured collocated grid system using the distributed memory system. The partial differential equations for 2D shallow water flow, suspended-load, bed-load sediment and bed evolution were successfully incorporated to predict the bed morphological changes. The developed model has been tested in different laboratory cases: scour downstream solid apron, shallow basin erosion due to clear water, sedimentation in a channel perpendicular to unidirectional flow of current and waves and local scouring around bridge pier abutment. Generally, good agreement was obtained between numerical simulation results and experimental data. This fact shows that the present numerical method is able to predict the sand bed profiles reasonably. The numerical simulation results recommended the use of the non-equilibrium model. In addition, it was demonstrated that the parallel efficiencies are attained by parallel computations.

6

Two-Dimensional Multi-phase Flow High Resolution Model

One of the major goals of this study is to provide a better understanding of which factors control the water salinity in El-Burullus Lake. In chapter 3 and chapter 4, some solutions were proposed to restore the lake salinity dynamics. A new discharge routing was proposed to simulate the flood routing as before constructing Aswan High Dam which may affect the lake stratification. Stratification acts as a barrier restraining the mixing of the water column. As a result of the incomplete mixing of the water column and lack of light for the photosynthesis in deeper layers, the water column may become anoxic. Assessing the exchanges between water layers is important because they influence the trophic organization of the ecosystem. Accordingly, in this chapter, a 2D vertical multi-phase numerical model has been developed for studying stratification process of El-Burullus shallow coastal lake due to density variation. The present model describes a multiphase system for immiscible and incompressible fluids with collocated grid system. The computations are parallelized and simultaneously performed with shared-memory system, which are implemented by OpenMP (Open Multiprocessing). The developed model is validated against the experimental data for the lock-exchange problem. In addition, saltwater intrusion into Ohashi River is simulated and validated using field measured data. Finally, the model is applied on El-Burullus Lake to assess the possibility of its stratification under the new proposed routing.

6.1 Numerical Procedures

6.1.1 Flow governing equations

The basic governing equations for flow are the mass conservation equation and momentum equations, Eq.(6.1)-Eq.(6.2), which describe the flow conditions in the vertical domain Ω as follows:

$$\int_{\Omega} \frac{\partial \rho}{\partial t}\, d\Omega + \oint_{\partial\Omega} \rho \boldsymbol{u} \cdot \boldsymbol{n}\, dl = 0 \tag{6.1}$$

$$\int_{\Omega} \frac{\partial u_i}{\partial t}\, d\Omega + \oint_{\partial\Omega} u_i \boldsymbol{u} \cdot \boldsymbol{n}\, dl = \int_{\Omega} f_i\, d\Omega - \frac{1}{\rho} \oint_{\partial\Omega} p \cdot \boldsymbol{n}\, dl + \oint_{\partial\Omega} \nu\, \nabla u_i \cdot \boldsymbol{n}\, dl \tag{6.2}$$

where t is time; ρ is the cell averaged fluid density; u_i is the velocity component with subscript $i = 1$ and 2 in x- and z- directions, respectively; x and z are the vertical orthogonal coordinates; $\boldsymbol{n}$ is the unit normal vector on the domain boundary $\partial\Omega$ towards the outside direction; p and ν are the average fluid pressure and dynamic viscosity, respectively; and f_i is the external force component due to acceleration.

6.1.2 The interface tracking method

The motion of the interface between immiscible liquids of different densities and viscosities is defined by the volume fraction function ϕ and the interface is convected using the computed velocity field by the following three conditions:

$$\phi = \begin{cases} = 1, & \text{fluid 1} \\ 0 < > 1, & \text{interface} \\ = 0, & \text{fluid 2} \end{cases} \tag{6.3}$$

The time dependence of the volume fraction function ϕ is governed by:

$$\int_{\Omega} \frac{\partial \phi}{\partial t}\, d\Omega + \oint_{\partial\Omega} \boldsymbol{u}\phi \cdot \boldsymbol{n}\, dl = 0 \tag{6.4}$$

Eq.(6.4) states that ϕ moves with the fluid and is considered as a flag identifying cells that contain fluid as shown in Figure 6.1. According to the local value of ϕ, appropriate properties and variables are assigned to each cell within the domain.

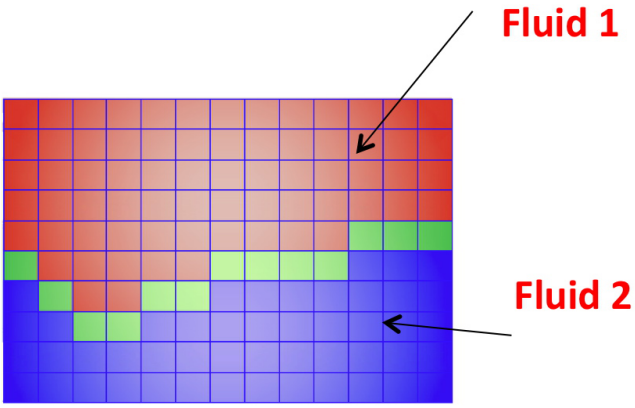

Figure 6.1: Tracking the interface surface between different fluids according to the value of the volume fraction function ϕ.

6.1.3 Convection diffusion equation for transported concentration

The concentration of the transported concentration is obtained by solving the convection-diffusion equation:

$$\int_{\Omega} \frac{\partial c}{\partial t}\, d\Omega + \oint_{\partial\Omega} \boldsymbol{u}c \cdot \boldsymbol{n}\, dl = \oint_{\partial\Omega} \frac{\nu}{\sigma_c} \nabla c \cdot \boldsymbol{n}\, dl \tag{6.5}$$

where c is the transported concentration, and σ_c is Schmidt number for concentration diffusion, which represents the ratio of viscosity to fluid diffusivity.

6.1.4 Computational procedure

The Numerical computation consists of four stages: flow computation, interface tracking, concentration calculation, and updating fluid properties stages. The governing equations are discretized in a collocated grid system and solved with a finite volume method.

In flow computation stage, the flow equations, Eq.(6.1)-Eq.(6.2), are solved according to the existing domain and boundary conditions. Estimated velocity components are obtained at the cell center using pressure at the present computational step while upwind scheme is used to calculate convective terms. The cell center velocity components are interpolated at the cell boundaries. C-HSMAC algorithm (76) is used to correct the pressure field so that the divergence of velocity in a cell should be less than a small threshold value. This algorithm for pressure

computation has the power to deal with large density contrast fluids (77). The cell centered velocity components then are corrected with the obtained pressure values.

In the interface tracking stage, the volume fraction function ϕ is calculated from Eq.(6.4) using the computed velocity field. The interface between different fluids is achieved and hence various fluid zones can be determined.

In the concentration calculation stage, concentrations can be estimated using the convection-diffusion equation, Eq.(6.5), using the computed velocity field.

In the updating fluid properties stage, a simplified equation of state is used to compute density according to the volume fraction function and concentration values, given in a simple linear equations:

$$\rho = \phi\rho_l + (1-\phi)\rho_g \tag{6.6}$$

$$\nu = \frac{\phi\rho_l\nu_l + (1-\phi)\rho_g\nu_g}{\rho} \tag{6.7}$$

with

$$\rho_l = \rho_o + \beta(c - c_o) \tag{6.8}$$

where ρ is the cell average density according to the existing fluid; ρ_l and ρ_g are the densities of two-phase immiscible fluids (liquid and gas); ν is the cell average viscosity according to the existing fluid; ν_l and ν_g are the viscosities of the two-phase immiscible fluids; ρ_o and c_o are the reference density and concentration values which are usually taken as 0.998 g/cm^3 and zero, respectively, for fresh water; and β is the direct proportional coefficient of the salinity gradient between the maximum and minimum value.

Finally, the model goes to the flow computation stage again to calculate the water pressure and the flow velocity field and so on.

6.1.5 Open multiprocessing computation technique (OpenMP)

A parallel computation technique in shared memory system is implemented in the present model. This model is parallelized by OpenMP (Open Multiprocessing) (78). OpenMP is an implementation of multithreading, a method of parallelizing whereby a master thread (a series of instructions executed consecutively) forks a specified number of slave threads and a task is divided among them, Figure 6.2. The threads then run concurrently, with the FORTRAN runtime environment allocating threads to different processors. This process enables us to significantly reduce the elapsed time of the large-scale computations.

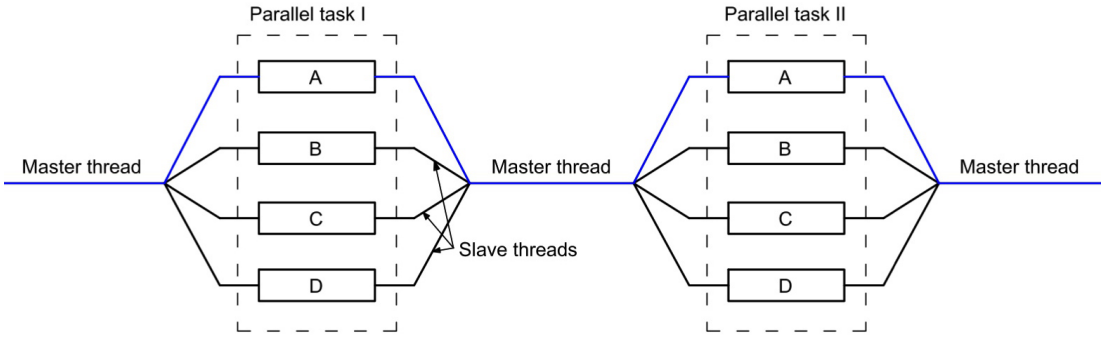

Figure 6.2: An illustration of multithreading process where the master thread forks off a number of threads which execute blocks of code in parallel.

6.2 Model Validation With Experimental Results

The present model has been tested to evaluate its applicability. Therefore, it was applied to density stratification problems and compared with experimental results and field data. The simulation results for these test cases are described below.

6.2.1 Lock-exchange problem

The lock-exchange test or dam break problem is defined as water of different densities are separated by a vertical barrier which is removed at time zero. Lock exchange involving fluids either with small density differences (the Boussinesq case) or with large density differences (the non-Boussinesq case). The removal of the barrier results in a gravity current of the lighter fluid propagating at constant speed along the upper

surface of the channel into the heavy fluid. In the opposite direction a gravity current of the heavier fluid propagates also at constant speed along the bottom of the channel. The lock-exchange test represents mixing processes that occur frequently in geophysical fluid dynamics. For the Boussinesq case: When a fresh water river empties into a salt water estuary while for the non-Boussinesq case: the volcanic eruptions often take the form of gravity currents. The density within the flow is a result of suspended ash and hot rocks, and is often many times larger than the surrounding air. Figure 6.3 presents a sketch for the used the lock-release cell, showing two fluids of densities ρ_1 and ρ_2, each having a depth of H and separated by a removable lock gate. Herein, the Boussinesq and Non-Boussinesq lock-exchange tests have been used to validate the developed code.

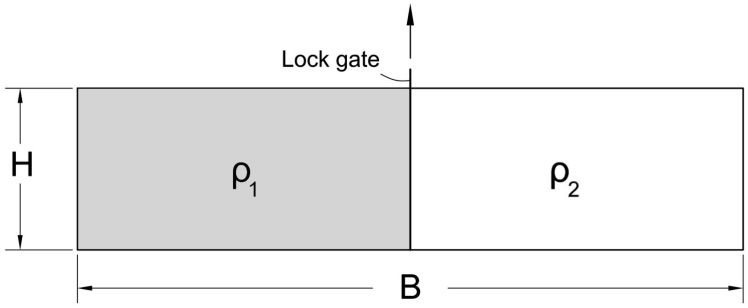

Figure 6.3: Sketch of the lock-release tank.

6.2.2 Boussinesq lock-exchange experiment

This model was applied to the Boussinesq lock-exchange experimental results obtained by Kolar et al. (79). The density cell had internal dimensions of length (B) = 58.4 cm, height (H) = 29.5 cm, and width = 2.54 cm. The both mixing fluids were initially separated by the barrier which was 0.4 mm thick of stainless steel sheet. The both mixing fluids were fresh water and saline water with a salt concentration of 17.5 ppt. Water at room temperature was used, resulted in a heavy water density (ρ_1) of = 1.011 g/cm^3 and a light water density (ρ_2) of 0.998 g/cm^3, for a density ratio of 0.987, which was clearly in the Boussinesq realm.

Herein, we present high resolution outcomes for direct and quantitative comparison of experimental and numerical results throughout the domain, not just the wave front. Figure 6.4 compares the model results with the laboratory experiments and determines how well the model captured the evolution of a density field that is driven entirely

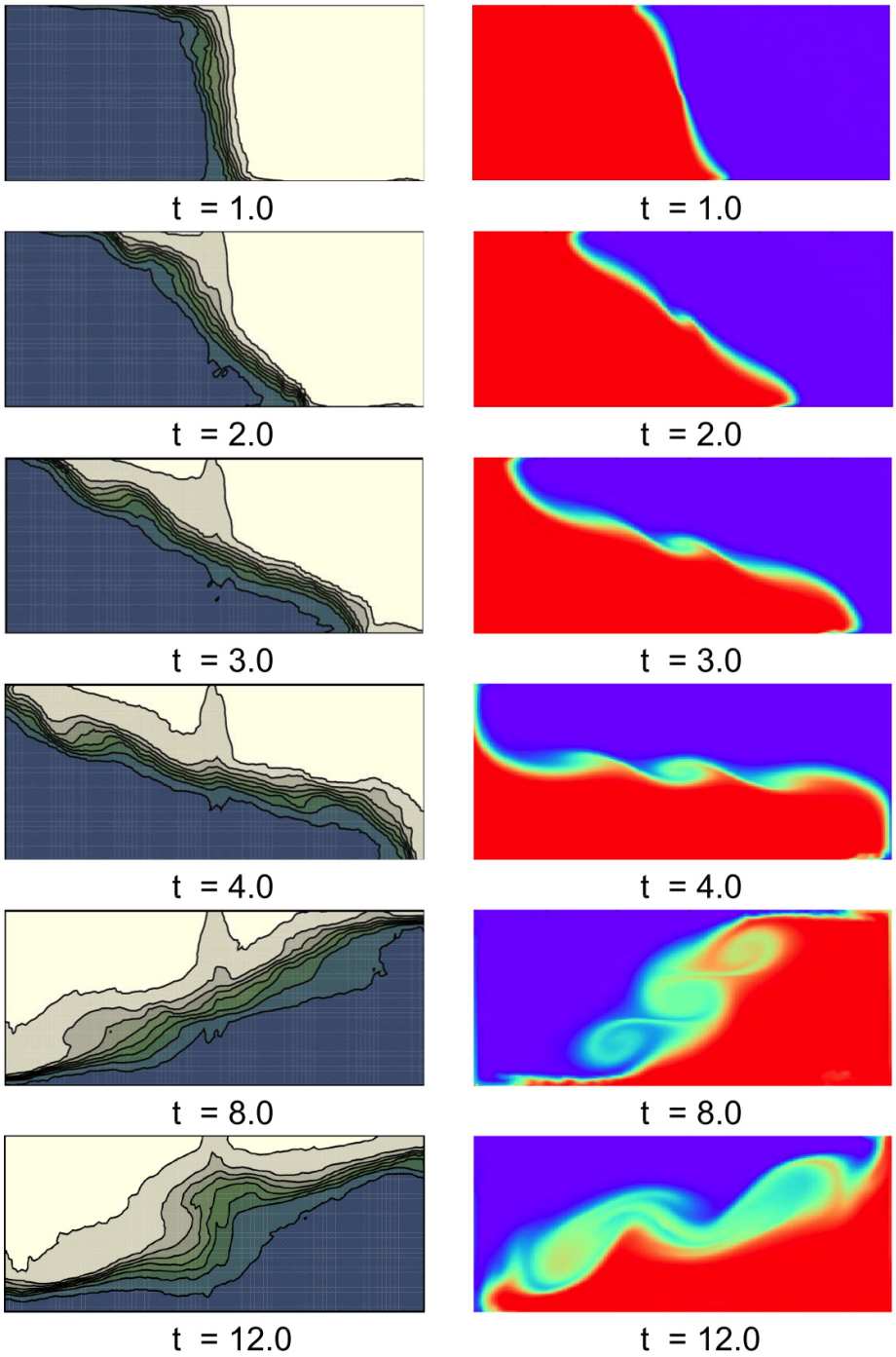

Figure 6.4: Comparison of experimental and predicted results for the density current propagation sequences for the Boussinesq lock-exchange case; (left) laboratory results and (right) model results.

by gravity currents.This figure clearly shows a good agreement between the calculated density propagation of the wave front compared with those which are experimentally measured. In addition, a coincidence between the front position for the estimated and the measured data was obtained as shown in Figure 6.5.

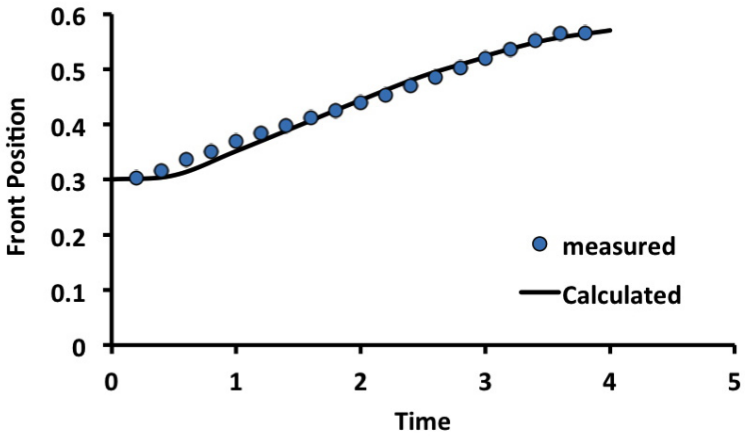

Figure 6.5: Comparison of the front position estimated from the laboratory experiments and the present model for the Boussinesq lock-exchange case.

6.2.3 Non-Boussinesq lock-exchange experiment

Lowe et al. (80) have carried out a series of experiments on the lock exchange involving fluids with large density differences - the non-Boussinesq case. One of the experiments is selected in this study. The experiments were performed in a rectangular channel using two fluids of density ratio ($\gamma = 0.681$). The less dense fluid was freshwater ($\rho_2 = 0.998$ g/cm^3) and the denser fluid was either a solution of sodium chloride (NaCl) or sodium iodide (NaI) ($\rho_1 = 1.466$ g/cm^3). The channel length was B = 182 cm, 23 cm wide and was filled to a depth of H = 20 cm. The flow was started by a vertically removing lock gate.

Figure 6.6 compares the model results with the laboratory experiments and determines how well the model captured the evolution of a density field that is driven entirely by gravity currents. This figure clearly shows an acceptable agreement between the calculated density propagation of the wave front compared with those which are experimentally measured but in a different time scale. In addition, the developed model successfully predicted the bore within the heavy front. The front velocity of the

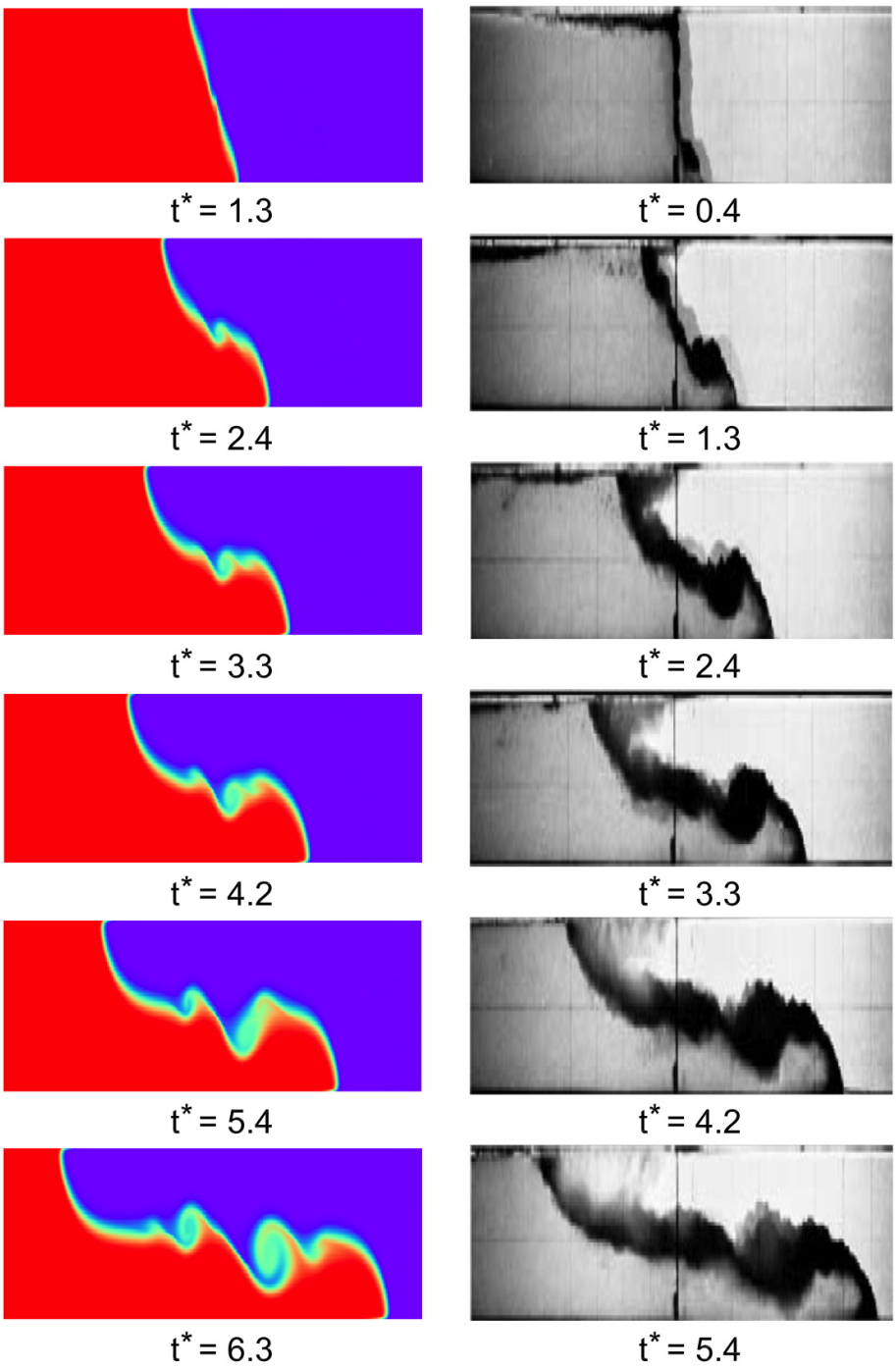

Figure 6.6: Comparison of experimental and predicted results for the density current propagation sequences for the non-Boussinesq lock-exchange case, (where $t^* = t\sqrt{(g(1-\gamma))/H}$); (left) model results and (right) laboratory results.

density current is almost the same for the light case as well as the heavy case as shown in Figure 6.7 and Figure 6.8. In the heavy front case, discrepancy may be observed because of the gate removal effect.

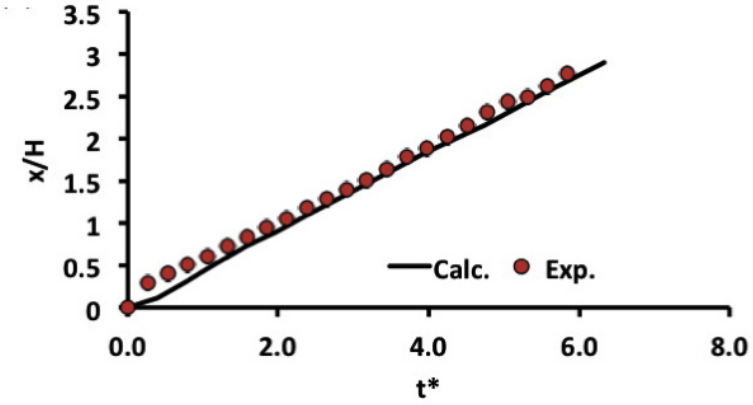

Figure 6.7: Comparison of the relative front position estimated from the laboratory experiments and the present model for the non-Boussinesq lock-exchange case for light front.

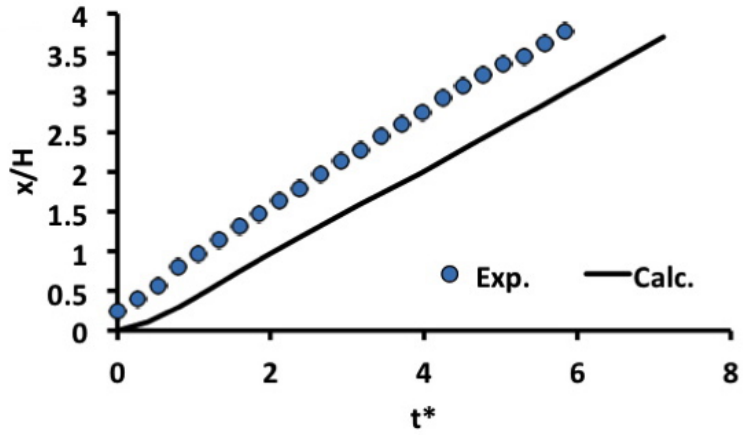

Figure 6.8: Comparison of the relative front position estimated from the laboratory experiments and the present model for the non-Boussinesq lock-exchange case for heavy front.

6.3 The Model Application on Ohashi River, Japan

The Ohashi River in southwest Japan is a tidal river located between two brackish lakes, Shinji and Nakaumi, Figure 6.9. These brackish lakes are stably stratified due

to salinity (density) differences. Nakaumi Lake is strongly affected by the salt water entering from the Sea of Japan through Sakai channel while the freshwater Hii River influenced on Lake Shinji. The density gradient has a significant impact on water movement in the Ohashi River. In this study, the field measured data (September 10, 1999) for the saltwater intrusion into the Ohashi River are used to validate the present model(81). Figure 6.9 shows the nine measuring stations along the Ohashi River.

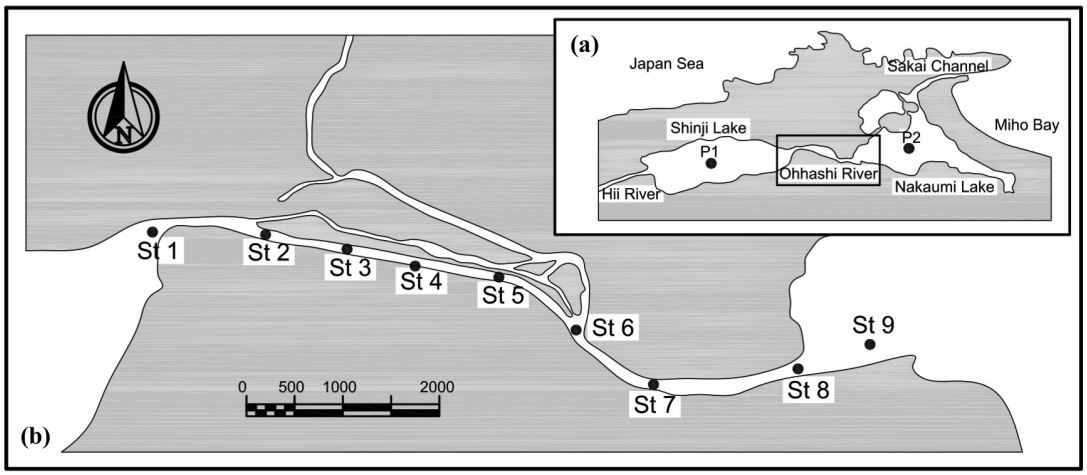

Figure 6.9: Geographical location of the Ohashi River and sampling locations: (a) location in the Lake Shinji-Nakaumi system and (b) nine sampling localities in September, 1999.

The salinity initial conditions of the salinity concentration values, computational domain, and the two lakes water levels are introduced in Figure 6.10. The model run starting time was 10:30 Am. The used simulation time period was chosen to decrease the effect of temperature on density values. The computational domain was separated vertically into two phases, air at top and water at bottom with different concentrations. A computational time step of 0.1 sec. and a computational grid of 0.25m and 100m in the vertical and the horizontal directions, respectively, were used in the numerical calculations. The linear wave theory was used to calculate the intrusion water flux from Lake Nakaumi using the water level difference between the two lakes. The model results show good agreement against the measured data for salinity concentrations at 14:30 Pm and 16:30 Pm as shown in Figure 6.11 and Figure 6.12. However, model refinement is needed to avoid the stripping shape of salinity concentrations.

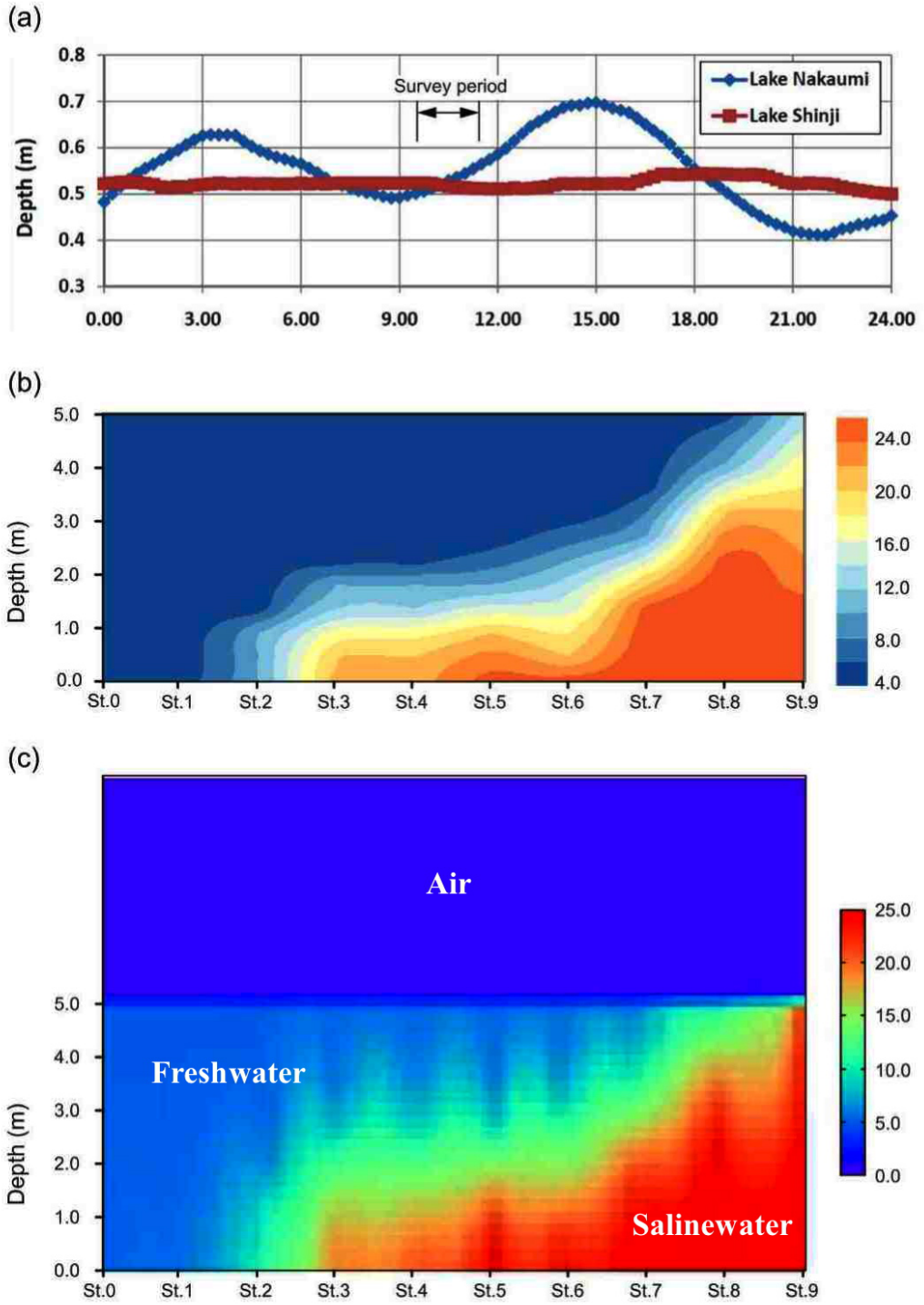

Figure 6.10: Initial conditions at 10:30 Am: (a) water level fluctuation, (b) measured salinity values along the Ohashi River, and (c) estimated salinity values along the Ohashi River.

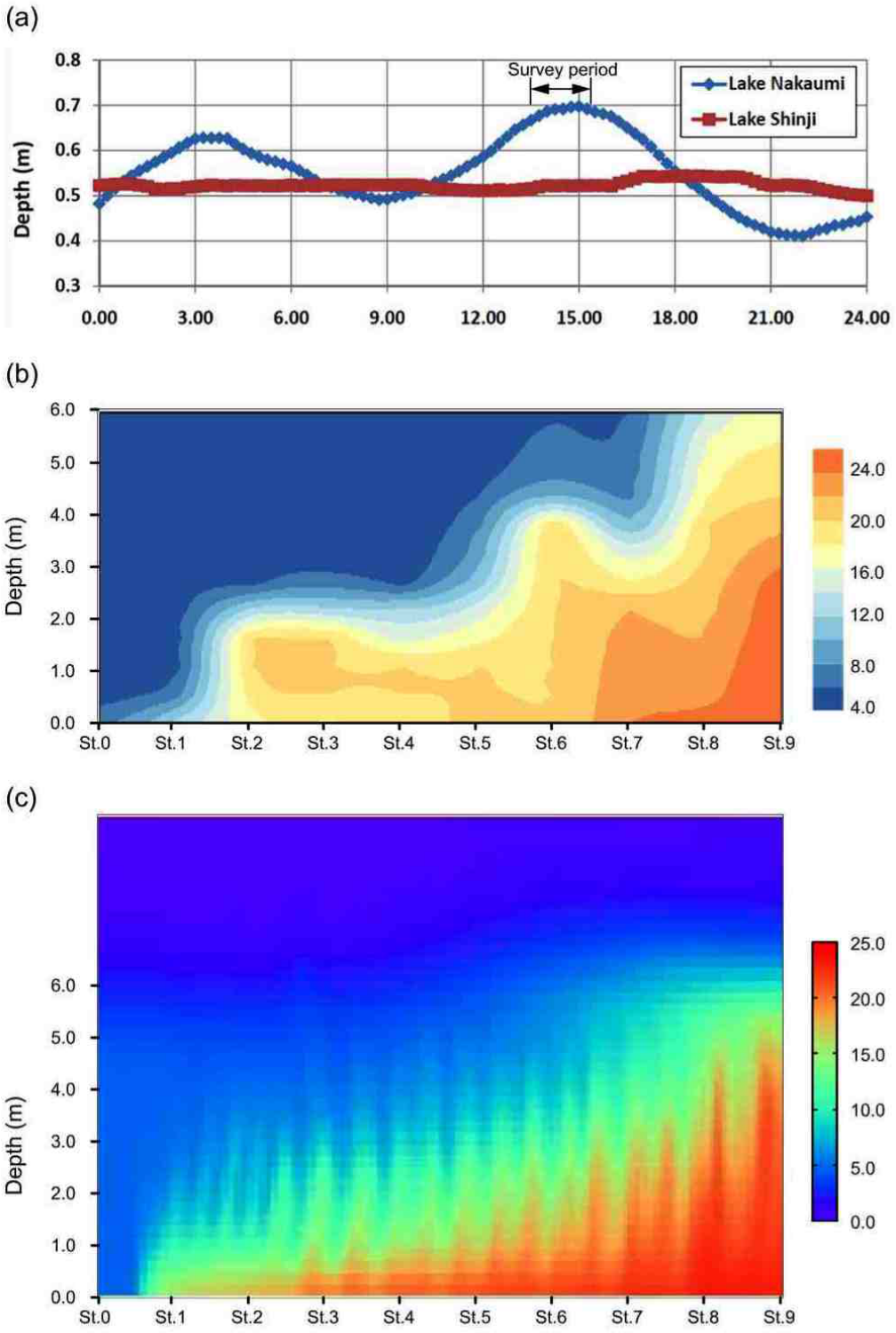

Figure 6.11: Comparison of the measured and the estimated results at 14:30 Pm: (a) water level fluctuation, (b) measured salinity values along the Ohashi River, and (c) estimated salinity values along the Ohashi River.

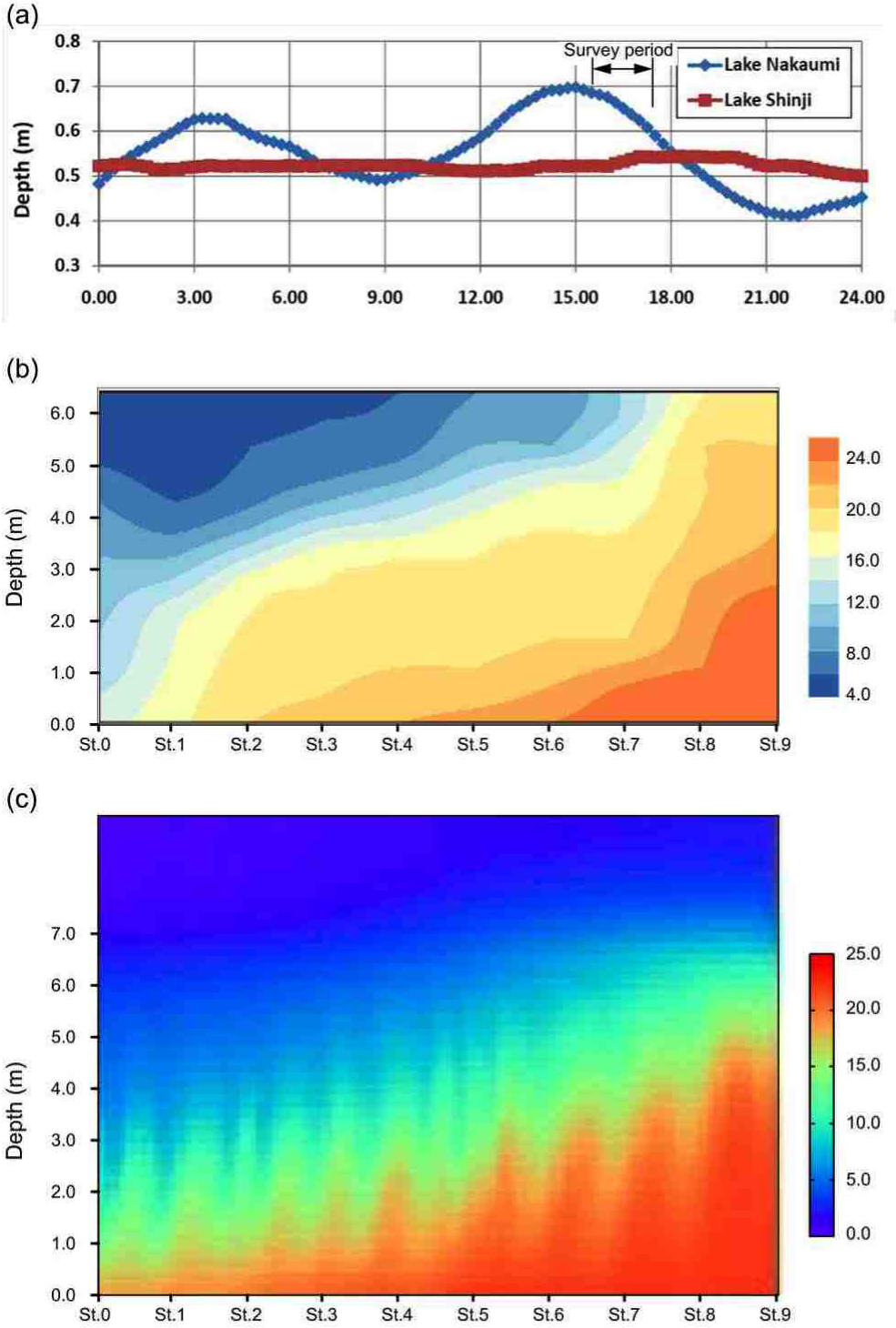

Figure 6.12: Comparison of the measured and the estimated results at 16:30 Pm: (a) water level fluctuation, (b) measured salinity values along the Ohashi River, and (c) estimated salinity values along the Ohashi River.

6.4 The Model Application on El-Burullus Lake

The present model is applied on El-Burullus Lake breach-way, Figure 6.13. The lake hydrodynamic behavior, salinity propagation and the effect of changing the fresh water routing on the lake stratifications are studied for further understanding. The lake was studied under actions of the total flux of fresh water and sea water level boundary conditions as shown in Figure 6.14. Due to the lake shallowness, the water density is assumed to be varied based on the salinity concentration differences where the vertical temperature distribution is considered almost uniform. The numerical simulation results revealed the effectiveness of the new routing. The salinity can intrude the lake as shown in Figure 6.14. In addition, It is necessary to use the three dimensional study because of the horizontal propagation of the salinity current cannot be considered by the present model.

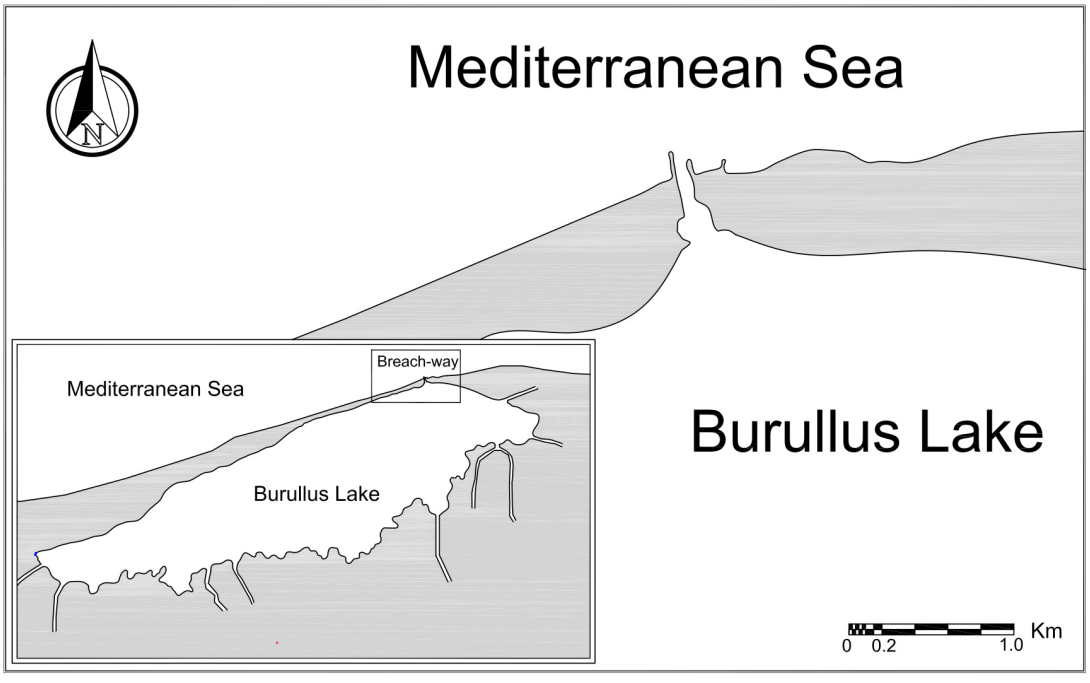

Figure 6.13: Geographical location of El-Burullus breach-way.

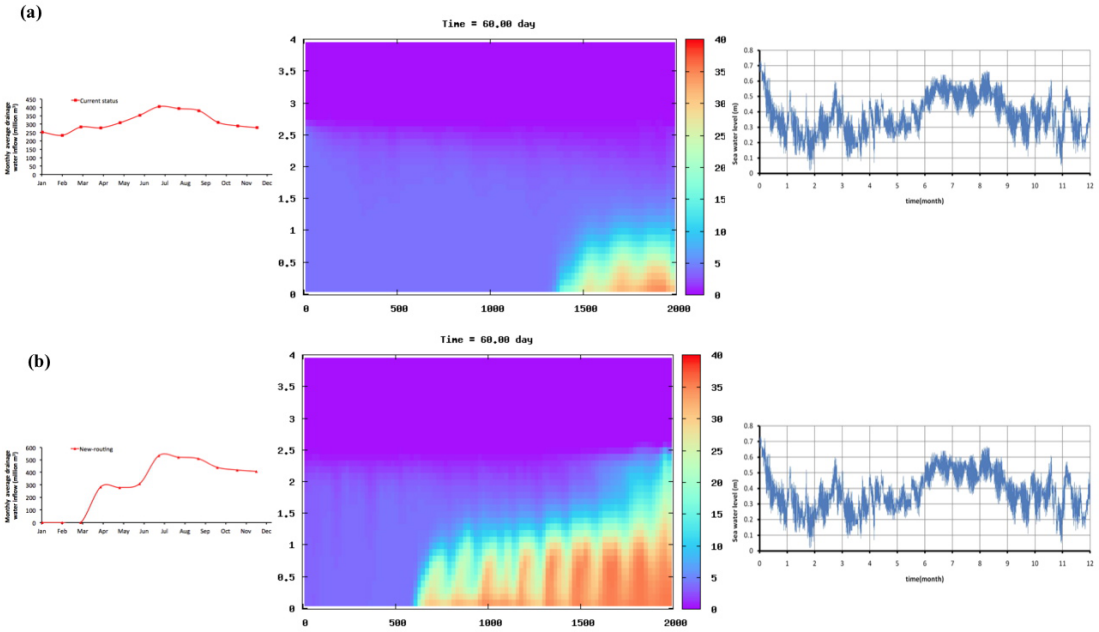

Figure 6.14: Layout of the used boundary conditions; (a) case of current status routing and (b) case of new-routing.

6.5 Summary

A two-dimensional multiphase numerical model for incompressible, immiscible and variable density fluids has been developed to study stratification process of brackish coastal lakes due to density variation. The governing equations are discretized in a collocated grid system and solved with a finite volume method. The developed model successfully predicted the density current propagation in the lock-exchange problems for Boussinesq and non-Boussinesq experimental cases. In addition, saltwater intrusion into Ohashi River is simulated and validated using field measured data. The predicted model still needs refinement to avoid concentration oscillations. The present model is applied on El-Burullus Lake for further understanding of the lake hydrodynamic behavior and the effect of changing the fresh water routing on the lake stratifications. The lake was studied under actions of the total flux of fresh water and sea water level boundary conditions. The numerical simulation results revealed the necessity of the three dimensional study.

7

Three-Dimensional Multiphase Model

In this chapter, the computational method for multiphase fields, MICS, (Multiphase Incompressible flow solver with Collocated grid System) is used to detect the density current propagation (82). This method predicts the interaction between three-dimensional (3D) free surface flows and solid bodies. The free-surface flow including solid objects is modeled as a multiphase flow field. The governing equations for the field are solved on the basis of a finite volume method with collocated grid system. Computations are simultaneously performed with the distributed-memory system which allows us to significantly reduce the elapsed time of computation. The model is validated against the experimental data for the lock-exchange problems and the shallow coastal lake system.

7.1 Numerical Procedures

7.1.1 Basic equations

In MICS method, the multiphase field Ω consisting of gas, liquid and solid phases is treated as a mixture of fluids, which is the collection of the immiscible and incompressible fluids Ω_i, as shown in Figure 7.1. The governing equations for the multiphase field, which correspond to of the so-called one-fluid model, are the mass conservation equation in Eulerian description, incompressible condition and momentum equation in conservation form:

$$\int_{\Omega} \frac{\partial \rho}{\partial t}\, d\Omega + \oint_{\partial\Omega} \rho \boldsymbol{u} \cdot \boldsymbol{n}\, dl = 0 \tag{7.1}$$

$$\oint_{\partial\Omega} \rho \boldsymbol{u} \cdot \boldsymbol{n} \; dl = 0 \tag{7.2}$$

$$\int_{\Omega} \frac{\partial u_i}{\partial t} \; d\Omega + \oint_{\partial\Omega} u_i \boldsymbol{u} \cdot \boldsymbol{n} \; dl = \int_{\Omega} f_i \; d\Omega - \frac{1}{\rho} \oint_{\partial\Omega} p \cdot \boldsymbol{n} \; dl + \oint_{\partial\Omega} \frac{\mu}{\rho} \nabla u_i \cdot \boldsymbol{n} \; dl \tag{7.3}$$

with

$$\rho = \frac{\sum_k \Omega_k \rho_k}{\Omega} \tag{7.4}$$

$$u_i = \frac{\sum_k \Omega_k \rho_k u_{k,i}}{\Omega} \tag{7.5}$$

$$p = \frac{\sum_k \Omega_k p_k}{\Omega} \tag{7.6}$$

$$\mu = \frac{\sum_k \Omega_k \mu_k}{\Omega} \tag{7.7}$$

where t is time; ρ is the cell averaged fluid density; u_i is the velocity component with subscript $i = 1$, 2 and 3 in x, y and z directions, respectively; x, y and z are the orthogonal coordinates; $\boldsymbol{n}$ is the unit normal vector on the domain boundary $\partial\Omega$ towards the outside direction; f_i is the external force component due to acceleration; p and μ are the cell averaged fluid pressure and viscous coefficient, respectively; and Ω_k is the volume of the fluid-k.

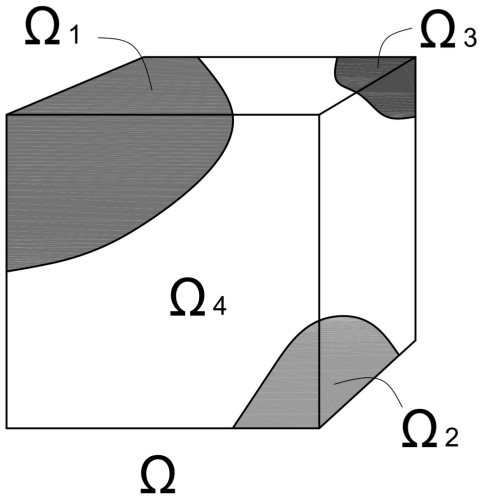

Figure 7.1: Multiphase field Ω including various phases Ω_i.

7.1.2 Sub-cell method

The physical values of the mixture of fluids need to be determined for each fluid cell. Since the fluid cell is based on the Eulerian grid which is fixed in the space. The volume-averaged physical value ψ in the cell C is estimated with the following equation:

$$\psi = (1 - f)\psi_g + (f - \sum_{O_k \epsilon C} \alpha_k)\psi_l + \sum_{O_k \epsilon C} \alpha_k \psi_{bk} \tag{7.8}$$

where ψ_g, ψ_l, and ψ_{bk} are physical values of gas, liquid phases and the object-k, O_k, respectively. The volume fraction of liquid and solid phases in a fluid-cell is given by f, while the fraction of the solid part is defined by α_k. The fraction α_k is approximated with a sub-cell method, as illustrated in Figure 7.2. When an element is included in the multiple fluid-cells, each fluid-cell is divided into multiple sub-cells and α_k is determined from the number of sub-cells included in the element.

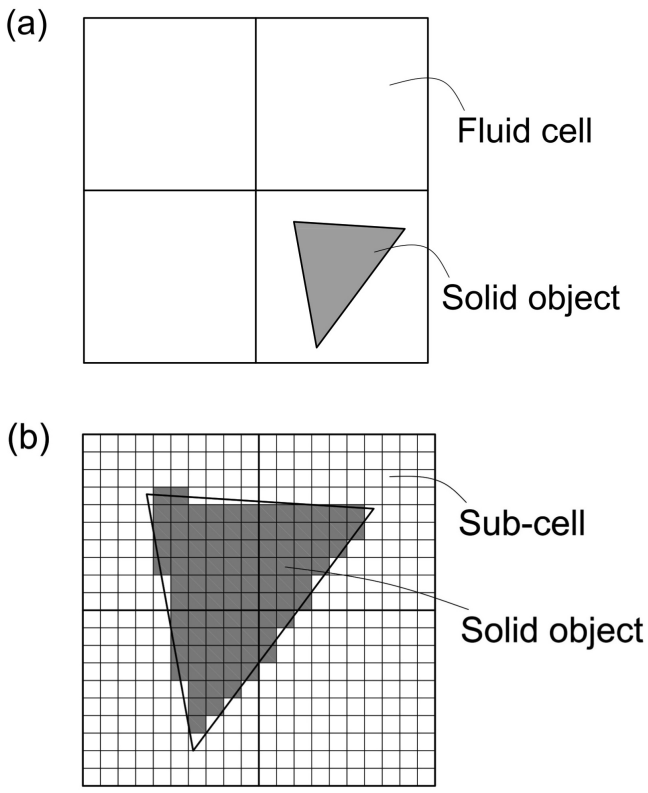

Figure 7.2: Subcell method; (a) In case of the solid object in a single fluid-cell and (b) In case of the solid object in multiple fluid-cells

7.1.3 Convection diffusion equation for transported concentration

The concentration of the transported concentration was obtained by solving the convection-diffusion equation:

$$\int_{\Omega} \frac{\partial c}{\partial t}\, d\Omega + \oint_{\partial\Omega} \boldsymbol{u}c \cdot \boldsymbol{n}\, dl = \oint_{\partial\Omega} \frac{\nu}{\sigma_c} \nabla c \cdot \boldsymbol{n}\, dl \tag{7.9}$$

where c is the transported concentration, and σ_c is Schmidt number for concentration diffusion, which represents the ratio of viscosity to fluid diffusivity.

7.1.4 Computational procedure

The basic equations are dicretized in a collocated grid system and solved with a finite volume method. The volume fraction of the solid object included in a fluid-cell is evaluated with the tetrahedron sub-cell method and the volume-averaged physical properties are evaluated using Eq.(7.8). Then, on the basis of the computational method for incompressible fluids, a tentative velocity components are calculated at the cell center points with the C-ISMAC method (21) while the convection terms are estimated with the fifth-order TVD scheme. The derived velocity components are spatially interpolated on the cell-boundaries and the pressure computations are performed with the C-HSMAC method in order to prevent pressure oscillation(76). The free-surface profiles are calculated from Eq.(7.1) with a non-diffusion filter. Concentrations can be estimated using the convection-diffusion equation, Eq.(7.9), using the computed velocity field. A simplified equation of state is used to compute the liquid density according to the concentration values, given in a simple linear equation:

$$\rho = \rho_o(1 - \beta c) \tag{7.10}$$

where ρ_o is the reference density which are usually taken as 0.998 g/cm^3 for fresh water; and β is the direct proportional coefficient of the concentration gradient between the maximum and minimum value.

The computational cells are decomposed into multiple sub-domains and their computations are simultaneously performed with distributed-memory system on the basis of a 3D domain decomposition method. This method is implemented by message-passing interface (MPI) which allows us to significantly reduce the elapsed time of computation.

7.2 Model Validation With Experimental Results

The present model has been tested to evaluate its applicability. Therefore, it was applied to density stratification problems and compared with experimental results. The simulation results for these test cases are described below.

7.2.1 Boussinesq lock-exchange experiment

This model was applied to the Boussinesq lock-exchange experimental results obtained by Kolar et al. (79). The density cell had internal dimensions of length (B) = 58.4 cm, height (H) = 29.5 cm, and width = 2.54 cm. The both mixing fluids were initially separated by the barrier which was 0.4 mm thick of stainless steel sheet. The both mixing fluids were fresh water and saline water with a salt concentration of 17.5 ppt. Water at room temperature was used, resulted in a heavy water density (ρ_1) of = 1.011 g/cm^3 and a light water density (ρ_2) of 0.998 g/cm^3, for a density ratio of 0.987, which was clearly in the Boussinesq realm.

Herein, we present high resolution outcomes for direct and quantitative comparison of experimental and numerical results throughout the domain, not just the wave front. Figure 7.3 compares the model results with the laboratory experiments and determines how well the model captured the evolution of a density field that is driven entirely by gravity currents. This figure clearly shows a good agreement between the calculated density propagation of the wave front compared with those which were experimentally measured. In addition, a coincidence between the front position for the estimated and the measured data was obtained as shown in Figure 7.5.

7.2.2 Non-Boussinesq lock-exchange experiment

Lowe et al. (80) have carried out a series of experiments on the lock exchange involving fluids with large density differences - the non-Boussinesq case. One of the experiments is selected in this study. The experiments were performed in a rectangular channel using two fluids of density ratio ($\gamma = 0.681$). The less dense fluid was freshwater (ρ_2 = 0.998 g/cm^3) and the denser fluid was either a solution of sodium chloride (NaCl) or sodium iodide (NaI) (ρ_1 = 1.466 g/cm^3). The channel length was B = 182 cm, width 23 cm wide and was filled to a depth of H = 20 cm. The flow was started by a vertically removing lock gate.

Figure 7.4 compares the model results with the laboratory experiments and determines how well the model captured the evolution of a density field that is driven entirely by gravity currents. This figure clearly shows an acceptable agreement between the calculated density propagation of the wave front compared with those which are experimentally measured but in a different time scale. In addition, the developed model successfully predicted the bore within the heavy front. The front velocity of the density current is almost the same for the light case as well as the heavy case as shown in Figure 7.6. Discrepancies may be observed because of the gate removal effect.

7.2.3 Nakaumi-Shinji coastal lakes system experiment

Nakaumi and Shinji are brackish coastal lakes connected by the Ohashi River. Laboratory experiments on the density stratification of Nakaumi-Shinji coastal lakes system were carried out by Kimura et al. (83). A simplified physical model of 1/25000 was used to study the behavior of saline water propagation to brackish lake through a river. Figure 7.7 shows a schematic sketch for the used physical model set-up. In this model, Lake 1 is representing the brackish Lake Shinji while Lake 2 is representing the saline water Lake Nakaumi. The two lakes are connected by Ohashi River which controls the salinity propagation between them. Case B was selected in this study where the water depth in Lake 1 was 6.0 cm and the river width was 4.0 cm. The experiment was conducted using the lock exchange technique. The both mixing fluids were fresh water and saline water with a salt concentration of 1%, 2% and 3%.

Figure 7.8 shows the used computational domain and the used tetrahedron solid block. At the solid object cells, the velocity is set to zero. Figure 7.9 presents a visualization plot for the density current propagation. Fresh water propagates into Lake 1 in the upper layers while the saline water encroach Lake 2 through the bottom layers. Figure 7.10 compares the model results with the laboratory results. This figure clearly shows a good agreement between the calculated density propagation front position and those that are experimentally measured. The present model is successfully able to predict density current due to density variations.

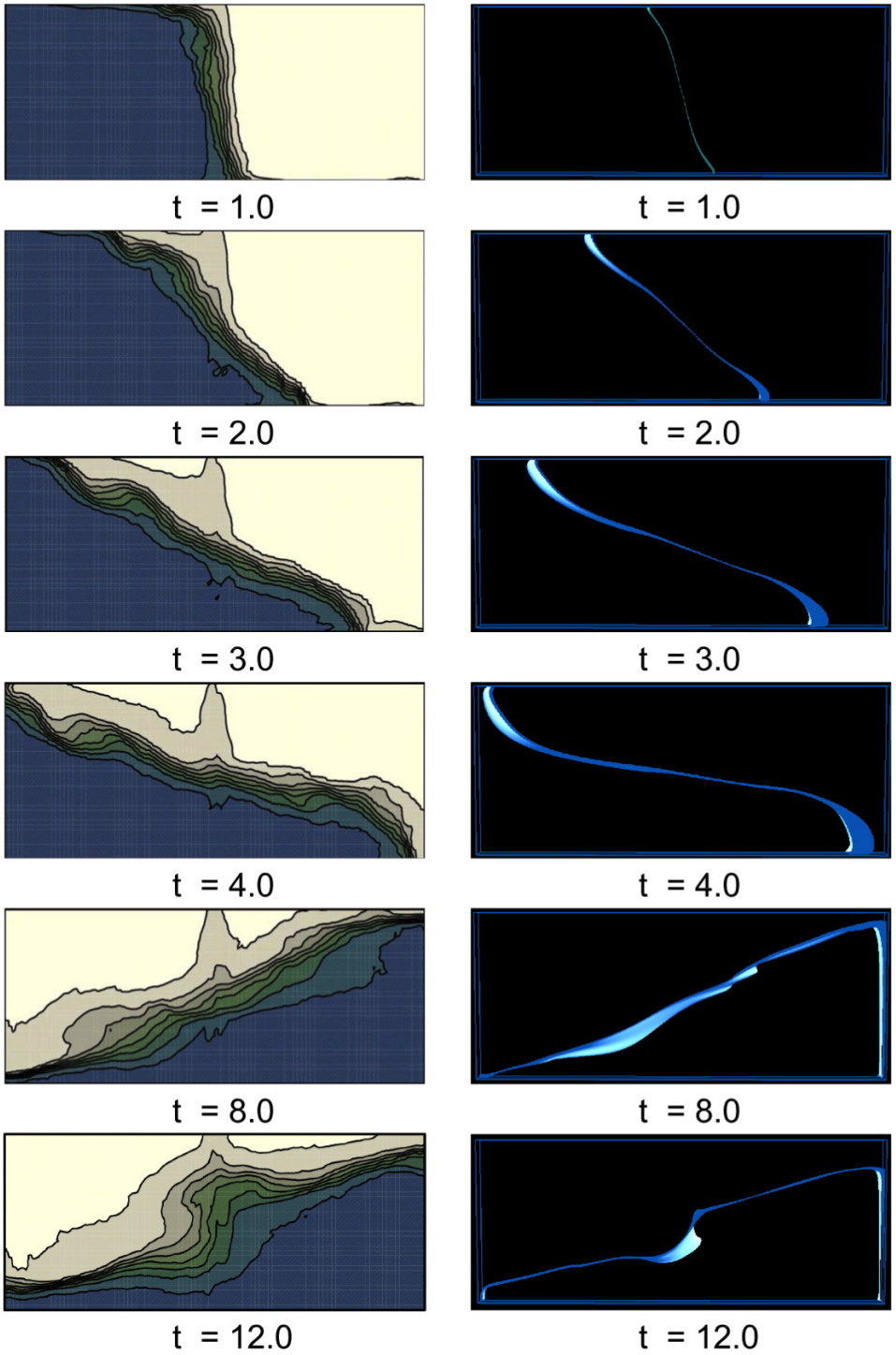

Figure 7.3: Comparison of experimental and predicted results for the density current propagation sequences for the Boussinesq lock-exchange case; (left) laboratory results and (right) model results.

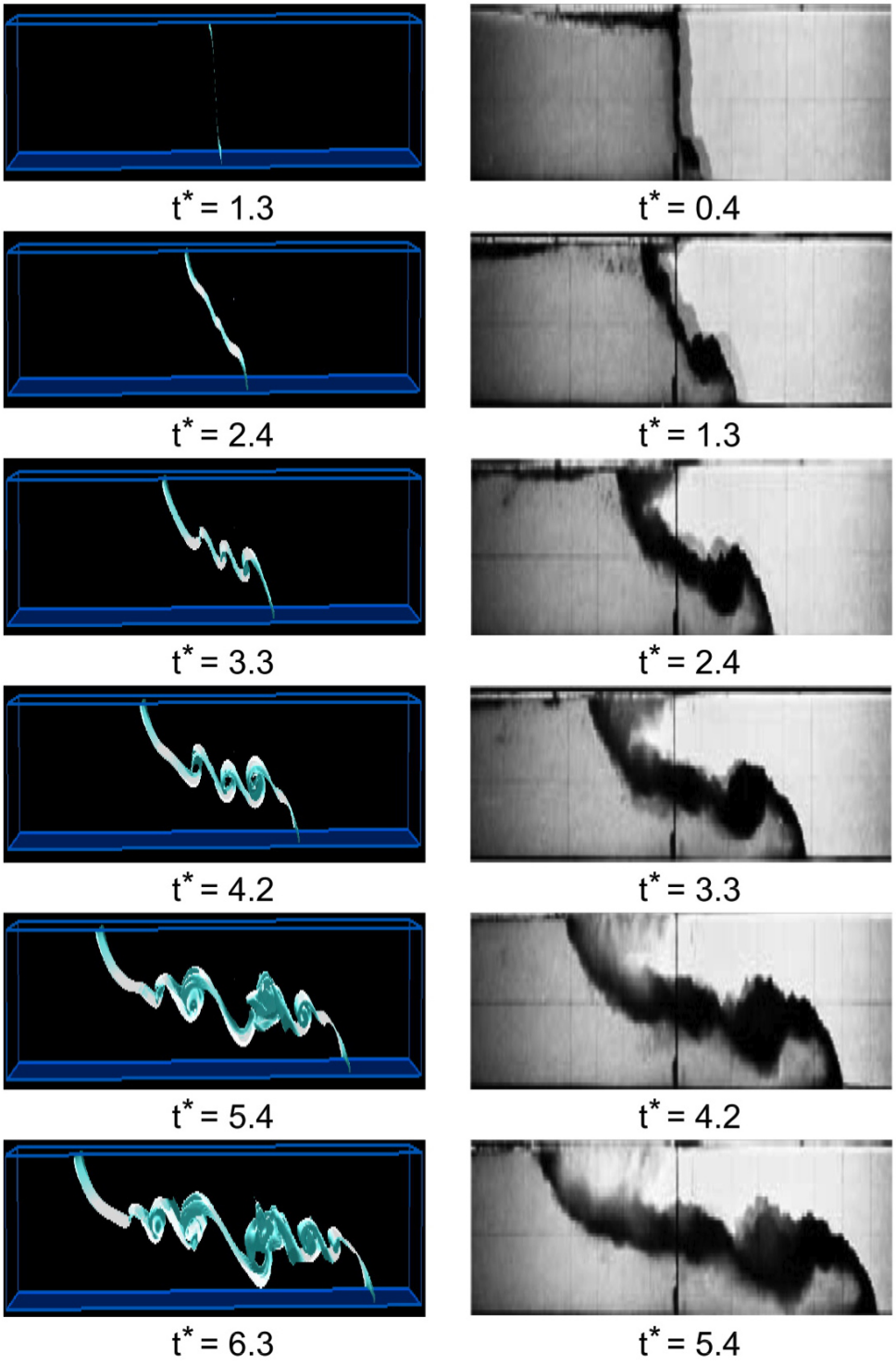

Figure 7.4: Comparison of experimental and predicted results for the density current propagation sequences for the non-Boussinesq lock-exchange case, (where $t^* = t\sqrt{(g(1-\gamma))/H}$); (left) model results and (right) laboratory results.

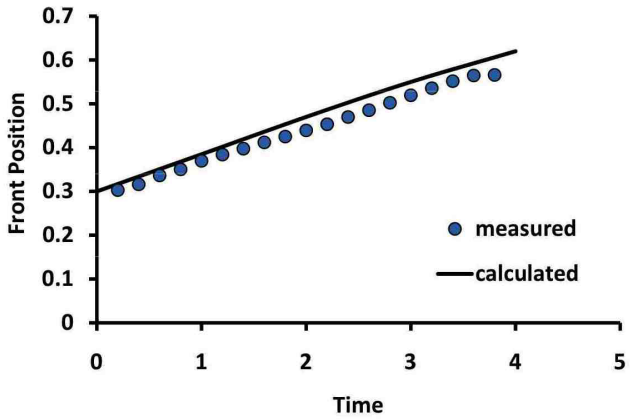

Figure 7.5: Comparison of the front position estimated from the laboratory experiments and the present model for the Boussinesq lock-exchange case.

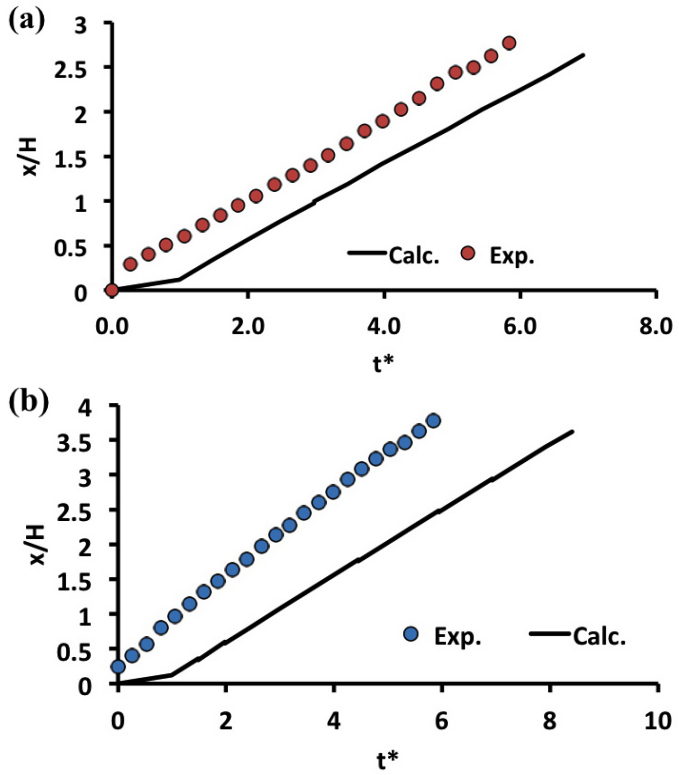

Figure 7.6: Comparison of the relative front position estimated from the laboratory experiments and the present model for the Boussinesq lock-exchange case; (a) light front and (b) heavy front

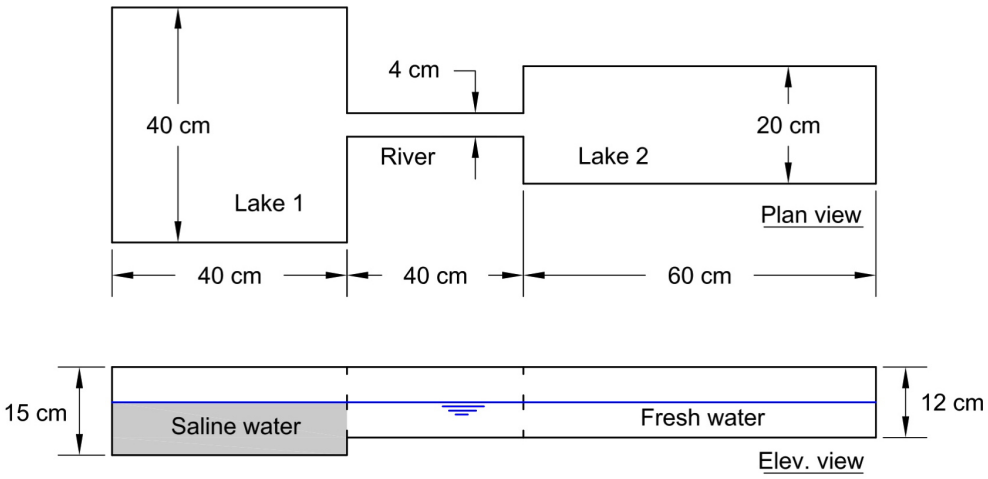

Figure 7.7: Schematic sketch for the physical model set-up.

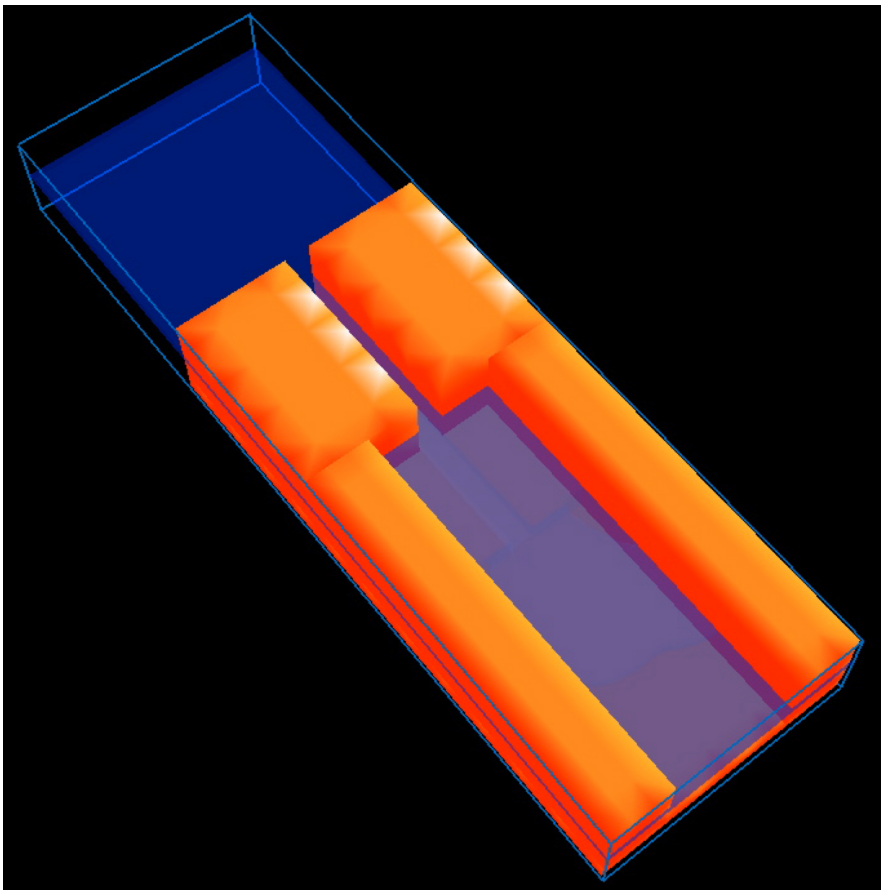

Figure 7.8: The computational domain representing the brackish lakes system.

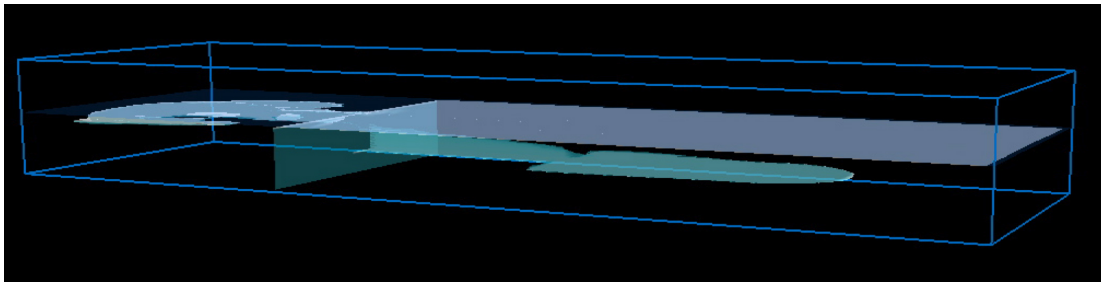

Figure 7.9: The density current propagation into lake 2.

7.3 The Model Application on El-Burullus Lake

The 3D multiphase model is applied on El-Burullus Lake to test the model ability to predict density stratification in large scale problems. Figure 7.11 and 7.12 show the layout of the El-Burullus Lake which is produced by the 3D multiphase model. The present model is a direct numerical simulation in which the Navier-Stokes equations are numerically solved without any turbulence model. Therefore, the computational cost is very high and the computational resources required exceed the capacity of the supercomputer. However, it is possible to perform numerical experiments for short-term periods allowing a better understanding of the brackish lakes physics. The lack of the short-term data for El-Burullus Lake built a barrier to compare the model results with field data. Given the potential of the 3D multiphase model it is likely that rapid growth of the future high-performance computer architectures is set to continue.

7.4 Summary

3D multiphase model based on MICS algorithm is used to detect the density current propagation. This method predicts the interaction between three-dimensional (3D) free surface flows and solid bodies. The free-surface flow including solid objects is modeled as a multiphase flow field. The governing equations for the multiphase field are solved on the basis of a finite volume method with collocated grid system. The model is successfully predicted the density current propagation in the lock-exchange problems for Boussinesq and non-Boussinesq experimental cases. Moreover, the model is applied to the experimental results of the Nakaumi-Shinji coastal lakes system. Good agreement between experimental results of the density current propagation front position and those

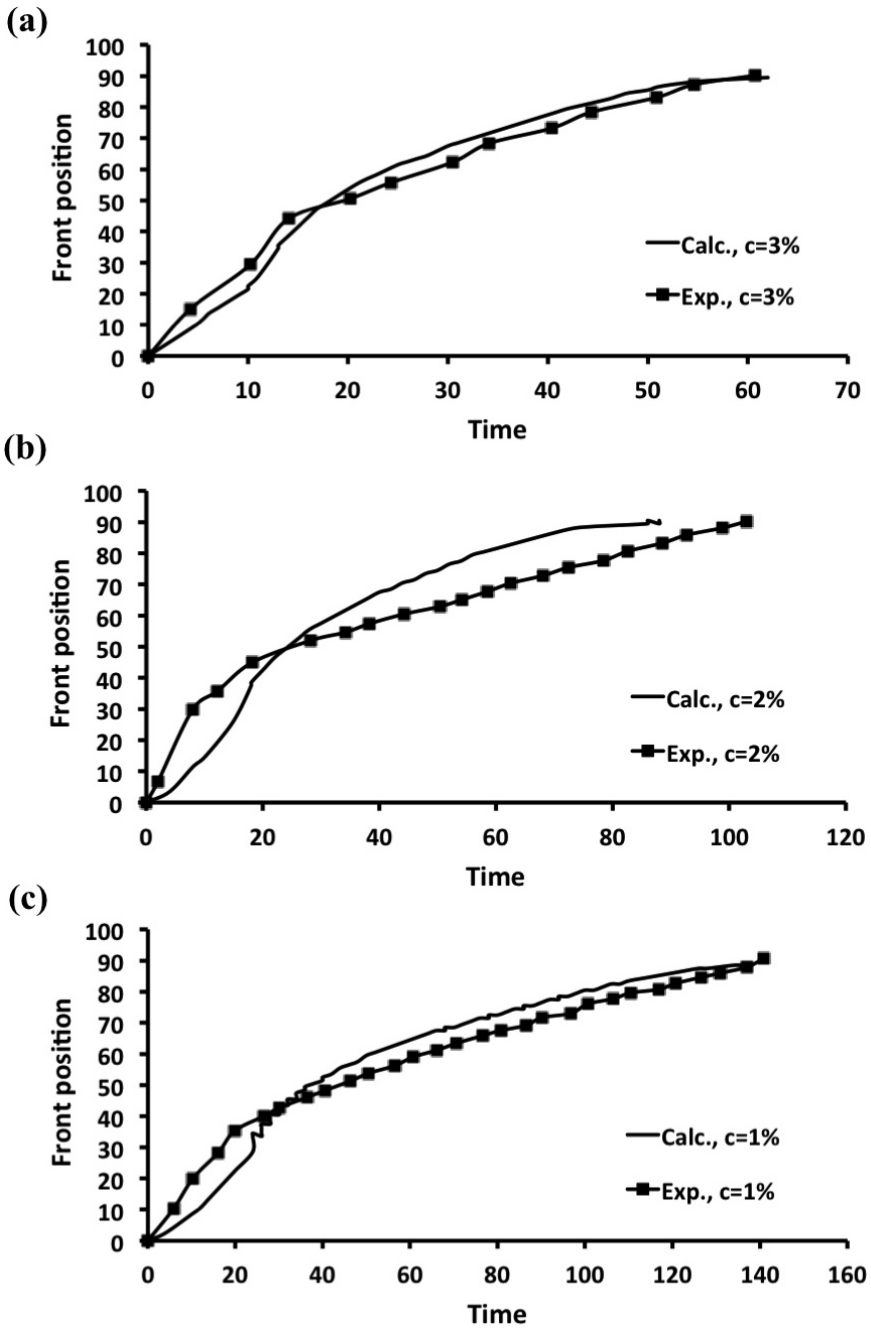

Figure 7.10: Comparison of experimental and predicted results for the saline water front position for different saline water concentrations; (a) 3% concentration, (b) 2% concentration, and (c) 1% concentration.

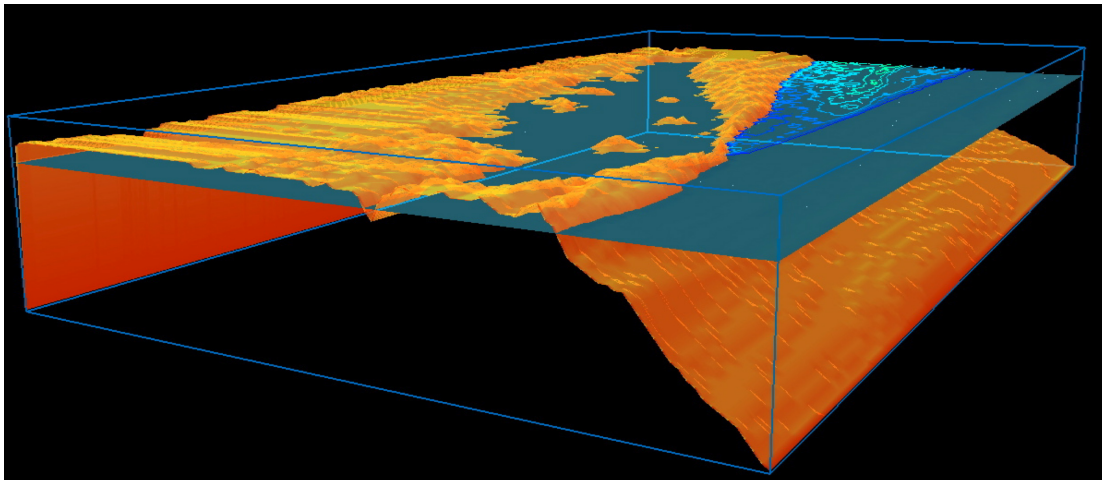

Figure 7.11: Layout of El-burullus simulated by the 3D multiphase model.

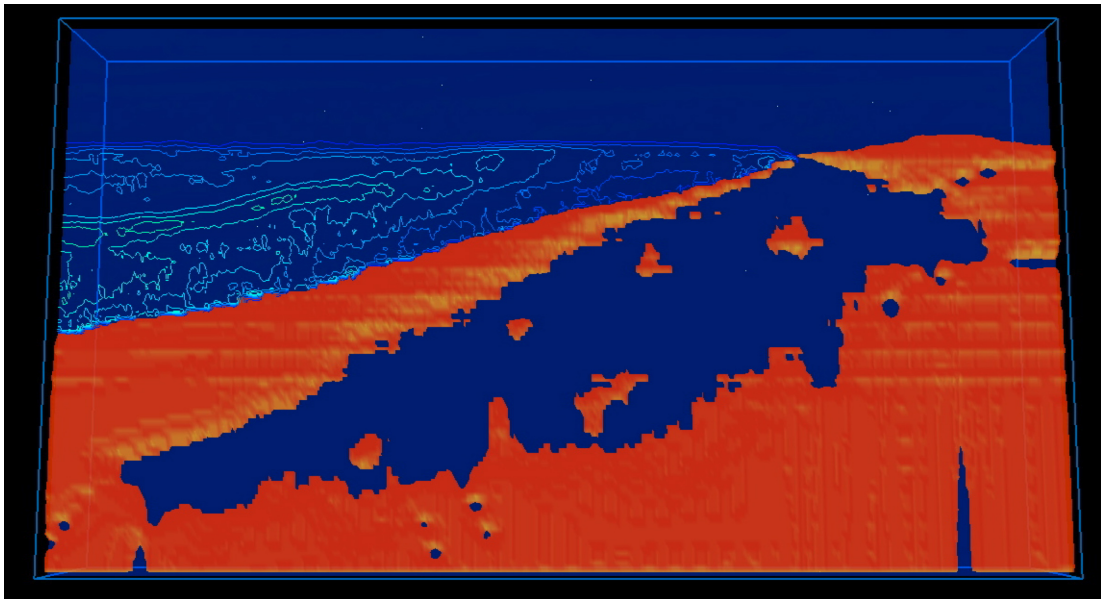

Figure 7.12: Aerial view for the lake produced by the present model.

that are numerically estimated. Short-term measurement data is needed to simulate large scale problems as El-Burullus Lake. Long-term simulations are beyond the current computational resources.

8

Conclusions

This study is representing a numerical study for El-Burullus lagoon brackish water as a model example for the other Egyptian coastal lakes on the Mediterranean Sea. This lake ecosystem has deteriorated since Aswan High Dam Construction, 1965. It is suffering from many problems, which might lead to environmental degradation and substantial changes in its ecosystem. Lake salinity has suffered from significant decrease due to excess unregulated drainage water effluent into the lake, which affected the lake flora and fauna. The purpose of the current study is to restore the salinity conditions of El-Burullus Lake to those before the construction of Aswan High Dam. For this purpose, three models are developed to simulate the lake hydrodynamics, circulation and salinization dynamics process as follows:

8.0.1 Depth-averaged mass transport model

This model is based on MACS algorithm with unstructured collocated grid system using the distributed memory system. The model numerical solutions is built on recent advances to couple numerical processes of hydrodynamic and mass transport equations using the FVM in discretization. Further, on the basis of a domain decomposition method, the unstructured cells are decomposed into multiple sub-domains and their computations are simultaneously performed with distributed-memory system. This method is implemented by MPI which significantly reduce the elapsed time of computation. It was demonstrated that the parallel efficiencies are attained by parallel computations. This model is able to predict the mass transported concentrations in shallow waters. The model has been successfully verified against analytical solution to

the advection diffusion equation and experimental measurements to transported concentration cloud in a meandering channel.

Furthermore, a numerical prediction method for equilibrium and non-equilibrium sediment transport under current and wave actions has been included in the present model. The partial differential equations for 2D shallow water flow, suspended-load, bed-load sediment and bed evolution were successfully incorporated to predict the bed morphological changes. The developed model has been tested in different laboratory cases: scour downstream solid apron, shallow basin erosion due to clear water, sedimentation in a channel perpendicular to unidirectional flow of current and waves and local scouring around bridge pier abutment. Generally, good agreement was obtained between numerical simulation results and experimental data. This fact shows that the present numerical method is able to predict the sand bed profiles reasonably. After model verification, the developed model is applied to El-Burullus shallow coastal lake in Egypt. Salinity distribution inside the lake is reasonably simulated considering the effect of bathymetry, tidal current, wind, precipitation, evaporation and drainage discharges. It is verified that the model has the potential for simulating long-term coastal processes using parallel computation.

8.0.2 Two-phase flow mass transport model

A two-dimensional multiphase numerical model for incompressible, immiscible and variable density fluids has been developed to study stratification process of brackish coastal lakes due to density variation. The governing equations are discretized in a collocated grid system and solved with a finite volume method. A parallel computation technique in shared memory system is implemented in the present model by Open Multiprocessing (OpenMP). The developed model successfully predicted the density current propagation in the lock-exchange problems for Boussinesq and non-Boussinesq experimental cases. In addition, the model is applied to simulate salinity intrusion into Ohashi River that connects Nakaumi and Shinji brackish coastal lakes. The developed model successfully predicted the density current propagation in the River. However, this model still needs refinement to avoid concentration oscillations.

8.0.3 Three-dimensional multiphase model

This model is based on MICS algorithm which predicts the interaction between three-dimensional (3D) free surface flows and solid bodies. The free-surface flow including solid objects is modeled as a multiphase flow field. The governing equations for the field are solved on the basis of a finite volume method with collocated grid system. The model successfully predicted the density current propagation in the lock-exchange problems for Boussinesq and non-Boussinesq experimental cases. Moreover, the model is applied to the experimental results of the Nakaumi-Shinji coastal lakes system. Good agreement between experimental results of the density current propagation front position and those that are numerically estimated.

8.0.4 El-Burullus shallow coastal lagoon

The validated depth-averaged mass transport model is applied to Burullus shallow coastal lake, Egypt. Salinity distribution inside the lake has been reasonably simulated considering the effect of bathymetry, tidal, wind, precipitation, evaporation and drainage discharges. Five scenarios were studied for further understanding of the lake circulation and salinity dynamics and to investigate possible means of restoring them to the desired state as before Aswan High Dam Construction. Salinity dynamics have been simulated for various possible scenarios: before constructing Aswan High Dam, current status, drainage discharge elimination, case of adding new breach-way, and changing drainage water routing, in order to adequately manage temporal salinity in Burullus lagoon. These scenarios revealed the importance of fresh drainage water discharges into the lake and the possibility to eliminate the effluent discharge during January to March which allow sea water to invade the lake and permit salinity exchange. The stored water can be used as an artificial flood similar to pre-Aswan High Dam construction flood, which unexpectedly increases the lake water level to become brackish water again.

In addition, the present model is used to investigate the impact of climate change on salinization process in El-Burullus Lake. The model is used to predict the salinization and circulation processes occurring under the effect of two global emission scenarios (SRES A2 and SRES B1) archived from the 2007 IPCC Fourth Assessment Report (AR4) which are abstracted from four different atmosphere-ocean coupled general circulation models (AOGCMs). Climate change will lead to double the salinity values

inside El-Burullus Lake under the current conditions of drainage flux. Though results show that salinity values will increase to double the current values, they are still much lower than those before constructing Aswan High Dam. A dynamic discharge system is proposed to re-originate lakes salinity under climate change conditions where it is recommended to reduce winter season drainage flux by 75% and release it again uniformly during summer and autumn seasons. This may improve salinity values and circulation in the lake, which may re-originate the lake's aquatic flora and fauna, and enhance its ecosystem.

The multiphase models are applied on El-Burullus Lake for further understanding of the lake hydrodynamic behavior and the effect of changing the fresh water routing on the lake stratification. Using the Two-phase model, the lake is studied under actions of the total flux of fresh water and sea water level boundary conditions. The numerical simulation results revealed the necessity of the three dimensional study. The 3D multiphase model is then applied to El-Burullus Lake to test the model ability to predict density variations in large scale problems. The 3D multiphase model is a direct numerical simulation in which the Navier-Stokes equations are numerically solved without any turbulence model. Therefore, the computational cost is very high and the computational resources required exceed the capacity of the supercomputer. However, it is possible to perform numerical experiments for short-term periods allowing a better understanding of the brackish lakes physics. The lack of the short-term data for El-Burullus Lake built a barrier to compare the model results with field data. Given the potential of the 3D multiphase model it is likely that rapid growth of the future high-performance computer architectures is set to continue.

References

[1] F. Murphy, H. Secor, The distribution of juvenile fishes in maryland coastal bays in relation to environmental factors: A multivariate analysis, Technical Report of the University of MD Center for Environmental Science Series No.TS-494-05-CB. 1

[2] R. Barnes, Coastal lagoons, Cambridge University Press, Cambridge. 1

[3] N. P. Smith, Seasonal-scale transport patterns in a multi-inlet coastal lagoon, Estuarine, Coastal and Shelf Science 52 (2001) 15–28. 1

[4] M. M. Nichols, J. D. Boon, Coastal lagoon processes, Elsevier, Amsterdam, The Netherlands, 1994. 1

[5] S. H. A. Rahman, Egypt country report, Meeting on Mediterranean coastal lagoons management: interaction between aquaculture and capture fisheries, Cagliari. 2

[6] J. Oczkowski, N. Nixon, Lagoons of the Nile Delta, In Coastal Lagoons: Critical Habitats of Environmental Change, CRC Press, 2010. 2

[7] A. El-Sabrouti, Mineralogy and sources of bottom sediments of lake burullus, egypt, J. Afr. Earth science 2 (1984) 151–153. 7, 28

[8] M. Shakweer, H. El Ebiary, A. Zaki, Comparative study on the major biochemical constitutents in the muscles of mugil cephalus inhabiting the mediterranean water, the northern delta lakes and fish farms of egypt, Bull. National Inst. of Oceanography and Fish 24 (1998) 79–101. 7, 28

[9] A. Al-Says, A. Radwan, r. L. Shakwee, Impact of drainage water inflow on the environmental conditions and fishery resources of lake borollus, Egyptian journal of aquatic research 33 (1) (2007) 312–351. 7, 31, 35

[10] A. Alsays, Studies on experimental fishing twines and nets and their efficiency and selectivity in fishing operations in lake borollus, ph.D thesis, Fac. Sci. Alexandria Univ. 11 (1967) 292. 7, 31

[11] M. e. a. Kassas, Management plan for burullus protected area, Med wet coast, global environment facility and Egyptian Environmental Affairs Agency, Cairo, Egypt. 7

[12] A. Younes, E. Nafea, Impact of environmental conditions on the biodiversity of mediterranean sea lagoon, burullus protected area, egypt, World Applied Sciences Journal 19 (2012) 1423–1430. 8

[13] N. Peja, A. Vaso, A. Miho, N. Rakaj, A. Crivelli, Characteristics of albanian lagoons and their fisheries, Fish. Res. 27 (1996) 215–225. 8

[14] N. Quinn, C. Breen, A. Whitfield, J. Hearne, An index for the management of south african estuaries for juvenile fish recruitment from marine environment, Fish. Manag. Ecol. 6 (1996) 421–436. 8

[15] A. Padmavathy, M. Anbarashan, Biodiversity of coastal lagoon in nallavadu village, puducherry, india, Int. J. Biodivers. Conserv. 5(1) (2013) 33–38. 8

[16] S. Ushijima, H. Yamashita, S. Fujioka, I. Nezu, Prediction method for shallow water equations based on the method for incompressible fluids with collocated grid, Annual Journal of Hydraulic Engineering 50 (775-780). 13, 17

[17] S. Ushijima, A. Fukutani, H. Yamashita, I. Nezu, Numerical prediction of sub- and super-critical flows by shallow water equations with macs, Annual Journal of Hydraulic Engineering 51 (811-816). 13, 17

[18] H. Yamashita, S. Ushijima, Parallel smac algorithms to solve shallow water equation with unstructured collocated grid system, Annual Journal of Hydraulic Engineering 55 (S-1213). 13

[19] G. Jayaraman, A. D. Rao, e. A. Dub, P. K. Mohanty, Numerical simulation of circulation and salinity structure in chilika lagoon, J. Coastal Engrg. 22 (2005) 195–211. 14

[20] M. Longuet-Higgins, R. Stewart, Radiation stress in water waves, a physical discussion with application, Deep-Sea Res 11 (1964) 529–563. 15

[21] S. Ushijima, I. Nezu, High-order implicit method (c-ismac method)for incompressible flows with collocated grid system, Doboku Gakkai Ronbunsyuu 719 (2002) 21–30. 15, 19, 104

[22] G. Karypis, V. Kumar, Multilevel k-way partitioning scheme for irregular graphs, Journal of Parallel and Distributed Computing 48 (1) (1998) 96–129. 21

[23] P. Pacheco, Parallel programming with MPI, Morgan Kaufmann Publisher, Inc., 1997. 21

REFERENCES

[24] L. Runkel, Solution of the advection-dispersion equation: continuous load of finite duration, J. Environmental Engrg., ASCE 122 (9) (1996) 830–832. 22

[25] K. Beak, W. Seo, S. Seong, Evaluation of dispersion coefficients in meandering channels from transient tracer tests, J. Hydraulic Engrg., ASCE 132 (10) (2006) 1021–1032. 23

[26] I. Beltagy, Sequences and consequences of pollution in northern egyptian lakes, lake burullus, Bull. National Inst. of Oceanography and Fish 11 (1985) 73–97. 28

[27] H. Dumont, G. El-Shabrawy, Lake borullus of the nile delta: a short history and an uncertain future, Ambio, J. Hum. Environ. 36 (8) (2007) 677–682. 28, 31

[28] K. Shaltout, Y. Al Sodany, Vegetation analysis of burullus wetland: a ramsar site in egypt, Wetlands Ecol Manage 16 (2008) 421–439. 31

[29] L. Meyer, J. Johnson, J. Gill, Comparison of nekton use of phragmities australis and spartina alterniflora marshes in the chesapeake bay, usa, Marine Ecology-Progress Series 209 (2001) 71–84. 31

[30] M. Chambers, L. Mayerson, K. Saltonstall, Extension of phragmities australis into tidal wetlands of north america, Aquatic Botany 64 (1999) 261–273. 31

[31] C. Hudon, P. Gagnon, M. Jean, Hydrological factors controlling the spread of common reed (phragmities australis) in the st. lawrence river (quebec, canada), Ecoscience 12 (3) (2005) 347–357. 31

[32] S. Hellings, J. Gallagher, The effects of salinity and flooding on phragmities australis, Journal of Applied Ecology 29 (1992) 41–49. 33

[33] M. Okbah, N. Hussein, Impact of environmental conditions on the phytoplankton structure in mediterranean sea lagoon, lake burullus, egypt, Water, Air, and Soil Pollution 172 (2006) 129–150. 34

[34] A. El-Shinnawy, Impact of the agricultural drainage on hydrological environment of al-burullus lake., First African Regional Conference on Drainage (ARCOD), Cairo. 34

[35] E. Ali, Impact of drain water on water quality and eutrophication status of lake burullus, egypt, a southern mediterranean lagoon, African Journal of Aquatic Science 36 (3) (2011) 267–277. 34

[36] H. Farag, E.-G. A., Assessment of the eutrophic status of lake burullus (egypt) using remote sensing, International journal of environmental science and engineering 2 (2012) 61–74. 34

[37] A. ElSayed, Eutrophication assessment of lake burullus, egypt, First international conference on coastal zone management of river deltas and low land coastlines (2010) 473–483. 34

[38] I. Abdel Rahman, A. Sadek, The application of multispectral remote sensing to the assessment of north nile delta, egypt, Academy of scientific Research and Technology. 35

[39] G. El-Bayomi, Lake burullus : a geomorphological study, ph.D thesis, Fac. Arts, Helwan Univ. (1999). 35

[40] A. M. Fanos, Longshore current analysis and littoral drift near burullus outlet, Coastal Research Institute. 39

[41] I. El-Shinnawy, Water budget estimate for environmental management at al-burullus lake, egypt, Egyptian Environmental Affairs Agency (EEAA). 39

[42] M. Parry, O. Canziani, J. Palutikof, P. van der Linden, C. Hanson, Ipcc (2007) climate change 2007:impacts, adaptation and vulnerability. contribution of working group ii to the third assessment report of the intergovernmental panel on climate change., Cambridge University Press, Cambridge, UK (2007). 51, 52

[43] J. Milliman, J. Broadus, F. Gable, Environmental and economic implications of rising sea level and subsiding deltas: the nile and bengal examples, Ambio 18 (1989) 340–345. 52

[44] D. Stanley, G. Warne, Sea level and initiation of predynastic culture in the nile delta, Nature 363 (1993) 435–438. 52

[45] M. El-Raey, S. Nasr, O. Frihy, E.-D. S., K. Dewidar, Adaptation to the impacts of sea level rise in egypt, Climate Research 12 (1999) 117–128. 52

[46] O. Frihy, E. Deabes, S. Shereet, F. Abdalla, Alexandria-nile delta coast, egypt: update and future projection of relative sea-level rise, Environ Earth Sci 61 (2010) 253–273. 52

[47] F. O., K. El-Sayed, Vulnerability risk assessment and adaptation to climate change induced sea level rise along the mediterranean coast of egypt, Mitigation and adaptation strategies for global change (2012) s11027. 52

[48] M. El-Raey, S. Nasr, O. Frihy, E.-D. S., K. Dewidar, Potential impacts of accelerated sea level rise on alexandria governorate, egypt, J. Coast. Res 14 (1995) 190–204. 52

[49] A. H. El-Nahry, R. Doluschitz, Climate change and its impacts on the coastal zone of the nile delta, Environ Earth Sci 59 (2010) 1497–1506. 52

[50] C. W. Thornthwaite, An approach toward a rational classification of climate, Geographic Review 38 (2010) 55–94. 53

[51] Y. Shimizu, H. Yamaguchi, T. Itakura, Three-dimensional computation of flow and bed deformation., Journal of Hydraul. Eng. 116(9) (1990) 1090–1108. 64

[52] N. Olsen, M. Melaaen, Three-dimensional calculation of scour around cylinders., Journal of Hydraul. Eng. 119(9) (1993) 1048–1053. 64

[53] S. Ushijima, Arbitrary lagrangian-eulerian numerical prediction for local scour caused by turbulent flows., journal of Computational physics 125 (1996) 71–82. 64, 73

[54] B. Duc, T. Wenka, W. Rodi, Numerical modeling of bed deformation in laboratory channel., Journal of Hydraulic Engineering. 30(9) (2004) 894–904. 64

[55] N. Nagata, T. Hosoda, T. Nakato, Y. Muramoto, Three-dimensional numerical model for flow and bed deformation around river hydraulic structures., Journal of Hydraulic Engineering 131 (2005) 1074–1087. 64

[56] X. Liu, B. J. Landry, M. H. Garcia, Two-dimensional scour simulations based on coupled model of shallow water equations and sediment transport on unstructured meshes., Coastal Engineering 55 (2008) 800– 810. 64

[57] S. Li, J. Diffy, Fully coupled approach to modeling shallow water flow, sediment transport, and bed evolution in rivers., Water Resources Research 47 (2011) 3508– 3528. 64

[58] A. Sanchez, W. Wu, A non-equilibrium sediment transport model for coastal inlets and navigation channels, Journal of Coastal Research 59 (2011) 39–48. 64

[59] B. C. Phillips, A. J. Sutherland, Spatial lag effects in bed load sediment transport, Journal of Hydraulic Research 27(1) (1989) 115–133. 64

[60] W. Wu, Depth-averaged two-dimensional numerical modeling of unsteady flow and nonuniform sediment transport in open channel, J. Hydraulic Engrg., ASCE 130 (2004) 1013–1024. 64, 69

[61] E. Meyer-Peter, R. Muller, Formulas for bedload transport, Proceedings of the Second Meeting, IAHR. 2 (1948) 39–64. 66

[62] L. C. Van Rijn, Sediment transport, part i: bed load transport., J. Hydraul. Eng. 110 (1984) 14311456. 66, 70

[63] K. Ashida, M. Michiue, Studies on bed load transportation for non-uniform sediment and river bed variation, Disaster Prevention Research Institute Annuals, Kyoto Univ. (1971) 14,B. 66

[64] Y. Iwagaki, Y. Tsuchiya, Fundamental study on critical tractive force, Trans. Japan Soc. Civ. Engrg. 41 (1956) 1–21. 67

[65] M. Michiue, K. Suzuki, k. Kawatsu, Modeling of local scour processes downstream of a consolidation work across a river channel, Disaster Prevention Research Institute Annuals, Kyoto Univ. (1982) 25,B2. 67

[66] Q. W. Han, A study on the non-equilibrium transportation of suspended load, Proc., 1st Int. Symp. on river sedimentation, Beijing (1980). 69

[67] L. C. Van Rijn, Sediment transport, part ii: Suspended load transport., J. Hydraul. Eng. 110 (1984) 14311456. 70

[68] L. C. Van Rijn, Sediment transport, part iii: Bed forms and alluvial roughness., J. Hydraul. Eng. 110 (1984) 14311456. 70

[69] L. C. Van Rijn, Unified view of sediment transport by currents and waves. i: Initiation of bed motion, bed roughness, and bed-load transport., J. Hydraul. Eng. 133 (2007) 649–667. 71

[70] L. C. Van Rijn, Unified view of sediment transport by currents and waves. ii: Suspended transport., J. Hydraul. Eng. 133 (2007) 668–689. 71

[71] T. Thuc, Two dimensional morphological computations near hydraulic structures., Ph.D. thesis, Asian Institute of Technology (1991). 74

[72] L. C. Van Rijn, Sedimentation of dredged channels by currents and waves., Journal of waterway, port, coastal and ocean Engineering 112(5) (1986) 541–559. 77

[73] D. Husain, A. Quraishi, A. Ibrahim, Local scour at bridge abutments., Journal KAU Engineering science 10(1) (1998) 141–153. 77

[74] S. Onda, T. Hosoda, I. Kimura, Refinement of a depth averaged model in curved channel in generalized curvilinear system and its verification., Annual Journal of Hydraulic Engineering 50 (2006) 769–774. 80

[75] K. Hagaiwara, I. Kimura, Y. Shimizu, M. Seiji, Computation of suspended sediment transport in meandering channels using depth-averaged models with the effect of secondary currents., Annual Journal of Hydraulic Engineering 54 (2010) 697–702. 80

[76] S. Ushijima, Y. Okuyama, M. Takemura, I. Nezu, Parallel computational method for pressure field in incompressible flows on 3d curvilinear coordinates, Annual Journal of Hydraulic Engineering, JSCE 47 (2003) 385–390. 87, 104

[77] S. Ushijima, O. Makino, I. Nezu, Three dimensional computational method for wave flows running up in a river and their flooded flows, Journal of Hydroscience and Hydraulic Engineering 25 (2007) 31–39. 88

[78] OpenMP, Openmp applicaton program interface (2011).
URL http://www.openmp.org 89

[79] R. Kolar, T. Kibbey, C. Szpilka, K. Dresback, E. Tromble, I. Toohey, J. Hoggan, J. Atkinson, Process-oriented tests for validation of baroclinic shallow water models: The lock-exchange problem, Journal of Ocean Modelling 28 (2009) 137–152. 90, 105

[80] J. Lowe, W. James, P. Linden, The non-boussinesq lock-exchange problem: Part 1. theory and experiments, Journal of Fluid Mech. 537 (2005) 101124. 92, 105

[81] S. Moriwaki, T. Fujii, K. Fukui, Intrusion of high salinity water mass into ohashi river, sanin district of japan, Journal of Laguna. 10 (2003) 3545. 95

[82] S. Ushijima, Yamada, S. S. Fujioka, I. Nezu, Prediction method (3d mics) for transportation of solid bodies in 3d free-surface flows, JSCE Journal 810/II (74) (2006) 79–89. 101

[83] I. Kimura, A. Teramoto, M. Obata, T. Hosoda, Fundamental investigations on saline water current advansing into a brackish lake by laboratory tests and 3d computations, Annual Journal of Hydraulic Engineering 50 (2006) 1291–1296. 106